REPORT DOCUMENTATION PAGE

Form Approved OMB No. 0704-0188

Public reporting burden for this collection of information is estimated to average 1 hour per response, including the time for reviewing instructions, searching existing data sources, gathering and maintaining the data needed, and completing and reviewing the collection of information. Send comments regarding this burden estimate or any other aspect of this collection of information, including suggestions for reducing this burden to Washington Headquarters Services, Directorate for Information Operations and Reports, 1215 Jefferson Davis Highway, Suite 1204, Arlington, VA 22202-4302, and to the Office of Management and Budget, Paperwork Reduction Project (0704-0188), Washington, DC 20503.

1. AGENCY USE ONLY (Leave blank)	2. REPORT DATE 2000	3. REPORT TYPE AND DATES COVERED Final Report

4. TITLE AND SUBTITLE Characterization of Aircraft-Induced Atmospheric Aberrations	5. FUNDING NUMBERS F61775-99-WE

6. AUTHOR(S)

Prof Vladimir P. Lukin

7. PERFORMING ORGANIZATION NAME(S) AND ADDRESS(ES) Institute of Atmospheric Optics RAS 1 Akademicheskii Ave Tomsk 634055 Russia	8. PERFORMING ORGANIZATION REPORT NUMBER N/A

9. SPONSORING/MONITORING AGENCY NAME(S) AND ADDRESS(ES) EOARD PSC 802 BOX 14 FPO 09499-0200	10. SPONSORING/MONITORING AGENCY REPORT NUMBER SPC 99-4035

11. SUPPLEMENTARY NOTES

12a. DISTRIBUTION/AVAILABILITY STATEMENT Approved for public release; distribution is unlimited.	12b. DISTRIBUTION CODE A

13. ABSTRACT (Maximum 200 words)

This report results from a contract tasking Institute of Atmospheric Optics RAS as follows: The contractor will investigate the nature of aircraft-induced atmospheric refractive index distortions on laser beams, and attempt to develop models of these new types of distortions that are consistent with typical laser beam propagation codes.

14. SUBJECT TERMS EOARD, Aircraft-induced optical distortions, laser atmospheric propagation	15. NUMBER OF PAGES 57
	16. PRICE CODE N/A

17. SECURITY CLASSIFICATION OF REPORT UNCLASSIFIED	18. SECURITY CLASSIFICATION OF THIS PAGE UNCLASSIFIED	19, SECURITY CLASSIFICATION OF ABSTRACT UNCLASSIFIED	20. LIMITATION OF ABSTRACT UL

NSN 7540-01-280-5500

Standard Form 298 (Rev. 2-89)
Prescribed by ANSI Std. 239-18
298-102

Institute of Atmospheric Optics SB RAS
WAVE PROPAGATION DIVISION
Laboratory of Coherent and Adaptive Optics
Laboratory of Nonlinear Interaction

The final report for contract SPC99-4035

"Characterization of Aircraft-Induced Atmospheric Aberrations"

Under contract with European Office of Aerospace Research and Development, Air Force Office of Scientific Research, Air Force Research Laboratory

Principal Investigators

Prof. Alexander Zemlyanov
Prof. Vladimir Lukin

Tomsk -2000

20000628 114

AQF 00-09-2893

CONTENTS

INTRODUCTION

The first year stage of program of the investigations includes the work with references, development of experimental set up, creation of necessary devices, and experiments at Tomsk airport.

It is well known that data obtained from measurements of turbulence intensity, wind velocity profiles, and temperature at the altitudes of 10-15 km signify the zones of sharp changes near the tropopause. In this context it is essential to distinguish the foot print of the aircraft from characteristic of nondisturbed turbulence. So the work with references are still continue in the following directions:

atmospheric characteristic at altitudes of 10 - 15 km;

turbulence characteristic at altitudes of 10 - 15 km;

characteristic of aircraft engines, especially for B-747 and IL-86 planes, at altitudes of 10- 15 km;

characteristic of aircraft foot prints under conditions of real flight.

And direct measurements of turbulence and refraction are performing in a plane foot print at the ground level.

We are assuming to construct the model of atmospheric turbulence on the high elevated paths along the long distance propagation.

KEY WORDS: turbulence, wake vortex, aircraft, condensation trail, jet, vortex, dispersion and diffusion regimes, model.

Part I. CONDENSATION TRAILS

A brief review of the papers referring to gasdynamic, physical-chemical and optical properties of condensation trails behind high-altitude aircraft is done.

1.1. Introduction

In Europe, the USA and the world over (in Japan for example) the study of aviation emissions and its impact on the Atmosphere is of great interest during the last years [1.1-1.9]. The problem of contrail (condensation trail behind aircraft) formation and evolution is concerned with studying of atmosphere pollution, in particular with the problem of impact of aviation emission on the ozone layer [1.10].

ICAO (International Civil Aviation Organization) reports (1997) that in 1996 world-wide aviation transported 1.38×10^9 passengers using 12980 commercial jet aircraft and 3180 turboprop aircraft [1.4]. World-wide air traffic increased by 5 to 6 % annually on overage from 1970 to 1993, and by 7 to 8 % in the years 1994 to 1996. Global air traffic consumed aviation fuel at a rate of 130×10^{12} - 180×10^{12} g/year 1992 to 1995. It is about 5 to 6% of all petrol products. About 65% of the fuel is consumed at cruise at altitudes between 10 and 13 km. The largest fraction is consumed by wide-body aircraft such as the B-747 on long distance flights. Most of the emissions occur between $30°$ and $55°$N over USA, Europe and the North Atlantic. Globally the fraction of fuel burnt above the tropopause has been estimated to be about 34%. Over the North Atlantic the stratospheric fraction of fuel consumption is about 50% in the annual mean. Aviation fuel consumption grew by about 3% annually over the last 2 decades.

The cruise altitude of Super Sonic Transport (SST) of second generation would be 15 -18 km for Mach number 2 aircraft (such as Concorde) or 18-20 km for Mach 2,4 aircraft [1.2]. This range of altitudes is not far from: the peak of the ozone concentration (about 24 km); the altitudes of the Polar Stratospheric Clouds (PSC) with extend over the poles (about 20 km).

Spectral multidomain
direct numerical simulations
for the recovery of laminar two-dimensional
steady-states in open cavities
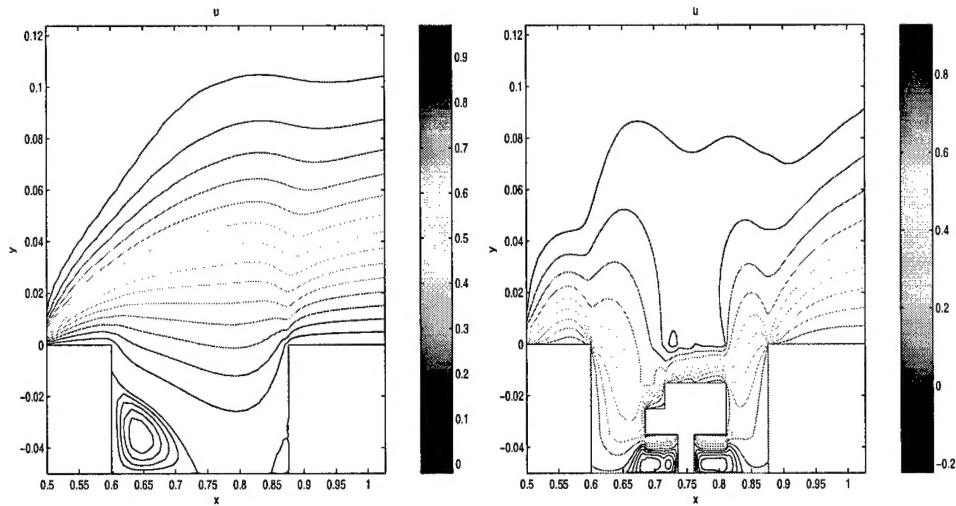
VASSILIOS THEOFILIS

March 2000

Spectral multidomain direct numerical simulations for the recovery of laminar two-dimensional steady-states in open cavities

BY VASSILIOS THEOFILIS †

Rohnsterrassen 14, D-37085 Göttingen, GERMANY
tel./fax: +49 551 48 76 25

(17 March 1999)

Our concern in this report is with two-dimensional laminar steady numerical solutions of the Navier-Stokes and continuity equations in open cavity geometries. Our ultimate objective is a nonparallel three-dimensional global linear instability analysis of these flows. Consequently, emphasis is presently placed on the accuracy of the obtained solutions, since the sensitivity of instability results on the details of the basic state is well known. The novelty of the spectral multidomain algorithm constructed for the basic flow calculations is that the iterations for satisfaction of solution continuity across domain interfaces and that for the nonlinearity of the governing system of equations are combined in a single step; order-of-magnitude savings in computing effort are thus materialised compared with the Dirichlet-Neumann approach in which the aforementioned two steps are nested within each other.

Results are presented, validating the proposed algorithm on both Poisson's equation and well-known solutions of the incompressible equations of fluid flow motion. Subsequently steady laminar incompressible flow solutions in the open cavity are presented. The modifications experienced by the steady flow pattern in the presence of a sizeable object inside the cavity is documented and conclusions concerning the global linear instability analysis of either problem are drawn. Issues concerning compressible flow simulations for the problem in question are highlighted.

Work which resulted from questions on the origin of numerical residuals in the course of steady-state numerical simulations, raised in the course of work performed on the present and Contract No. F61775-99 WE049, is submitted as an independent document with the request to have its suitability for a US Patent examined by the Air Force.

European Office for Aerospace Research and Development
©Vassilios Theofilis (1999)

1. Introduction

We report the results of our efforts to obtain spectrally accurate solutions pertaining to steady laminar flow in two-dimensional open cavities. This work is a pivotal step towards the target of a global linear instability analysis of this flow. In such an analysis the entire flowfield obtained herein must be used as the variable coefficients (so-called basic flow) in the partial-differential-equation-based complex nonsymmetric generalised eigenvalue problem in which the Navier-Stokes, continuity and, in compressible flow, the energy equations may be recast. Consequently, the quality of the expected solutions of the eigenvalue problem is conditioned by that of the steady laminar basic states and it is tempting to devote sufficient computing power to ensure the recovery of high-quality basic flow results. However, current hardware technology limits the maximum number of discretisation nodes on which the respective eigenvalue problem may be solved. This, in turn, results in the necessity for basic flow results to be obtained that are as accurate as possible on the limited number of discretisation points available. This latter requirement points at spectral methods as the natural choice for spatial discretisation. Conversely, relaxing the requirement of modest resolutions, one may obtain benchmark open cavity solutions at reasonable amounts of computing effort as one of the possible extensions of the present work.

In building up the individual elements of the algorithm used for the solution of the problem at hand we have followed a modular approach and present solutions to the issues arising in both incompressible and compressible flow. After presentation in § 2 of the spectral multidomain algorithm utilised, an iterative multidomain Poisson solver which forms the core of our incompressible multidomain direct numerical simulation (DNS) approach is validated in § 3 against two steady laminar flow problems and a solution recently presented in the Literature, obtained by an alternative spectral discretisation scheme. Our attention is subsequently focussed on the incompressible equations of motion and the issues of domain connectivity, boundary conditions and resolution necessary for results of predefined accuracy to be obtained are discussed in § 4 (a-c) by reference to well-known benchmark solutions of the equations of motion. Open cavity incompressible solutions at a variety of Reynolds number and aspect-ratio parameters are presented in § 4 (d). As a demonstrator of the potential of the multidomain algorithm proposed we recover solutions in a full-bay model of the open cavity; the strong qualitative differences of the flow pattern compared with the equivalent-sized empty open cavity is thus highlighted and conclusions regarding a possible subsequent global linear instability analysis of either problem are drawn. Issues of particular concern in compressible flow are discussed in § 5. While we have solved the initial-condition problem for compressible simulations, no compressible open-cavity solutions have been obtained so far; these will be presented in due course, after answers to the boundary-condition related issues raised herein have been addressed in a satisfactory manner. Concluding remarks and an outline of the several potential extensions of the present work are presented in § 6.

2. A spectral multidomain approach

(a) Spatial decomposition

The choice of spectral methods has been made on the grounds of their superiority over finite-difference or finite-volume methods in recovering solutions of optimal accuracy at modest resolutions. The nature of the domain in which we are interested renders single-domain spectral calculations impractical. Within the framework of spectrally-accurate solutions two options for the spatial discretisation of an open cavity are a spectral multidomain (Demaret and Deville 1991; Quarteroni 1991) or a spectral element (Patera 1984) domain decomposition. The first approach is well-suited for domains which may be decomposed in regular rectangular subdo-

mains; the second approach may either be formulated in rectangular subdomains or based on space triangulation and is thus more flexible than spectral multidomain in the reconstruction of arbitrarily-shaped domains, albeit in the presence of an efficient triangulation algorithm. Given the regularity of the geometry of the open cavity we use here spectral multidomain spatial decomposition based on rectangular subdomains. For consistency in what follows we refer to the N(orth), E(ast), S(outh) and W(est) boundaries and enumerate domains in a clockwise manner.

Rectangular open-cavity type of two-dimensional physical domains may be reconstructed by means of the $2^4 - 1$ rectangular subdomains whose sides result from permutations of open and closed boundaries less that subdomain whose four sides correspond to solid walls. These subdomains are depicted in Figure 1 and may be classified into four types, equal to the number of rows in Figure 1, according to the number and location of the open/closed sides in each domain. Using clockwise notation we start from the N boundary in each domain and denote a solid boundary by '1' and an open boundary by '0'. The subdomain whose four sides are open is thus denoted by 0000 and we call it a type A domain. The family of subdomains having three open sides has four members, 1000, 0100, 0010 and 0001 and is denoted as type B. The six subdomains having two open and two closed sides are 1100, 0110, 0011, 1001, 0101 and 1010 and are denoted as type C subdomains. Finally, the family of subdomains having three closed sides and denoted as type D has four members, 1101, 1110, 0111 and 1011. Using this notation a minimum of four subdomains, one of type A, two of type B (0010) and one of type D (0111) may be used to reconstruct a simple open cavity geometry, while eight subdomains may minimally be used to decompose space in the case of an open cavity including a protrusion, one of type A, five of type B and two of type D, as depicted in Figure 2.

(b) Physical boundary conditions for the incompressible equations of motion

Before addressing the issue of connectivity of the domains exposed in §2 (a) we discuss briefly the system of equations solved in incompressible flow in order for the issue of physical boundary conditions to be addressed and the distinction to be made between physical boundary conditions and numerical compatibility conditions necessary to close the system of equations in the present multidomain framework. If incompressible solutions are sought, the system composed of the relation between streamfunction ψ and vorticity ζ and the steady vorticity transport equation is solved,

$$\nabla^2 \psi + \zeta = 0, \tag{2.1}$$

$$\nu \nabla^2 \zeta + \left\{ \psi_y \zeta_x - \psi_x \zeta_y \right\} = 0, \tag{2.2}$$

in which ν denotes the kinematic viscosity of the fluid. The choice of the steady, as opposed to the unsteady version of the equations of motion, was made so that global two-dimensional amplified linear instabilities, potentially developing upon the sought laminar basic flow solutions, are not allowed to manifest themselves in the dynamics of a DNS which aims at recovery of steady-state laminar basic states (Theofilis 1999). Another point worthy of mention regarding the choice of the vorticity-transport equation as opposed to the primitive variable formulation concerns the savings expected to be made when solving two as opposed to three equations using potentially long expensive iterative procedures for the satisfaction of solution continuity across interfaces. From an academic point of view it is interesting to investigate spectral multidomain algorithms in the context of the vorticity transport equation, since multidomain solutions are typically obtained using primitive variables (Quarteroni 1991).

The physical boundary conditions associated with this system on solid walls are no-slip and no-penetration. In terms of the velocity components along the spatial directions x and y, respectively denoted by $\bar{u}$ and $\bar{v}$, *both* boundary conditions concern the streamfunction

$$\bar{u} \equiv \psi_y = 0, \quad \text{and} \quad \bar{v} \equiv -\psi_x = 0. \tag{2.3}$$

Substantial effort has been put into translating these physical boundary conditions on boundary conditions for vorticity in the context of finite-difference calculations (e.g. E and Liu 1996). In the present calculations on solid boundaries we impose *both* physical boundary conditions (2.3) on ψ and derive boundary conditions on ζ using (2.1).

Physical boundary conditions are also given at open boundaries. In the case of the open cavity defined in $x \in [x_0, x_\infty] \times y \in [y_0, \infty)$ one may distinguish between three types of physical boundary conditions, those imposed at the inflow boundary $x = x_0$, boundary conditions on the computational boundary $y = y_\infty$ which models the physical boundary $y \to \infty$ and, finally, boundary conditions at the outflow boundary $x = x_\infty$. The inflow boundary conditions for the present problem are given in terms of the streamfunction and the vorticity of flow on a flat plate at a given Reynolds number Re_{x_0}. At the N boundary of all relevant subdomains, $y = y_\infty$, flow is driven by $\bar{u} = 1$ and $\bar{v} = 0$ is imposed; Dirichlet and Neumann boundary conditions on ψ are used to impose these physical boundary conditions. At the outflow boundary $x = x_\infty$ information is extrapolated from the interior of the computational domain on the E boundary of the subdomain whose E side is at $x = x_\infty$. We will return to these points in in § 4 (a-c) and (d).

(c) Connectivity of the domains and numerical compatibility conditions

We focus the discussion on the open cavity geometry presented in the upper part of Figure 2, in which Roman numbering of the subdomains is used. We indicate interfaces by their position with respect to the domain followed by the number of the domain in brackets. The interfaces E(ii)/W(i), E(i)/W(iii) and S(i)/N(iv) between the non-overlapping domains (ii)/(i), (i)/(iii) and (i)/(iv), respectively, are artificially generated internal boundaries resulting from the spatial decomposition. A straightforward iterative algorithm is used to solve the governing equations in this geometry as follows.

The physical boundary conditions on the N, S and W boundaries of domain (ii) are complemented by arbitrarily chosen Dirichlet data on E(ii), the governing equations are solved in this subdomain and Neumann data on the interface E(ii)/W(i) are generated. The same approach is followed on domain (iii) in which (2.1-2.2) are solved subject to the physical boundary conditions on N, E, and S of this domain and arbitrary Dirichlet boundary values on W(iii) in order for Neumann boundary data to be generated on the interface E(i)/W(iii). Analogously, the (no-slip) physical boundary conditions on E, S, and W of subdomain (iv) are complemented by arbitrary Dirichlet data on N(iv), the governing equations are solved and Neumann boundary data on the interface S(i)/N(iv) are generated. The system (2.1-2.2) may now be solved in subdomain (i) subject to the *physical* boundary condition on N(i) and the *numerical* Neumann compatibility conditions generated from the solutions in the adjacent subdomains. The solution delivers Dirichlet data on E(i), S(i) and W(i), which are passed on to the adjacent subdomains (iii), (iv) and (ii) using relaxation according to

$$q^{(n)} = \omega q^{(n)} + (1 - \omega)q^{(n-1)} \tag{2.4}$$

where $(n-1)$ and (n) denote old and new iteration levels and ω is an $O(1)$ relaxation parameter. The process is iterated until convergence; at convergence C^1 continuity is attained on all interfaces. The algorithm has been found to converge rapidly in both the form discussed and also when Neumann data are chosen initially in subdomains (ii), (iii) and (iv) and Dirichlet values are used for the subsequent iteration in subdomain (i).

The proposed algorithm is the streamfunction/vorticity-transport analogon of the so-called Dirichlet-Neumann iterative scheme presented in the context of primitive-variables discretisation

of the equations of motion by Quarteroni (1991). In the case of two subdomains Ω_1 and Ω_2 with a common interface Γ one solves the independent problems

$$
\begin{cases}
\nabla^2 \psi_1^{(n)} + \zeta_1^{(n)} = 0, & \text{in } \Omega_1 \\
\nu\nabla^2 \zeta_1^{(n)} = g_1^{(n)}, & \text{in } \Omega_1 \\
\psi_1^{(n)} = \lambda^{(n-1)}; \ \zeta_1^{(n)} = \mu^{(n-1)} & \text{on } \Gamma \\
\\
\nabla^2 \psi_2^{(n)} + \zeta_2^{(n)} = 0, & \text{in } \Omega_2 \\
\nu\nabla^2 \zeta_2^{(n)} = g_2^{(n)}, & \text{in } \Omega_2 \\
\partial\psi_1^{(n)}/\partial n_\Gamma = \partial\psi_2^{(n)}/\partial n_\Gamma, \ \partial\zeta_1^{(n)}/\partial n_\Gamma = \partial\zeta_2^{(n)}/\partial n_\Gamma & \text{on } \Gamma
\end{cases}
\tag{2.5}
$$

and updates the Dirichlet data on the interface according to

$$
\begin{cases}
\lambda^{(n)} & = & \omega\psi_2^{(n)} + (1-\omega)\lambda^{(n-1)} \\
\mu^{(n)} & = & \omega\zeta_2^{(n)} + (1-\omega)\mu^{(n-1)}
\end{cases}
\tag{2.6}
$$

Depending on whether one solves the steady version of the equations of motion, as the case is here, or whether one solves the time-accurate problem the forcing functions are defined either by (2.2),

$$
g_1^{(n)} = -\left\{ \psi_{y,1}^{(n)}\zeta_{x,1}^{(n)} - \psi_{x,1}^{(n)}\zeta_{y,1}^{(n)} \right\} = 0,
\tag{2.7}
$$

$$
g_2^{(n)} = -\left\{ \psi_{y,2}^{(n)}\zeta_{x,2}^{(n)} - \psi_{x,2}^{(n)}\zeta_{y,2}^{(n)} \right\} = 0
\tag{2.8}
$$

or by (2.7-2.8) modified by the terms arising from a semi-implicit time-discretisation (Canuto *et al.* 1987). In the latter case the iterative procedure for the satisfaction of solution continuity across domain interfaces is nested into that for the time-stepping algorithm. The key difference between the Dirichlet-Neumann approach for the steady equations of motion and that for a time-accurate solution is that in the former case we do not distinguish between the iteration necessary for the satisfaction of solution continuity across domain interfaces and that which must be performed for the nonlinearity of the vorticity-transport equation.

Refinement of spatial discretisation at certain interesting parts of the flowfield (f.e. solid-wall junctions) is attained in either of two ways. First, retaining the spatial decomposition one refines resolution in the subdomains adjacent to the physical location of interest. Second, the subdomains in which refinement is required may be further decomposed into smaller subdomains, generating additional interfaces within the original subdomain and retaining the principle of utilising the physical boundary conditions in order to generate numerical compatibility conditions for the newly-generated interfaces. For example subdomain (iv) of Figure 2 (upper) may be decomposed into six subdomains, as shown in Figure 3. The solution here starts in a first step of a 'forward' iteration by assuming Dirichlet values on the NUW and NUE boundaries of the type C subdomains (c) and (e), respectively, solving the system of governing equations in (c) and (e) and generating Neumann data for the type B subdomains (b), (d) and (f). In a second step, the physical boundary conditions on the type B subdomains are complemented by the newly generated information on their S, E/W and S boundaries, respectively, and by arbitrary Dirichlet data values on N(b), W(b), N(d), N(f) and E(f) and the governing equations are solved. In a final step, the newly generated Neumann data on E(a), S(a) and W(a) are complemented by arbitrary Dirichlet data on N(a) and (2.1-2.2) are solved in this domain. This generates a new estimate of the solution derivative along the entire N(iv) boundary which may be used to solve for domain (i) in the global solution algorithm. This produces new function values along

N(f)∪N(a)∪N(b) and the flow of information may be reversed in a 'backward' local iteration within the original domain (iv).

3. Validation of the multidomain approach on the Poisson equation

At the heart of the numerical solution for (2.1-2.2) lies a spectrally-accurate Poisson solver. Before entering the details of the numerical solution of the Navier-Stokes and continuity equations we validate the procedure of § 2 (*c*) on the Poisson problem

$$\nabla^2 \psi = F(x, y) \tag{3.1}$$

for three different cases of integration domain, forcing function and associated boundary conditions.

(*a*) *Poisson's equation in a rectangular duct*

The first is calculation of the steady laminar flow in a rectangular duct presented by Tatsumi and Yoshimura (1990) in which the forcing is provided by the constant, pressure-gradient related term $F(x, y) = -2$. The rectangular integration domain in this case is defined by $x \in [-A, A] \times y \in [-1, 1]$, where A is the duct aspect ratio. The boundaries in this example are taken to be solid walls, on which the viscous boundary conditions are applied. Space is discretised by the union of three subdomains, the 1011 D-type subdomain $\left\{ x \in [-A, x_L] \times y \in [-1, 1] \right\}$, the 1010 C-type subdomain $\left\{ x \in [x_L, x_R] \times y \in [-1, 1] \right\}$ and the 1110 D-type subdomain $\left\{ x \in [x_R, +A] \times y \in [-1, 1] \right\}$. The interfaces are chosen at $x_L = -0.5A$ and $x_R = 0.25A$ and all subdomains are discretised using Legendre Gauss-Lobatto collocation points to resolve the $x-$ and $y-$spatial directions by Nx and Ny points, respectively. Results for the streamfunction at $(x_L, 0), (0, 0)$ and $(x_R, 0)$ and its first derivative ψ_x at $(x_L, 0)$ and $(x_R, 0)$ as function of resolution is shown in Table 1 for two aspect ratios, $A = 3$ and 4. Note that the magnitude of $\psi_y(x_L, 0), \psi_x(0, 0), \psi_y(0, 0)$ and $\psi_y(x_R, 0)$ is $< 10^{-14}$. Converged results which agree in all significant digits with those presented by Tatsumi & Yoshimura (1990) may be obtained using 16 collocation points per spatial direction in each subdomain and $\omega = 0.5$. Our result for ψ in the union of the three subdomains is presented in the form of eleven contours from 0 to $\max(\psi)$† in Figure 4, where the absence of any sign of discontinuity at the interfaces is visible.

The efficiency of the present algorithm derives from two facts; firstly, a spectrally-accurate solution is obtained in this problem by solving linear systems defined by dense matrices whose leading-dimension is $Nx \times Ny$ as opposed to $3 \times Nx \times Ny$ that would have been necessary for a single-domain calculation at the same resolution. Second, the small number of iterations necessary for $|\psi^{(n+1)} - \psi^{(n)}|/|\psi^{(n+1)}| < 10^{-14}$, also displayed in Table 1, justifies the use of an iterative scheme on the three small rather than a direct scheme on a single large problem. In the latter problem one order of magnitude larger memory and two orders of magnitude longer runtime, compared with those for solution in a single subdomain, would have been necessary using direct inversion. Representative results for the CPU time necessary for convergence using a single PII 300MHz processor are also shown in Table 1. Shown are two numbers, one corresponding to the total cost of the LU-factorisation of the three implicit matrices corresponding to the three subdomains and the iteration itself and a second showing the latter cost alone. It is clear that most of the time is spent in the one-off factorisation, the results of which are stored and used during the iteration. The iterative approach itself is parallelisable, which may reduce the cost of the iteration process further.

† Contour level 0 is the wall itself, while a single point in the centre of the domain corresponds to the contour $\psi = \max(\psi)$

(b) *Poisson's equation in a grooved-channel geometry*

The second validation case for the algorithm of § 2 (c) is the Poisson problem (3.1) subject to the same forcing function and boundary conditions but solved in the domain of the open cavity. Aside from testing the performance of the algorithm on the actual domain in which the flow solutions are to be obtained, the objective here is firstly to test the symmetries present in the solution if a symmetric integration domain is chosen and secondly to assess the level of discretisation necessary in order for solutions to converge within predefined tolerance in a domain containing geometric singularities. Space is discretised by the union of the three D-type subdomains $\{1011: \ x \in [-1, -0.75] \times y \in [0,1]\}$, $\{0111: \ x \in [-0.5, 0.5] \times y \in [-1, 0]\}$, $\{1110: \ x \in [0.5, 1] \times y \in [0,1]\}$, with the C-type subdomain $\{1010: \ x \in [-0.75, -0.5] \times y \in [0,1]\}$, and the B-type subdomain $\{1000: \ x \in [-0.5, 0.5] \times y \in [0,1]\}$. Of particular interest is the performance of the algorithm in the presence of the discontinuities at $(x_L, y_L) = (-0.5, 0)$ and $(x_R, y_R) = (0.5, 0)$. Results for the streamfunction ψ and its first derivatives along the spatial coordinates ψ_x and ψ_y are shown in Figures 5–7; the symmetry of the solution about the geometrical line of symmetry $x = 0$ is evident. Results for ψ, ψ_x and ψ_y at six x−locations along $y = 0.5$ as a function of resolution, which was kept the same in the five subdomains, are shown in Table 2. The most striking observation is that despite the presence of the physical discontinuities in the integration domain convergence of the spectral method is exponential, showing reduction of residuals by an order of magnitude when doubling the number of collocation points in each spatial direction. A resolution of 16 collocation points per spatial direction in each subdomain is sufficient to produce results whose relative discrepancy from the result at the highest resolution is less than 0.05%. On the other hand, unlike the case of the rectangular duct, the presence of corner points in this problem results in at least 64 collocation nodes being necessary for residuals less than 10^{-5} to be obtained. The same message is conveyed by the small but nonzero values of ψ_x on the line of symmetry $x = 0$ where the latter quantity assumes values of $O(10^{-8})$ at the highest resolution and also by the difference between function or derivative values at a point and its mirror image with respect to the geometric line of symmetry $x = 0$. Such discrepancies in a basic flow are well within the bounds of acceptability for accurate linear instability analysis results to be obtained. Our conclusion here is that the spectral multidomain algorithm of § 2 (a − c) is able to handle the target grooved channel geometry, albeit at the cost of rather large number of discretisation points; we will return to this point in the context of simulations of the Navier-Stokes and continuity equations. Given the well-established property of a spectral method to deliver results of comparable accuracy with those of a second-order accurate finite-difference or finite-volume method at approximately an order of magnitude less number of discretisation points per spatial direction, the present results may be used as guidance for the number of discretisation points necessary for a second-order accurate method to deliver results in the problem in question of accuracy comparable with that of the present spectral scheme.

(c) *Poisson's equation in a backward-facing step geometry*

The final validation case for the multidomain algorithm before turning to the equations of motion is that discussed by Black (1997). The integration domain here is the classic backward-facing step geometry and the novelty compared with the previous two validation cases is the open domain boundary conditions. The integration domain is decomposed into two B-type subdomains $\{0010: \ x \in [-\pi, 0] \times y \in [\pi/2, \pi]\}$ and $\{0001: \ x \in [0, 2\pi] \times y \in [0, \pi/2]\}$ and an A-type subdomain $\{0000: \ x \in [0, 2\pi] \times y \in [\pi/2, \pi]\}$. The forcing function in (3.1) is a constant equal to unity and the boundary conditions are

V. Theofilis

x	y	$\psi(x,y)$	
$[-\pi, 2\pi]$	π	0	(3.2)
2π	$[0, \pi]$	$\psi_x = 0$	(3.3)
$[0, 2\pi]$	0	$(\pi/2)^3/6$	(3.4)
0	$[0, \pi/2]$	$(\pi/2)^3/6$	(3.5)
$[-\pi, 0]$	$\pi/2$	$(\pi/2)^3/6$	(3.6)
$-\pi$	$[\pi/2, \pi]$	$(\pi - y)^3(y/3 - \pi/12).$	(3.7)

Only graphical results are presented by Black (1997); nevertheless, to the degree that results may be compared visually, the agreement seen between hers and our result for ψ, to be found in Figure 8, is satisfactory. Additionally in this figure we present the first derivatives of the solution in none of which evidence of discontinuity of the solution at interfaces can be found. The function and first derivative values at the midpoints of the interfaces, $(x,y) = (\pi, 0)$ and $(x,y) = (0, 3\pi/4)$, may be found in Table 3. Overall the solution converges faster on the former, compared with the latter point. Both converge exponentially, although a number of collocation points higher than 64 per spatial direction is found to be necessary if convergence beyond the fourth decimal place is desired. With the spectral multidomain approach validated on the Poisson problem in nontrivial geometries, we now turn our attention to the solution of the system (2.1-2.2).

4. The incompressible equations of motion in two spatial dimensions

As it has been stressed already, in view of the global linear instability analysis which will ultimately follow the present work, restrictions are placed upon the maximum total number of discretisation points that can be used to solve for the steady laminar basic flow. Emphasis is consequently placed here on assessing the minimum number of collocation points by which converged steady laminar solutions may be obtained within the framework of a spectral multidomain discretisation. Issues which have to be tackled for the solution of the system governing fluid flow motion, additionally to those discussed above, are the following. First, the extension of the iterative algorithm for the satisfaction of solution continuity across domain interfaces to systems of equations must be validated. Second, the points raised regarding the physical boundary conditions as opposed to the numerical compatibility conditions discussed in § 2 $(b - c)$ deserve elaboration in the context of fluid flow simulations. Third, physical boundary conditions pertinent to open/solid boundaries must be discussed in the present spectral multidomain framework. Finally, the nonlinearity of the system of the governing equations introduces in principle an additional iteration besides that necessary for the satisfaction of continuity of the solution across subdomain boundaries. The relative performance of our algorithm, in which this additional iteration is circumvented, against an algorithm which uses an outer iteration for the nonlinearity (and potentially the time-advancement) and a nested inner iteration based on the Dirichlet-Neumann algorithm for the satisfaction of solution continuity across interfaces must be assessed. These issues are addressed below, where we expose the properties of the proposed algorithm by discussion of its performance on analytically and numerically well-known fluid flow examples. Steady laminar flows in a plane channel, the lid-driven cavity and the Blasius boundary layer are discussed before solutions to the open cavity problem are presented.

(a) Plane Poiseuille flow

The first building block of the algorithm which we wish to validate is our approach to the boundary conditions imposed at free-boundaries. To this end a single-domain calculation with one free-boundary, that at outflow, is performed. Plane Poiseuille flow (PPF) is an ideal test case for this problem since its analytical results serve both as inflow boundary conditions and as test for the returned numerical solution in the entire domain. In view of the (ψ, ζ) formulation used herein one preprocessing step is necessary, that of provision of an analytical functional form for ψ. We take a single domain in which $x \in [-2, 3]$ denotes the arbitrarily chosen extent of the downstream spatial direction and $y \in [-1, 1]$ is taken to be along the wall-normal spatial direction. Fortuitously in this flow the physical domain of interest and the standard Chebyshev Gauss-Lobatto grids (Canuto *et al.* 1987) coincide and no mapping of the computational coordinate is necessary in the wall-normal direction. It is also worthy of mention is that the spatial homogeneity of this problem is *not* exploited by use of a Fourier decomposition of flow quantities along the streamwise spatial direction but, rather, a Jacobi polynomial expansion which permits recovery of arbitrary solutions is used. It is left to the dynamics of the flow to select the correct (homogeneous) solution.

Assuming a downstream pressure gradient $p_x = -2/Re$ analytically results in the classic parabolic profile for $\bar{u}(x, y) = 1 - y^2$, while $\bar{v} \equiv 0$. The definition of $\bar{u} = \psi_y$ may be integrated once to provide

$$\psi(x, y) = \frac{2}{3} + y - \frac{1}{3}y^3, \tag{4.1}$$

where the choice $\psi(x, y = -1) = 0$ has been made. The flow vorticity is also known analytically,

$$\zeta(x, y) = 2y. \tag{4.2}$$

The algorithm solves the Poisson problem (2.1) for ψ, given a delayed ζ field subject to the boundary conditions of Table 4. At inflow Dirichlet boundary conditions for ψ, provided by eq. (4.1), complement the boundary condition $\bar{v} = -\psi_x = 0$ while at outflow the prescription of Briley (1971) is used, which was presented as a boundary-layer approximation. It is interesting to assess its performance in the context of the present low-Reynolds number Navier-Stokes spectral multidomain simulations. On solid walls the viscous boundary conditions are imposed on ψ either directly for u ($\psi_y = 0$) or indirectly for v by specifying a constant ψ value obtained by (4.1). With the solution of ψ known at the new iteration level (2.2) is also written as a Poisson problem in which the nonlinear right-hand-side forcing may be constructed using current-level information on ψ and ζ data which are delayed by one iteration; the Poisson problem for ζ may then be solved subject to the compatibility conditions for ζ also shown in Table 4. Note that only one outflow boundary condition is required on this quantity, the other being imposed on ψ at this boundary and all physically available information being incorporated in the streamfunction boundary conditions. A variant of the present algorithm would solve a coupled problem for ψ and ζ in which information on the forcing term alone would be delayed by one iteration. However, both the accuracy and the convergence rate of results of single domain calculations are such that the higher cost of a coupled solution is not justified.

Single-domain calculation results converge quickly to the parabolic profile for the streamwise velocity component and the linear dependence of vorticity on the wall-normal coordinate throughout the entire domain. Most significantly, this result has been found to be independent of the arbitrary extent of the integration domain in the streamwise direction x and the resolution of the wall-normal direction y, provided that the latter exceeds 8 collocation points. The rate at which the analytical results are obtained is a function of the Reynolds number, with lower

Re-values resulting in increasing diagonal dominance of the matrix discretising the Laplacian operator in (2.2) and quicker convergence compared with higher Reynolds number results. The most significant finding of this test-case, though, concerns the boundary conditions treatment. Use of equation (2.1) was found to deliver machine-precision agreement with the analytically known inflow boundary condition for ζ; results obtained on this problem provide justification for use of Briley's outflow boundary treatment in all subsequent simulations.

The same problem is tackled next using our multidomain approach in which space is discretised by two 1010 C-type subdomains

$$\Big\{x \in [-3, 0] \times y \in [-1, 1]\Big\} \cup \Big\{x \in [0, 2] \times y \in [-1, 1]\Big\}.$$

The boundary conditions of Table 4 are used at the N, S and W boundaries of the first and the N, E and S boundary of the second subdomain, respectively. At the interface compatibility conditions ensuring continuity of ψ and its first derivative close the Poisson problems to be solved for the streamfunction, while compatibility conditions based on (2.1) are used for ζ in both subdomains. Again, the analytical results are obtained to within machine-precision. Iteration history results for the streamfunction, the streamwise velocity component and the (constant throughout the integration domain) wall-normal derivative of the flow vorticity against the time-like variable τ, related with the number of iterations performed N and the relaxation parameter ω through $\tau = \omega N$, are presented in Figure 9; $\bar{u}$ and ζ are presented in Figure 10. As has been mentioned, results were obtained by iteratively exchanging function and first-derivative information between domains at interfaces. The interesting observation here is that the approach of absorbing the iteration for the nonlinearity within that for satisfaction of solution continuity at interface boundaries saves an order of magnitude of computing effort in comparison with an approach which uses nested iterations for solution continuity within those for the nonlinearity of the governing equations.

(b) The lid-driven cavity

The next test case is the classic lid-driven cavity flow. This flow serves as a testbed for new numerical algorithms and has extensively been simulated in the past in its own right and on account of the analogies between the lid-driven and the problem of interest here, that of flow in an open cavity, in which the shear-layer at the lip of the open cavity acts as the lid driving flow inside the cavity. Recently, Theofilis (2000) has demonstrated excellent agreement between the frequency of the most unstable global linear mode calculated by the novel global linear instability analysis technique and that measured in a careful series of experiments (Aidun *et al.* 1991; Benson and Aidun 1992). One of the objectives of the present study is to compare the steady laminar basic flow patterns in the lid-driven and the open cavity in order to draw indirect conclusions upon the expected global linear instability behaviour of the open cavity problem before embarking upon the computationally intensive global linear instability analysis in the open cavity.

The spectral multidomain algorithm discussed is applied to the lid-driven cavity problem, discretising space using the union of a 1011 and a 1110 D-type domain,

$$\Big\{x \in [0, 0.5] \times y \in [0, 1]\Big\} \cup \Big\{x \in [0.5, 1] \times y \in [0, 1]\Big\}.$$

Simulations were performed at several Reynolds numbers and correspondingly increasing resolutions; the boundary conditions imposed are shown in Table 5. Excellent agreement with the benchmark results of Schreiber and Keller (1983) has been obtained. Interestingly, these authors provide vortex core position and strength results as a converging series of Richardson-extrapolated data. The maximum relative discrepancy of our calculations at $Re = 4000$ from their results is $< 0.3\%$. Such an agreement could only be obtained by using in excess of 32 spectral collocation points per spatial direction on account of two factors. First, the boundary layers

forming in the vicinity of all four solid surfaces and in particular in the salient corners need to be adequately resolved. Second, the singularity of the boundary conditions at the lid endpoints requires placement of sufficient gridpoints in the vicinity of $(x, y) = (0, 1)$ and $(1, 1)$. Plots of the streamfunction, vorticity and velocity components at $Re = 100$, obtained using 48^2 Chebyshev collocation points per subdomain can be seen in Figure 11. Despite the satisfactory agreement obtained between benchmark results and the present calculations, it has been observed in this nontrivial solution of the equations of fluid motion that a relatively large number of collocation points in each subdomain is required in order for convergence of the algorithm to be achieved.

(c) The Blasius boundary-layer

The Blasius boundary-layer flow is recovered next by application of the spectral multidomain technique proposed. This flow is interesting in a twofold manner in the context of the open-cavity calculations. First, from a numerical point of view the issue of boundary conditions in an open system in conjunction with the proposed iterative spectral multidomain algorithm must be addressed. Second, the flat-plate boundary layer constitutes the flow upstream of the open-cavity solutions to be discussed shortly and as such we wish to ensure that it is well captured in its own right. With hindsight, the results obtained in this section have highlighted the potential sources of errors particular to open systems, introduced in the solution by application of the multidomain algorithm to this type of flows.

We have solved the equations of motion on rectangular domains

$$\left\{ x \in [x_{in}, x_{out}] \times y \in [0, y_\infty] \right\}$$

with x_{out} chosen to be located subcritically with respect to Tollmien-Schlichting (TS) instability (Schlichting 1979). Failure to satisfy this condition is expected to result in amplification of two-dimensional small-amplitude wave-like disturbances which, depending on the length of the integration domain, will manifest themselves in the DNS in the inability to obtain a converged steady-state (Theofilis 1999). Our intention in terms of the open-cavity solutions to follow is to ensure that the only source of unsteadiness originates from linear instability of the cavity itself and not from additional instabilities of different physical origin. To this end we chose $\bar{u}_\infty = 1, x_{in} = 0.5, x_{out} = x_{in} + 100\delta^*_{in}$ and $\nu = 1.7 \times 10^{-5}$ in SI units. This results in (dimensional) displacement-thicknesses of the boundary layer $\delta^*_{in} \approx 0.005$ and $\delta^*_{out} \approx 0.007$ at inflow and outflow, respectively; the corresponding Reynolds numbers are $Re_{in} \approx 295$ and $Re_{out} \approx 417$ while the well-known critical Reynolds number for TS-amplification is $Re^*_\delta \approx 520$ (Tollmien 1929). The wall-normal direction was resolved by mapping the Chebyshev Gauss-Lobatto points $\eta \in [-1, 1]$ onto the physical coordinate y using

$$y = l \frac{1 - \eta}{1 + s + \eta}. \tag{4.3}$$

Here $l = y_c(y_\infty - y_0)/(y_\infty - y_0 - 2y_c), s = 2l/(y_\infty - y_0)$, half of the total number of collocation points in the wall-normal direction are placed between the wall $y_0 = 0$ and $y_c = (y_\infty - y_0)/d$, the parameter d takes values between 3 and 5; the outflow boundary is placed at $y_\infty \approx 0.06$.

After obtaining converged solutions of the governing equations using single-domain computations and as few as 16 collocation points per spatial direction, the system (2.1-2.2) was solved in two B-type 0010 subdomains,

$$\left\{ x \in [x_{in}, x_c] \times y \in [0, y_\infty] \right\} \cup \left\{ x \in [x_c, x_{out}] \times y \in [0, y_\infty] \right\}$$

subject to the following boundary conditions. At inflow the Blasius solution at x_{in} was calculated using a Newton-Kantorowitz spectral iterative approach (Boyd 1989) on the same wall-normal grid as the subsequent Navier-Stokes calculations were performed, in order to avoid the intro-

duction of interpolation-related error when transferring the boundary-layer data onto the DNS grid. The profiles obtained were then used as inflow boundary conditions for ψ and ζ. At the far-field we imposed $\psi_y = 1$ and $\zeta = 0$. At the wall the usual viscous boundary conditions $\psi = \psi_y = 0$ were imposed on ψ and none on ζ. At the outflow boundary x_{out} the conditions $\psi_{xx} = 0$ and $\zeta_{xx} = 0$, already validated on the plane Poiseuille flow, were imposed. Continuity of the solution and its derivatives was ensured at the interface boundary, the latter placed at $x_c = x_{in} + (x_{out} - x_{in})/2.5$. In a manner analogous with the calculations in the lid-driven cavity, the resolution of the boundary layer requires an adequate number of points resolving the boundary layer. On the other hand, it is interesting in the context of the present calculations to obtain solutions within a predefined low tolerance on as small a total number of points as possible; this requirement was elemental in the decision to use spectral methods for the discretisation of the governing equations. It is well-known from single-domain calculations that at high resolutions these methods suffer from severe CFL-related time-step limitations when time-accurate solutions are obtained, and very small relaxation parameters in the context of iterative solution approaches. As a matter of fact, the largest time-step permitted scales with the fourth power of the smallest grid-spacing (Canuto *et al.* 1987) while an analogous situation pertains to the relaxation parameter. Consequently, very high resolution runs are quite expensive to obtain in general. The cost is aggravated in the context of the present multi-domain calculations on account of the iteration process necessary for continuity of the solution at the interfaces to be ensured.

With these considerations in mind, solutions on grids comprising 12^2, 16^2, 32^2 and 48^2 collocation points in each subdomain were obtained. In Figure 12 we present a local convergence history of the ψ and ζ solutions obtained on the coarsest grid at the midpoint of the first integration subdomain against the time-like variable τ; monotonic convergence of both quantities is demonstrated. Also shown is the collapsing of the calculated solution onto the Blasius profile. Three stations are shown, firstly $x = x_{in}$, where the Blasius solution is imposed as an inflow boundary condition for the first domain, secondly the calculated solution at the domain interface $x = x_c$ and thirdly the calculated solution at $x = x_{out}$. It is worthy of mention that the collapsing of the solutions obtained is quite adequate even at this coarse resolution.

However, an interesting situation arose on grid refinement of the coarsest resolution results. While the 12^2 calculations converged monotonically, prior to convergence the 16^2 results exhibited an oscillatory behaviour in the downstream subdomain, the amplitude of which increased with the number of iterations until divergence of the simulation; the same behaviour has also been observed as a result of too high a relaxation parameter ω, in which case instability appears without convergence having been approached. A typical result of the in-phase oscillations of ψ and its derivatives in the latter case is shown in Figure 13. Several potential causes of this behaviour, which is absent in the context of single-domain calculations *using the same domain extent and the same resolution*, were examined and extensive experimentation was performed at a given extent of the integration domain with different grid-refinement, iteration parameters and outflow boundary conditions alternative to those used in the examples presented so far. As a matter of fact a modest increase of the resolution and decrease of the associated ω had no influence neither on the pattern seen in Figure 13 nor on its frequency, leading us to examine the possibility of the instability being of physical origin. Although in the parameter range examined Tollmien-Schlichting instability gives rise to decaying waves alone, if TS waves were present in the flow they would manifest themselves at conditions of linearity, i.e. near convergence of the basic flow to a steady state, in line with the observations made. On the other hand, the absence of instability in single-domain calculations points at the origin of the oscillations being of numerical nature, associated with the existence of an interface in the integration domain. Further, it may be conjectured that the practically absent dissipation of a spectral scheme results in catastrophic amplification of the numerically generated instability. Such a behaviour might have

been absent if a spatial discretisation scheme with inherent dissipation higher than that of the spectral method were used.

We first eliminate the possibility of the outflow boundary conditions being responsible for the phenomenon observed. To this end, we artificially stabilise the outflow region by using a buffer-domain approach, in which the convective terms of the governing equations are smoothly reduced to zero. This technique has been used successfully by a number of investigators dealing with spatial direct numerical simulation of transitional and turbulent flows (Spalart 1988, Rist *et al.* 1996). The function used to achieve this purpose in the context of the present simulations is

$$\lambda(x) = 0.5\left[1 + \tanh\frac{s - x}{\beta}\right], \qquad (4.4)$$

where $s = x_c + \alpha(x_{out} - x_c)$ with α determining the location $s \in [x_c, x_{out}]$ around which the hyperbolic tangent function is centred. The parameter β determines the slope in the hyperbolic tangent function and ensures that a given streamwise grid resolves $\lambda(x)$ well. The governing equations are then modified, replacing (2.2) by

$$\nu\nabla^2\zeta + \lambda(x)\left\{\psi_y\zeta_x - \psi_x\zeta_y\right\} = 0, \qquad (4.5)$$

which delivers unphysical solutions for (ψ, ζ) in the part $x \in [s, x_{out}]$ of the second subdomain in favour of stable solutions upstream of $x = s$. While one wishes to have $s \to x_{out}$ and a steep slope of the hyperbolic tangent function, there are limitations to the extend that the buffer-domain approach may be used such that it fulfills its purpose to damp outflow oscillations and at the same time is not too wasteful in terms of the collocation points devoted to resolving λ as opposed to solving the governing equations. Several experiments performed using this technique have improved the quality of the transient solutions compared with the untreated outflow boundary. However, at modest resolutions the buffer treatment failed to deliver a satisfactory solution of the issue of numerical instability in the downstream subdomain near convergence of the simulation.

We have established three possible remedies of the numerical instability problem. The first, least satisfactory, solution is use of extremely small ω values. At the present conditions and a resolution of 16^2 collocation points in each of two subdomains a value $\omega = 10^{-6}$ appears to alleviate the problem. While no discontinuity of the solution at the domain interface may be found after a large number of iterations, traces of the instability in question may still be found in the solution, as seen in Figure 14. The solution shown is converged to a relative discrepancy between successive iterates of $< 10^{-9}$. However, owing to the cost of the iterative approach with such a small value of ω further iterations aiming at reducing this tolerance value to machine-accuracy levels were not performed and it remains unclear whether the instability in question will ultimately manifest itself in the solution. The second means found to improve the behaviour of the solution is shifting the inflow location of the integration domain x'_{in} upstream of the location $x_{in} = 0.5$. One may choose to retain the outflow location x_{out} in its original position or shift it to $x'_{out} < x_{out}$, effectively solving a different problem. In the first case the instability appears and eventually destroys the simulation, while in the second case converged solutions may be obtained after a small number of iterations which depends on the location of the new outflow boundary x'_{out}. Since TS-waves are more stable in $x \in [x'_{in}, x'_{out}]$ than in $x \in [x'_{in}, x_{out}]$, the latter observation may suggest a coupling between physical instabilities and the iterative approach for satisfaction of solution continuity at the interface as being responsible for the observed numerical instability.

Finally, the most effective way found to eliminate the numerical instability of the type shown

in Figure 13 is to increase resolution to the levels used for the singular lid-driven cavity problem or the Poisson problems in the geometries with a corner singularity. Results have been obtained discretising space by means of two 0010 B-type subdomains in each of which 48^2 spectral collocation points have been used. The Dirichlet-Neumann algorithm discussed was used at the interfaces and no use of the buffer-domain technique has been made (i.e. $\lambda(x) = 1$ in (4.5)). The convergence history, obtained with a modest value of $\omega = 10^{-4}$ may be found in Figure 15 and the spatial distribution of the solutions is shown in Figure 16. No traces of numerical instability may be found in neither the solution for ψ itself nor in its streamwise derivative $\psi_x \equiv -v$ at the interface, while continuity of u naturally follows from that of ψ and v; an analogous situation pertains for the flow vorticity ζ. The collapsing of the calculated solutions in both the 16^2 and the 48^2 calculations onto the Blasius profile is shown in Figure 17.

In summary, it appears that a coupling between physical instabilities and the iterative algorithm for the satisfaction of continuity at interfaces is responsible for the observed numerical instability at modest resolutions. This phenomenon is absent in single-domain calculations, where less collocation points are in general necessary in order to obtain solutions of analogous quality and gives rise to the investigation of alternative schemes for the satisfaction of solution continuity at the interfaces, for example Neumann-Neumann or Robin in combination with either Dirichlet or Neumann transmission interface conditions as an extension of the present work. In the context of the present simulations the most satisfactory remedy was found to be an increase of the number of collocation points to a level analogous to that at which satisfactory solutions were obtained in the lid-driven cavity, as far as the equations of fluid motion are concerned, and to that at which converged solutions of the Poisson equation in the grooved-channel and the backward-facing step geometry were obtained.

(d) Open-cavity steady laminar solutions

The experience gained with the spectral multidomain scheme in the problems addressed is next utilised to obtain solutions in the open cavity. The geometry of the domain including some of the parameters of the problem is shown in Figure 18. The fluid is taken to be air, with a kinematic viscosity of $\nu = 1.7 \times 10^{-5}$ in dimensional SI units and flow is taken to be driven by a constant dimensional free-stream velocity $\bar{u}_\infty = 1$ under zero streamwise pressure-gradient conditions. The control parameter for the solutions obtained is the flow Reynolds number, an increase of which may be interpreted as downstream shifting of the open cavity at the same free-stream velocity or increase of the latter with the cavity being kept at a fixed location. Other parameters on which the solution depends are the lengths x_L and x_R which determine the Reynolds number at the upstream lip of the cavity and at the outflow of the integration domain, as well as the depth D and length L using which the two cavity Reynolds numbers $Re_L = \bar{u}L/\nu$ and $Re_D = \bar{u}D/\nu$ may be defined. In line with the argumentation used for the Blasius flow with respect to subcriticality to TS instability we ensure that the Reynolds numbers of the flow at the inflow boundary and at the upstream lip of the open cavity is kept within the known bounds. The choice of the parameters L and D, on the other hand, has been shown experimentally to be crucial for the type of flow state to be expected, laminar, transitional or turbulent (Sinha *et al.* 1982). Accordingly, the values of both L and D as well as that of the outflow location $x_{out} = x_{in} + x_L + L + x_R$ must be restricted, such that steady laminar flow exits the integration domain. Without attempting to match their (different) conditions, we have used the works of Sinha *et al.* (1982) and Gatski and Grosch (1984) for some guidance with respect to the choice of x_L, x_R, L and D.

The spectral multidomain algorithm used in the open cavity employs a domain decomposition analogous to that of § 3 (*b*) although here four subdomains have been used to discretise space, two 0010 B-type, one 0111 D-type and one A-type subdomain as shown in Figure 2 (upper). The domain mapping in the wall-normal coordinate in the B-type subdomains is (4.3) used for

the calculation of the Blasius flow. We used either our algorithm, which does not distinguish between iteration for the nonlinearity and that for solution continuity across interfaces or the classic Dirichlet/Neumann approach which incorporates the latter within the former iteration. Convergence of the solutions in the present context has been ensured in a threefold manner. First, continuity of the solution across domain interfaces was enforced in an inner iteration of the Dirichlet-Neumann algorithm until the jump across interfaces was of the level of machine accuracy. Second, results of relative discrepancy below preset tolerances were obtained as the grid was refined; a typical value used was a relative change of less than 0.1% between two successive grid refinements. Third, the outer iteration for the nonlinearity was pursued until the relative changes in the solution were of the $O(10^{-6})$.

(i) SQUARE CAVITY SOLUTIONS

Steady-state solutions have been obtained in the open cavity in the Reynolds number region examined, Re $\in [50, 5000]$. The spatial convergence of the solutions has been assessed by grid refinement using 8^2 to 32^2 collocation points in each subdomain. The iteration process converged quickly at all resolutions; the iteration history using 20^2 collocation points in each subdomain is shown in Figure 19. The fact that all solutions were obtained using $\omega = 0.1$ is a demonstration of the robustness of the multidomain algorithm proposed, using which solutions may be obtained in less than 10^3 iterations at the low Reynolds numbers and twice that number at the higher Re$-$values. Global and local convergence criteria were used; in Table 6 we present the maximum value of u at $(x = x_{\mathrm{inf}} + x_L + L/2, y = 0)$ where it may be seen that the relative discrepancy between the results at the two highest resolutions is less than 0.1%. The spatial distribution of the incompressible open-cavity results obtained is shown in terms of isolines in Figures 20–23. Worthy of mention in these figures are a number of facts. First, in all solutions obtained there are no signs of discontinuities at domain interfaces. Second, the outflow boundary conditions used for the Navier-Stokes solutions discussed so far perform equally well in the present problem, despite its strongly elliptic nature. This is the result of the re-establishment of attached laminar boundary-layer flow at the outflow boundary; these boundary conditions may not perform equally well in case separated flow reaches the outflow boundary as a result of further increase of the Reynolds number; this is one of the questions of academic and practical interest, which may be posed for further investigation in a possible extension of the present work. Third, the boundary-layer approximation used to obtain inflow data becomes progressively more applicable as the Reynolds number is increased, while at low Reynolds numbers the DNS-obtained result at the neighbourhood of the inflow boundary quickly departs from the boundary-layer solution imposed at inflow. Fourth, an examination of the flowfields obtained reveals that an increasingly large level of interaction between flow outside and that inside the cavity takes place as a result of an increase in the Reynolds number; at the same time the shear-layer emanating from the upstream lip of the cavity is strengthened, as may be visually appreciated in the vorticity results.

In the steady solutions obtained no indication of the known from experiment oscillation of the flow between the upstream and the downstream vertical walls of the cavity has been observed. However, an interesting situation related to this phenomenon arose with a further increase of the Reynolds number to Re = 6000; the result may be found in Figure 24. Using the same resolutions as in the lower Reynolds number simulations we observed that upwards of 20^2 collocation points in each subdomain were necessary for converged steady-state solutions to be obtained. At lower resolutions the simulation became unstable, indicating that the number of discretisation points is too low to resolve the gradients in the flow. Interestingly, though, an explosive instability of the algorithm occurred only at the lowest resolution used, 12^2, while when using 16^2 collocation points in each subdomain *periodic* non-physical solutions were obtained. The solution then appeared to oscillate between the upstream and downstream vertical walls of the cavity while every signal built with either local or global quantities appeared to pertain

to a limiting cycle. In the absence of the higher resolution results one could misinterpret this behaviour as the onset of physical unsteadiness in the cavity. We ensured that this observation is related to low resolution and is not an artifact of too-high ω values by experimenting with the latter parameter. The results of Figure 24 were qualitatively repeated when ω values half and an order-of-magnitude smaller than that used in Figure 24 were employed. Worse, by experimenting with the value of ω at a given resolution, 16^2, we were able to obtain solutions which (in a time-accurate framework) may be interpreted as bearing all the hallmarks of limiting-cycle behaviour. The iteration history obtained using $\omega = 0.01$, in which the in-phase oscillations of the solution components are clearly visible, is shown in Figure 25. The altogether plausible result for the corresponding velocity components is shown in Figure 26; this bears little resemblance to the true solution obtained using upwards of 20^2 collocation points per subdomain, also shown in this figure. Even more curiously, at the lower resolution of 8^2 collocation points in each subdomain, the iteration process converged quickly to a steady-state solution which may be discarded as unphysical only on the grounds of comparison with the high-resolution results. Summarising the results of our experimentations beyond Re = 6000 we note that, aside from the well-known need for grid-convergence studies in order for a numerically obtained solution to be established as physically relevant, the new experience gained during this part of the work is that low-resolution simulations may produce results which can be erroneously interpreted as being related to the known from experiment physical behaviour of the open cavity solution. In view of the different resolution capacity of spectral methods on one hand and finite-difference or finite-volume schemes on the other, the present observations may be relevant to simulations using the latter numerical methods and resolutions substantially higher than those presently employed. Caution is warranted in order to discern between physical behaviour and numerical artifacts in open cavity flow simulations.

Increasing the Reynolds number further to Re = 7000 we were unable to obtain a converged steady-state solution when employing up to 32^2 collocation points in each subdomain, as shown in Figure 27. The iteration history signal appears to be nonlinear throughout the simulation. One of the iterates of the solution shortly before numerical instability destroys the simulation is shown in Figure 28. The results for the streamfunction and its derivatives seem plausible, although one notices the large extent of interaction between fluid outside and inside the cavity, as well as the strong gradient forming in the neighbourhood of the downstream corner of the cavity; the latter is an indication that further runs to must be performed at higher resolutions. Although it would be tempting to proclaim that we have identified the critical Reynolds number for amplification of two-dimensional ($\beta = 0$) global linear instabilities (Theofilis 1999) the results at Re = 6000 warrant caution and such a statement may only be made after simulations at higher resolutions (and associated smaller values of ω, i.e. simulations which are altogether substantially more expensive than the one using 32^2 collocation points in each subdomain) have been performed. This forms one of the possible extensions of the present work, namely the identification through extensive grid-refinement study of the critical Reynolds number $\mathrm{Re}_{cr,2D}$ for amplification of two-dimensional global linear instabilities. A further avenue which may be pursued in continuation of the present work is simulations of time-periodic states which are expected to set in past $\mathrm{Re}_{cr,2D}$ as a consequence of neutrally-stable ($\beta = 0$) global linear eigenmodes which interact nonlinearly with the steady laminar basic state. The objective of pursuing simulations at higher Reynolds numbers is to broaden the scope of the present work towards Reynolds numbers relevant to Air Force needs. Subsequent global linear instability analyses of both steady and time-periodic states will identify two *different* mechanisms *both* of which are of relevance to high-speed flow. From a technical point of view, the extension of the present work into recovery of time-periodic basic states may be pursued using a straightforward time-accurate extension of the algorithms validated herein.

(ii) Rectangular cavity solutions

Next, we have turned our attention to open cavities in which $L \neq D$. We have considered a constant free-stream velocity $\bar{u} = 1$ and kept the locations of the inflow domain and the upstream lip of the cavity at the fixed positions $x_{in} = 0.5$ and $x_{in} + x_L = 0.5 + 20\delta^*$, respectively, where δ^* is the flat-plate boundary layer thickness at inflow; the outflow boundary is placed at $50\delta^*$ past the downstream vertical wall of the cavity. Taking as reference the square cavity solution $L = D = 10\delta^*$ wide cavity solutions have been obtained by taking $D = 10\delta^*$ and $L/D = 2(1)10$ while deep cavity solutions have been obtained using $L = 10\delta^*$ and $D/L = 2, 3$ and 4. In all simulations space was discretised using the same conformable subdomains as in the square cavity simulations, in which 20 collocation points resolved each spatial direction. An $\omega = 0.1$ has sufficed for converged solutions to be obtained after a few hundreds of iterations at all parameters.

Figure 29 shows the dependence of the maximum of the streamwise velocity component along the interface of the domains II and IV. This quantity reaches its minimum in the square cavity and depends in a nearly linear manner on the aspect ratio L/D as the latter increases. The physical explanation of this result is rather straightforward, pointing to the fact that increasingly more fluid from the free stream entrains into the cavity as L/D increases. This may be appreciated in the results of Figures 30-33, where the solutions for ψ, u, v and ζ at $L/D = 3(2)9$ are plotted. Our intention here is to highlight the qualitative features of the solutions obtained and hence we present a large number of equally spaced contours between zero and the maxima of each quantity as well as the same number of contours between the minima and zero of the respective quantities. The same results are plotted in Figure 34 on the same scale, so that the quantitative changes resulting from a change of the aspect ratio may be appreciated. At about $L/D = 5$ the single recirculation region inside the open cavity is divided in two large areas of recirculating flow attached to either of the upstream and downstream vertical cavity walls; as the aspect ratio of the cavity increases further the flow pattern in the neighbourhood of the upstream and downstream vertical walls of the open cavity increasingly resembles that of the union of two other interesting prototype flows, namely the backward- and forward-facing step flow. The latter may be better visualised in Figure 35 in which isolines of the steady laminar solution at $L/D = 10$ are presented. In order for the recirculation regions to be highlighted ten isolines of positive values between zero and the respective maxima as well as ten isolines of negative values between the respective minima and zero and the associated colourbars were generated for the respective flow quantities. At these parameters the attached laminar flow at the inflow boundary separates past the upstream lip of the cavity and reattaches at the lower wall of the cavity at $x \approx x_{in} + x_L + 1.25D$ before separating again shortly before the downstream vertical wall of the cavity is reached. Thereafter a laminar attached boundary layer develops up to the outflow boundary. Comparisons of the results obtained with established backward- and forward-facing step benchmark simulations is beyond the scope of the present investigation and will be reported separately in due course as yet another possible extension of the present work. From a numerical point of view, in line with the results of the Poisson equation obtained in § 3 (c), it suffices here to state that the present wide cavity steady-state results demonstrate that the spectral multidomain algorithm presented herein is capable of solving for flow in both the backward and the forward-facing step geometry in a straightforward manner.

Finally, we turn our attention to deep cavities and present in Figures 36-39 and 40, respectively, the qualitative and quantitative features of steady ψ, u, v and ζ solutions obtained at $D/L = 1(1)4$. These may be discussed along both numerical and physical lines. From a numerical point of view, as in all open cavity solutions obtained so far, we have not noticed any evidence of numerically introduced discontinuity of the solution at subdomain interfaces. Briley's outflow boundary conditions neither introduce artificial boundary layers in the neighbourhood of the outflow boundary nor do they affect the flowfield in the neighbourhood of the cavity. A comment

relevant to the wide cavity simulations also is that the quality of the solution is not affected in the context of the present spectral simulations when the aspect ratio of the minimal discrete cell increases. This is a problem which is of concern to finite-difference and finite-volume simulations, where the ratio of the minimal discretised lengths in the two spatial directions must be of $O(1)$. Here this aspect ratio is shown to take values from 0.25 to 10 inside the cavity without any visible influence on the quality of the solution. Furthermore, the pattern predicted by Burggraf (1966) on the basis of the lid-driven cavity, including its symmetries, is also present in our deep open-cavity numerical results; note that 11 orders of magnitude separate the maximum and the minimum values at which isolines of ζ in the deepest cavity are drawn in Figures 36-39 and 40. From a physical point of view we observe in the open cavity the formation of multiple recirculation zones of essentially Stokes flow (known as Moffat eddies) as the depth of the cavity increases. The strength of recirculation decreases exponentially as one progresses from $y = 0$ to $y = -|D|$ with most of the activity taking place in the neighbourhood of the interface between the cavity and the outer flow. From the point of view of a subsequent global linear instability analysis, owing to their small magnitude in comparison with the flow in the neighbourhood of the cavity lips, the details of the Moffat eddies are not expected to influence the accuracy of the instability results to be obtained. Nevertheless, it is remarkable that a resolution of the flow with 20 collocation points per spatial direction inside the cavity is capable of delivering this result. If finer resolution of the Moffat eddies is required, this may be straightforward obtained by refining the cavity resolution by subdividing it in additional subdomains, as indicated in Figure 3. While it is certainly possible to pursue higher resolution simulations, we bear in mind the ultimate objective of the present work, which is recovery of as accurate as possible a basic flow on as small number as possible a number of discretisation points. The proposed spectral multidomain algorithm has been shown to satisfy this requirement.

(iii) SOLUTIONS IN A FULL BAY MODEL

Beyond delivering accurate results at modest resolutions, the multidomain algorithm proposed for the solution of the open cavity problem is well-suited to solve this problem beyond the idealised situation of an empty rectangular open cavity. As an aside to the main theme of the present report, we discuss the solution to a problem representative of the class of flows indicated in § 2 (a) in which an object is contained in the open cavity. A two-dimensional model of the domain of a full bay is shown in Figure 41. This domain is chosen as a demonstrator of the capabilities of the present spectral multidomain algorithm, without any pretension to model a specific cargo; it should be clear, though, that the limit of complexity of the geometry which may be tackled using our approach is set by efficiency aspects and the number of processors available to be devoted to the (clearly parallelisable) solution approach. All solutions which follow were obtained on a single-processor platform using the 24 subdomains indicated in Figure 41.

From an algorithmic point of view, there is no conceptual addition in complexity by considering the domain shown in Figure 41. The nature of the boundary conditions necessary to close the problem in each subdomain is the same as that in the empty open cavity, namely an inflow boundary, a solid wall and a free-stream or outflow boundary. The compatibility conditions across domain interfaces are treated as part of the new iterative algorithm used for the open cavity solutions presented in the previous sections. The efficiency of our approach is indicated by the fact that solutions on $8 \times 8, 12 \times 12, 16 \times 16$ or 20×20 conformable grids in each subdomain could be obtained on single-processor platforms within reasonable computing times. A technical detail of interest is that if the number of discretisation points is kept the same in all subdomains which discretise space in this relatively complex geometry, the smallest grid spacing in the smallest in size subdomain imposes an unnecessarily small iteration parameter ω (or time-step in a time-accurate framework) if standard Chebyshev Gauss-Lobatto (CGL) grids are used. Indeed, the value of ω scales with $1/N^4$, where N is the number of CGL points used in each spatial

direction; this limitation severely restricts the usefulness of a spectral method as resolution increases. A remedy is to redistribute the CGL points in a more equidistant manner compared with the (strongly stretched at the endpoints of the integration domain) CGL grid. There are several ways to achieve this target; here we have constructed a straightforward modification of the grid proposed by Kosloff and Tal-Ezer (1993). Specifically, we map the CGL points $\xi = \cos \frac{j\pi}{N}, j = 0, \cdots, N$ onto

$$\eta = x_L + \frac{x_R - x_L}{2} \left\{ \frac{\arcsin[(\beta - 1)\xi]}{\arcsin(1 - \beta)} + 1 \right\}, \tag{4.6}$$

where x_L and x_R are the endpoints of the original domain, mapped on themselves. Appropriate choices of the $O(N^{-2})$ parameter β alleviate the $1/N^4$ restriction for ω to $1/N$; using $\omega = 10^{-3}$ we have obtained converged results within $O(10^4)$ iterations in what follows. The convergence history of a typical solution obtained with 8 collocation points per spatial direction and subdomain is shown in Figure 42. The large number of iterations shown is characteristic of the complexity of the problem solved. While the discrepancy between successive iterates becomes lower than 0.02% after $\sim 3 \times 10^4$ iterations, the solution relaxes to the converged result rather slowly. We attribute this finding to the relatively large fraction of subdomain boundaries on which an iteration is required over those on which physical boundary conditions are supplied. This fraction increases from 0.3 in the case of the subdomain discretisation used for the empty open cavity shown in Figure 2 (upper) to 0.8 in the spatial discretisation of Figure 41.

From a physical point of view, the objective of this short departure from the main theme of our report has been to compare solutions in the open (empty) and the present model of a full-bay cavity. To this end, we chose the parameters shown in Table 7 which result in solutions to be compared (in the sense of size of the domain) with the $L/D = 5$ rectangular cavity results also presented in Figure 34. The streamfunction and its first derivatives are shown in Figures 43-45 along the results of the equivalent-sized empty open cavity. In all results an equidistant number of contours between the respective maxima/minima and zero are provided. As expected, substantial differences in the solutions in the two configurations exist; the presence of a sizable object inside the cavity leads to the destruction of the zero-streamline which connects the upstream and downstream lips of the empty cavity and to the formation of strong shear layers inside the cavity, with new stagnation points being formed as a consequence of the chosen geometry. The extent to which fluid from the free-stream entrains into the open cavity may be seen in Figure 43 where the regions of recirculating fluid under the object have been highlighted.

The qualitative features of the results presented in Figures 43-45 have been found to be independent of resolution when using between 8 and 20 points per spatial direction and subdomain. Clearly, running the code on a parallel machine can refine the quantitative features of the solutions obtained; this is also beyond the scope of the present work. What we are interested in here is viewing these results within the framework of a global linear instability analysis. The conclusion which may be drawn is that the total resolution requirements take a global linear analysis of the full-bay basic flow model well beyond the reach of an eigenvalue problem approach. While it might still be possible to obtain reasonably well resolved global linear instability results in the empty open cavity using an eigenvalue problem approach in which the spatial discretisation is treated in a coupled manner, a time-accurate approach and decoupled calculation of spatial derivatives is essential for the global linear instability analysis of a full-bay model. The well-validated spectral multidomain algorithm proposed herein is one efficient potential candidate to be employed in this respect.

V. Theofilis

5. The compressible equations of motion in two spatial dimensions

(a) *Governing Equations*

We now turn our attention to the compressible equations of motion. In conservative formulation and two Cartesian spatial dimensions the nondimensional equations read

$$\frac{\partial \mathbf{Q}}{\partial t} + \frac{\partial \mathbf{F}_c}{\partial x} + \frac{\partial \mathbf{G}_c}{\partial y} = \frac{1}{\text{Re}} \left(\frac{\partial \mathbf{F}_v}{\partial x} + \frac{\partial \mathbf{G}_v}{\partial y} \right), \qquad (5.1)$$

where

$$\mathbf{Q} = \begin{bmatrix} \rho \\ \rho u \\ \rho v \\ E \end{bmatrix},$$

is the solution vector,

$$\mathbf{F}_c = \begin{bmatrix} \rho u \\ \rho u^2 + p \\ \rho uv \\ u(E+p) \end{bmatrix}, \ \mathbf{G}_c = \begin{bmatrix} \rho v \\ \rho uv \\ \rho v^2 + p \\ v(E+p) \end{bmatrix},$$

are the convective and

$$\mathbf{F}_v = \begin{bmatrix} 0 \\ \tau_{xx} \\ \tau_{yx} \\ u\tau_{xx} + v\tau_{yx} + q_x \end{bmatrix}, \ \mathbf{G}_v = \begin{bmatrix} 0 \\ \tau_{xy} \\ \tau_{yy} \\ u\tau_{xy} + v\tau_{yy} + q_y \end{bmatrix}.$$

are the viscous fluxes, respectively.

The total energy E is related with density ρ, temperature T and the Cartesian velocity components u and v in the x and y spatial directions, respectively, through

$$E = \frac{1}{\gamma - 1}p + \frac{1}{2}\rho(u^2 + v^2)$$

and an ideal gas law is assumed, for which

$$p = \frac{1}{\gamma M^2}\rho T.$$

The fluid is taken to be Newtonian, with the viscous stress tensor components given by

$$\tau_{xx} = 2\mu\frac{\partial u}{\partial x} + \lambda\left(\frac{\partial u}{\partial x} + \frac{\partial v}{\partial y}\right), \tau_{yy} = 2\mu\frac{\partial v}{\partial y} + \lambda\left(\frac{\partial u}{\partial x} + \frac{\partial v}{\partial y}\right), \tau_{xy} = \tau_{yx} = \mu\left(\frac{\partial u}{\partial y} + \frac{\partial v}{\partial x}\right).$$

while the components of the heat-flux vector are

$$q_x = \frac{\mu}{(\gamma - 1)M_\infty^2 \text{Pr}}\frac{\partial T}{\partial x}, \ q_y = \frac{\mu}{(\gamma - 1)M_\infty^2 \text{Pr}}\frac{\partial T}{\partial y},$$

The ratio of the heat capacities of the fluid under constant pressure c_p and constant volume c_v is denoted by γ; an $O(1)$ reference length L and free-stream reference quantities, namely

$\rho_0, u_0, p_0 = \rho_0 u_0^2, T_0 = u_0^2/c_v$, have been used for the nondimensionalisation of the equations; these have been combined into the Reynolds $\mathrm{Re} = \rho_0 u_0 L/\mu_0$ and Prandtl $\mathrm{Pr} = \mu_0 c_p/k_0$ numbers of the flow with the latter taken to assume the constant value for air, $\mathrm{Pr} = 0.72$.

Stokes' hypothesis

$$\lambda = -\frac{2}{3}\mu \tag{5.2}$$

and Sutherland's law for viscosity

$$\mu = T^{3/2}\frac{1 + \mathrm{C}_S}{T + \mathrm{C}_S}, \tag{5.3}$$

with $\mathrm{C}_S = 110.4^\circ\mathrm{K}/T_0$ complete the system of equations to be solved in the framework of compressible direct numerical simulations.

(b) *Inflow boundary conditions*

In a manner analogous to the incompressible simulations presented in § 4 at the inflow boundary in the DNS the similarity profiles pertaining to compressible boundary-layer flow over a flat plate at given free-stream Reynolds and Mach numbers is imposed. The similarity solution is obtained using the classic Howarth-Dorodnitsyn transformation of the compressible laminar boundary layer equations which transforms the wall-normal coordinate y into a similarity coordinate η defined by

$$y = \sqrt{\frac{2\xi}{\mathrm{Re}}}\int_0^\eta T(\tau)d\tau, \tag{5.4}$$

where

$$\eta = \frac{\sigma}{\sqrt{2\xi\mathrm{Re}}} \text{ and } \sigma = \int_0^y \rho(\tau)d\tau. \tag{5.5}$$

The system of ordinary differential equations to be solved for the determination of the streamwise velocity component u and temperature T is

$$\left(\chi f''\right)' + ff'' = 0, \tag{5.6}$$

$$\left(\frac{\chi}{\mathrm{Pr}}T'\right)' + fT' + (\gamma - 1)M_\infty^2\chi\left(f''\right)^2 = 0, \tag{5.7}$$

where $f' = u/u_\infty, \chi = (\rho\mu)/(\rho_\infty\mu_\infty)$ and primes denote differentiation with respect to the similarity variable η. The system (5.6-5.7) is solved subject to the boundary conditions

$$f(0) = 0, \ f'(0) = 0, \ f'(\eta \to \infty) = 0, \tag{5.8}$$

$$T(\eta \to \infty) = 1, \tag{5.9}$$

alongside

$$T(0) = T_w/T_\infty \tag{5.10}$$

in the case of an isothermal wall, or

$$T'(0) = 0 \qquad\qquad\qquad (5.11)$$

if an adiabatic wall is considered. Details of the shooting algorithm used and solutions of the compressible flat-plate boundary layer obtained are outlined in the Appendix.

Solutions of the compressible flat-plate boundary layer equations have been obtained using $\mathrm{Pr} = 0.72, T_0 = 288.89^\circ\mathrm{K}$ and $M_\infty = 0.01, 0.5, 1.0$ and 1.5. Plots of the streamwise velocity component u, temperature T and their first two derivatives are shown in Figure 46. Both the viscous and the thermal boundary layers in the subsonic cases are barely distinguishable from the incompressible result. As a consequence, a (non-rational) global linear instability analysis performed on the basis of the incompressible model at subsonic Mach numbers and the consistent compressible global linear instability approach are expected to deliver qualitatively analogous results. Of interest is whether the presence of inflectional profiles in the compressible basic state at inflow introduces additional (global) linear instability modes, as the case is in the classic linear analyses. This forms one of the questions to be answered in future.

(c) Numerical Methods

After discretising the open cavity domain in the manner presented in §1, we employ in each subdomain a twofold extension of the techniques discussed by Theofilis (1998b) for the solution of the two-dimensional compressible Euler equations. Firstly, in the present problem two inhomogeneous spatial directions are considered, as opposed to the one inhomogeneous and one periodic spatial direction of the latter work. Secondly, the algorithm is straightforwardly extended to incorporate calculation of the viscous fluxes in the form presented above. Spatial derivatives are calculated using the same collocation algorithm discussed for the incompressible simulations. Alternative schemes based on compact finite-difference methods, which have reached a high level of sophistication (Visbal and Gaitonde 1998; Gaitonde and Visbal 1999), might also have been used; however, the issue of performance of the numerical scheme for the calculation of spatial derivatives was found to be highly platform-dependent (Theofilis 1998b) and, hence, we adhere to the spectral scheme which provides optimal accuracy at modest resolutions.

By contrast to the incompressible simulations, here we concentrate on obtaining time-accurate compressible results using a low-storage fully explicit algorithm due to Wray (1986) for the time-integration of the equations of motion. The algorithm advances the solution vector $\mathbf{Q}$ according to

$$\begin{aligned}
\mathbf{k}_1 &= \Delta t \quad \mathbf{F}(\mathbf{Q}^n, t_n) \\
\mathbf{k}_2 &= \Delta t \quad \mathbf{F}(\mathbf{Q}^n + \frac{2}{3}\mathbf{k}_1, t_n + \frac{2}{3}\Delta t) \\
\mathbf{k}_3 &= \Delta t \quad \mathbf{F}(\mathbf{Q}^n + \frac{1}{4}\mathbf{k}_1 + \frac{5}{12}\mathbf{k}_2, t_n + \frac{2}{3}\Delta t)
\end{aligned}$$

$$\mathbf{Q}^{n+1} = \mathbf{Q}^n + \frac{1}{4}\mathbf{k}_1 + \frac{3}{20}\mathbf{k}_2 + \frac{3}{5}\mathbf{k}_3, \qquad\qquad (5.12)$$

where superscript (n) indicates time-level, Δt is the time-step and $\mathbf{F} = -\mathbf{F}_c - \mathbf{G}_c + 1/\mathrm{Re}\mathbf{F}_v + 1/\mathrm{Re}\mathbf{G}_v$, as defined in (5.1). The attractive feature of the particular RK3 scheme is that it provides third-order accuracy in time, while it requires only two levels of storage. As such the RK3 represents a compromise between the more accurate but more expensive classic RK4 and the less accurate and equally expensive second-order accurate RK2 scheme. The severe time-step restrictions of explicit schemes in conjuction with spectral spatial discretisation are alleviated by

use of the mapping proposed by Kosloff and Tal-Ezer (1993) discussed in § 4 (d). Appropriate choice of the single mapping parameter results in near-uniform distribution of collocation points in the two spatial directions, which in turn permits time-steps of $O(1/N)$, N denoting the total number of collocation points in either the $x-$ or the $y-$direction, as opposed to $O(1/N^4)$ by which standard Chebyshev methods are restricted (Canuto *et al.* 1987).

A straightforward Dirichlet-Neumann algorithm has been constructed to ensure C^1-continuity of the solution at an interface Γ of two subdomains Ω_1 and Ω_2, according to which a solution $\mathbf{Q}_1$ of (5.1) is obtained in Ω_1 which satisfies an arbitrary Dirichlet boundary condition and provides Neumann data for the solution $\mathbf{Q}_2$ of the governing equations in Ω_2. The algorithm is

$$\begin{cases} \frac{\partial \mathbf{Q}_1}{\partial t} = -\frac{\partial \mathbf{F}_1}{\partial x} - \frac{\partial \mathbf{G}_1}{\partial y} & \text{in } \Omega_1, \\ \mathbf{Q}_1^{(m)} = \underline{\lambda}^{(m-1)} & \text{on } \Gamma, \\ \\ \frac{\partial \mathbf{Q}_2}{\partial t} = -\frac{\partial \mathbf{F}_2}{\partial x} - \frac{\partial \mathbf{G}_2}{\partial y} & \text{in } \Omega_2, \\ \partial \mathbf{Q}_1^{(m)}/\partial n_\Gamma = \partial \mathbf{Q}_2^{(m)}/\partial n_\Gamma & \text{on } \Gamma, \end{cases} \tag{5.13}$$

where $\mathbf{F} = \mathbf{F}_c - \frac{1}{\text{Re}}\mathbf{F}_v$ and $\mathbf{G} = \mathbf{G}_c - \frac{1}{\text{Re}}\mathbf{G}_v$. The vector of Dirichlet data on the interface is updated according to

$$\underline{\lambda}^{(m)} = \omega \mathbf{Q}_2^{(m)} + (1-\omega)\underline{\lambda}^{(m-1)}, \tag{5.14}$$

with superscript (m) indicating iteration level and ω being an $O(1)$ relaxation parameter. Note that the iteration produces C^1-continuous values of the *conservative* quantities at each new time-level, from which the primitive variables may be extracted.

(d) *Boundary conditions for aeroacoustics calculations*

The objective currently is calculation of steady-state solutions in an open cavity in compressible flow. Aside from the issue of accuracy, which may be guaranteed by ensuring sufficiently high resolution, a novelty introduced by compressibility is the finite speed of propagation of pressure waves and the potential of confusion between acoustic signals generated by the flow itself and numerically generated reflections at the boundaries of the calculation domains. This issue is clearly demonstrated by the problem of advection of a vortical disturbance (Visbal and Gaitonde 1998)

$$\rho = 1, \tag{5.15}$$

$$u = U_\infty - \frac{C}{R^2}(y - y_c)\exp\left(-r^2/2\right), \tag{5.16}$$

$$v = \frac{C}{R^2}(x - x_c)\exp\left(-r^2/2\right), \tag{5.17}$$

$$p = p_\infty - \frac{\rho C^2}{2R^2}\exp\left(-r^2\right), \tag{5.18}$$

where (x_c, y_c) is the location around which vorticity is distributed initially, U_∞ is the advection velocity, p_∞ is the ambient pressure, $r^2 = (x-x_c)^2/R^2 + (y-y_c)^2/R^2$ and C and R are constants. Two sets of results were obtained using the compressible DNS techniques discussed; the results serve to illustrate the point regarding numerical reflections at finite boundaries. All simulations were performed in single domains using upwards of 50 collocation points per spatial direction and time-steps of $O(10^{-2})$.

Firstly, we have chosen $(x_c, y_c) = (0, 0), U_\infty = 0, C = 1, R = 1$ and performed several simulations initialised by (5.15) and (5.18) alone, setting $u = v = 0$ initially; the transient solution quickly settles to u and v predicted by (5.16-5.17) as seen in Figure 47, independently of Reynolds or Mach number values. While no distortions are to be seen on account of numerical dissipation, which is practically absent in the spectral scheme used, these transient solutions are destroyed by numerical instability as time in the simulation progresses; identification of the origin of this numerical instability is our next concern. To this end we set $(x_c, y_c) = (-5, 0), U_\infty = 1, C = 0.1, R = 0.75$ and perform simulations at $M = 0.4, 0.8$ and $M = 1.2$ at $Re = 10^5$, initialising the calculation using (5.15-5.18). The results at the highest Mach number are presented in Figures 48 and 49. If attention is focussed on the velocity components alone (or vorticity, not presented here), one sees that the vortical structure is being advected by the flow at the imposed speed U_∞ throughout the simulation. This result is repeated at all Mach numbers examined, the difference being that when all parameters in the respective simulations are kept identical as the Mach number decreases numerical instability sets in earlier in time. The same conclusion is to be drawn from the results of Figure 50 where the passage of the vortex is recorded at two fixed locations $(x = x_0, y = 0)$ with $x_0 = 0$ and $x_0 \approx 10$, respectively. Starting at $x_c = -5$ the vortex passes from these locations with no distortion, as seen clearly in the v−signal which is indistinguishable from the analytical solution at all times examined.

However, the reason for the numerical instability is clearly to be seen in the signals of ρ, u and v as well as in the density and pressure isosurfaces presented in Figures 48 and 49. A cylindrical pressure wave emanating from the vortical structure propagates in space, reflects on the boundary and returns to the integration domain. The reason is clearly the boundary conditions imposed at the artificially truncated boundaries, the reflecting character of which is responsible for the numerical instability initially and the destruction of the simulation eventually. One remedy is to place the boundaries far enough from the region of interest; however, this approach is not suitable for simulations in the open cavity, where long-time integrations will be necessary for a steady state solution to be obtained. A more elegant solution to this problem is the imposition of non-reflecting boundary conditions based on characteristic analyses (Thompson 1987; Poinsot and Lele 1992). While the issue of non-reflecting boundary conditions is the subject of current investigations (Rowley and Colonius 2000) it should be noted that in subsonic simulations some amount of reflection must be allowed in order for pressure to be able to adjust to the ambient value and implementation of perfectly non-reflecting boundary conditions is not advisable. Our current objective is the study of non-reflecting far-field boundary conditions in conjunction with spectral multidomain algorithms. Specifically, we are interested in the interaction of pressure waves with artificially created internal boundaries, such as the interfaces of the multidomain algorithm, and the potential generation of instabilities of numerical origin at such boundaries. Once this issue has been answered in a satisfactory manner we intend to proceed and obtain the compressible analoga of the open cavity solutions presented in § 4 (d); results will be presented in due course.

6. Conclusions

A spectral multidomain algorithm of the Dirichlet-Neumann class has been presented for the numerical solution of the Poisson equation and of the streamfunction/vorticity-transport formulation of the system of equations governing incompressible fluid flow, when space is decomposable in rectangular subdomains. The novelty of the algorithm is that, in the case solutions to the steady equations of motion are sought, the iteration necessary for satisfaction of solution continuity across subdomain interfaces and that for the nonlinearity of the governing partial differential equations are combined and performed in a single step. This results in order-of-magnitude savings compared with the standard approach in which these iterations are nested within each other. The issue of physical boundary conditions and numerical compatibility conditions has been discussed by reference to several benchmark solutions with which excellent agreement has been obtained. In geometries in which single-domain calculations may also be used it has been observed that higher resolution is necessary when using multidomain in order to achieve results of the same quality as those of the single-domain calculation. Relatively high resolutions are necessary for the solution of both the Poisson and the incompressible Navier-Stokes and continuity equations when the domain contains geometric singularities, as the case is in the open cavity. Particularly revealing are the solutions of the Poisson equation in such domains, where estimates of the number of collocation points necessary in each subdomain in order for solutions to converge within prescribed tolerances may be obtained. This is especially helpful in the context of the global linear instability analyses, which form the objective of an extension of the present work, since the ability to increase the resolution of the steady laminar basic flow at will is absent in the framework of the instability analyses.

Steady laminar incompressible solutions for low Reynolds number flow in arbitrary aspect-ratio open cavities have been obtained. The deep cavity limit at the Reynolds numbers examined was found to bear remarkable analogies with the well-known patterns of the lid-driven cavity flow (Burggraf 1966). Wide open cavity solutions, on the other hand, were found to correspond to the union of the well-known flow patterns in the backward- and forward-facing step geometries. The high resolution requirements suggested by the model problems examined earlier were confirmed in the open cavity simulations. One of the most interesting findings of the present work is the resonance-like behaviour of the flow at modest spatial resolutions. A clearly defined periodic solution pattern, which may well be confused with flow resonance between the upstream and the downstream vertical cavity walls, appeared as a consequence of modest resolutions and disappeared when resolution was increased further. The need for careful further numerical experimentation in order for the critical Reynolds number $Re_{2d,st}$ for onset of two-dimensional unsteadiness has thus been underlined. A further interesting result of the present work is the assessment of the differences of the flowfield set up in the empty as opposed to an open cavity containing an object. From the point of view of a subsequent global linear instability analysis, the resolution requirements in latter flow were found to be such that the instability analysis may only be performed in the context of an initial-boundary value problem. The resolution requirements of the empty open cavity, on the other hand, are such that a partial-derivative linear eigenvalue problem approach (Theofilis 1998a) may be employed.

In order for compressible flow solutions in the open cavity to be obtained the issue of appropriate boundary and compatibility conditions must be addressed. The problem at the inflow boundary was solved by provision of the compressible flat-plate boundary-layer solution, while the potential pitfalls of naive application of the incompressible boundary conditions to the solution of the boundary closure problem in the far-field and the downstream outflow boundaries of the computational domain in compressible simulations have been highlighted. It was shown that boundary conditions which do not prevent reflections at artificially introduced boundaries may not necessarily destroy the simulation but can definitely lead to misinterpretation of its results. We are currently working on this issue.

Our recent work on residuals in DNS, motivated by our desire to understand the origins of instability and three-dimensionalisation of two-dimensional steady flows, such as those in the open cavity, suggests that the existence of two-dimensional steady-state solutions in the open cavity is synonymous with stability of all two-dimensional global flow eigenmodes. This does not prevent three-dimensional modes being unstable. The extent to which the conclusions put forward in § 4 (d) carry weight in a three-dimensional environment will precisely be determined by the global instability analysis in which the entire steady $(x, y)-$flowfields calculated in the framework of the present work may be used as variable coefficients for the partial-differential-equation-based complex nonsymmetric generalised eigenvalue problem. Estimates, based on the known global linear instability results in the lid-driven cavity, of the instability results in the open cavity may already be obtained indirectly by comparing the open and the lid-driven cavity basic states; this work is also in progress.

The global linear instability analysis of the open cavity flow forms the ultimate objective of an extension of the present work; an intermediate step is the extension of the incompressible part of the present work to implement a time-accurate approach for the recovery of open-cavity solutions, an approach which is expected to be an order of magnitude more intensive computationally compared with the iterative algorithm proposed herein, on account of the iterations for satisfaction of solution continuity across subdomains being nested within the fractional time-steps of the time-integration procedure; however, the time-accurate algorithm is necessary in order for two-dimensional laminar time-periodic basic states to be obtained. Both incompressible and compressible *time-periodic* fields may form an alternative basic flow compared with the laminar steady-states obtained herein. Qualitatively different basic flows and a global linear instability analysis approach incorporating Floquet theory in the case of a time-periodic basic state are expected to result in the identification of *different types* of global linear instability mechanisms. The deliverable of this approach will be a critical Reynolds number $Re_{2d,tp} > Re_{2d,st}$ which will be closer to that relevant to Air Force needs in comparison with $Re_{2d,st}$. Clearly, linear amplification of both types of global disturbances, *stationary and time-periodic*, is relevant to flight Reynolds numbers.

Finally, the experience obtained in the present work suggests that the resolution necessary for adequate description of the steady laminar basic flow in the open cavity at high Reynolds numbers or the resolution of the flowfield set up by the presence of sizeable objects within the cavity calls for an extension of the partial-derivative-eigenvalue-problem-based global linear instability approach (Theofilis 1998a). In this respect, one of the present findings points at the fact that a solution approach in which all subdomains are solved in a coupled manner is impractical on account of the large total number of collocation points and the associated memory limitations. One way forward in this respect is implementation of an initial-boundary-value problem approach for global linear instability analysis which incorporates the validated spectral multidomain algorithm discussed in the present work.

Appendix A.
A shooting algorithm for the compressible flat-plate boundary layer equations

Key to the solution of the system (5.6-5.7) is the boundary-layer assumption of a constant pressure impressed upon the flow across the layer,

$$p = \frac{1}{\gamma M_\infty^2}. \tag{A 1}$$

It follows that $\rho T = 1$ and

$$\chi = T^{\frac{1}{2}} \frac{1 + C_S}{T + C_S}, \tag{A 2}$$

where Sutherland's viscosity law (5.3) has been used. Introduction of (A 2) into (5.6-5.7) permits solution of this system for the similarity variables $f(\eta)$ and $T(\eta)$ subject to boundary conditions (5.8-5.9) and either of (5.10) or (5.11). A straightforward shooting approach combined with Newton iteration until all boundary conditions are satisfied is employed to solve the system on a uniform η-grid. The governing equations may be written in the form of as a system of ordinary differential equations

$$\mathbf{h} = \mathbf{g}', \tag{A 3}$$

where

$$
\begin{array}{rclcrcl}
g_1 &=& f & , & h_1 &=& g_2, \\
g_2 &=& f' & , & h_2 &=& g_3, \\
g_3 &=& f'' & , & h_3 &=& -\frac{\chi'}{\chi} g_3 g_5 - \frac{1}{\chi} g_1 g_3, \\
g_4 &=& T & , & h_4 &=& g_5, \\
g_5 &=& T' & , & h_5 &=& -\frac{\chi'}{\chi} g_5^2 - \frac{Pr}{\chi} g_1 g_5 - Pr(\gamma-1) M_\infty^2 g_3^2.
\end{array}
\tag{A 4}
$$

The known boundary conditions are supplemented with estimates of the unknown values $f(\to \infty), f''(0), f''(\to \infty), T'(\to \infty)$ and either of $T(0)$ or $T'(0)$, depending on whether an isothermal or adiabatic problem is considered, respectively. The η-grid encompasses a large number of uniformly-distributed points, such that subsequent interpolations of the similarity results onto the DNS grid may be performed without appreciable error being introduced.

References

C. K. Aidun, N. G. Triantafillopoulos and J. D. Benson 1991
Global stability of a lid-driven cavity with throughflow: Flow visualization studies.
Phys. Fluids A **3**, 2081–091.

J. D. Benson and C. K. Aidun 1992
Transition to unsteady nonperiodic state in a through-flow lid-driven cavity.
Phys. Fluids A **4**, 2316–2319.

O. R. Burggraf 1966
Analytical and numerical studies of the structure of steady separated flows.
J. Fluid Mech., **24**, 113–151.

J. P. Boyd 1989
Fourier and Chebyshev spectral methods. Lecture Series in Engineering, Springer.

K. Black 1997
A spectral element technique with a local spectral basis.
SIAM J. Sci. Comput. **18**, (2) 355–370.

W. R. Briley 1971
A numerical study of laminar separation bubbles using the Navier-Stokes equations.
J. Fluid Mech. **47**, 713–736.

C. Canuto, M. Y. Hussaini, A. Quarteroni, and T. A. Zang 1987
Spectral methods in fluid dynamics. Springer.

P. Demaret and M. O. Deville 1991.
Chebyshev collocation solutions of the Navier-Stokes equations using multi-domain decomposition and finite element preconditioning.
J. Comput. Phys. **95** (2), 359–386.

W. E and J.-G. Liu 1996
Vorticity boundary condition and related issues for finite-difference schemes.
J. Comput. Phys. **124**, 368–382.

D. Gaitonde and M. Visbal 1999
Further development of a Navier-Stokes solution procedure based on higher-order formulas.
AIAA Pap., **99-0557**.

T. B. Gatski and C. E. Grosch 1984
Embedded cavity drag in steady and unsteady flows.
AIAA Paper 84-0436.

R. Kosloff and H. Tal-Ezer 1993
A modified Chebyshev pseudospectral method with an $O(1/N)$ time step restriction.
J. Comp. Physics **104**, 457–469.

A. Patera 1984
A spectral element method for fluid dynamics; laminar flow in a channel expansion.
J. Comp. Physics **54**, 468.

A. Quarteroni 1991
Domain decomposition and parallel processing for the numerical solution of partial differential equations.
Surv. Math. Ind. **1**, 75–118.

T. J. Poinsot and S. K. Lele 1992
Boundary conditions for direct simulations of compressible viscous flows. *J. Comp. Physics* **101**, 104–129.

C. W. Rowley and T. Colonius 2000
Discretely nonreflecting boundary conditions for linear hyperbolic systems.
J. Comp. Physics **157**, 500–538.

U. Rist, U. Maucher, and S. Wagner 1996
Direct numerical simulation of some fundamental problems related to transition in laminar separation bubbles.
Proc. Computational Fluid Dynamics Conf. *ECCOMAS '96*, 319 – 325.

R. Schreiber, and H. B. Keller 1983
Driven cavity flows by efficient numerical techniques.
J. Comput. Phys. **49**, 310–333.

H. Schlichting 1979
Boundary layer theory. Mc-Graw Hill.

S. N. Sinha, A. K. Gupta and M. M. Oberai 1982

Laminar separating flows over backsteps and cavities. Part II: Cavities.
AIAA J. **20** (3), 370–375.

P. R. Spalart 1988
Direct simulation of a turbulent boundary layer up to R_θ=1410.
J. Fluid Mech. **187**, 61–98.

T. Tatsumi and T. Yoshimura 1990
Stability of the laminar flow in a rectangular duct.
J. Fluid Mech. **212**, 437–449.

V. Theofilis 1998a
Linear instability in two spatial dimensions. Proceedings of the Fourth European Computational Fluid Dynamics Conference *ECCOMAS'98*,
K. D. Papailiou (ed.) J. Wiley and Sons, 547–552.

V. Theofilis 1998b
On the resolution of critical flow regions in inviscid linear and nonlinear instability calculations.
J. Eng. Math. **24**, 111–129.

V. Theofilis 1999
On numerical residuals and physical instabilities in incompressible steady-state fluid flow simulations.
DLR IB-223-99 **A 25**, 53pp. Submitted to *J. Comp. Phys.*

V. Theofilis 2000
Globally unstable flows in open cavities. *AIAA Pap.* 2000-1964.

K. W. Thompson 1987
J. Comp. Physics **68**, 1.

W. Tollmien 1929
Über die Entstehung der Turbulenz. 1. Mitteilung,
Nachr. Ges. Wiss. Göttingen Math. Phys. Klasse 21–44.

M. Visbal and D. Gaitonde 1998
High-order accurate methods for unsteady vortical flows on curvilinear meshes.
AIAA Pap., **98-0131**.

A. A. Wray 1986
Very low storage time-advancement schemes.
NASA Ames Int. Rep., 6pp.

Table 1. *Validation of the multidomain algorithm for the Poisson equation in the rectangular duct steady laminar flow; $x(y) \equiv x^y$.*

(Nx, Ny)	iterations	CPU time (sec)	$\psi(x_L,0)$	$\psi_x(x_L,0)$	$A=3$ $\psi(0,0)$	$\psi(x_R,0)$	$\psi_x(x_R,0)$
8×8	8	0.14 (0.07)	0.901343	0.152104	0.981459	0.967024	-0.428399(-1)
16×16	6	2.04 (0.73)	0.901344	0.152106	0.981459	0.967035	-0.428125(-1)
32×32	4	73.21 (4.74)	0.901344	0.152106	0.981459	0.967035	-0.428125(-1)
(Nx, Ny)	iterations	CPU time (sec)	$\psi(x_L,0)$	$\psi_x(x_L,0)$	$A=4$ $\psi(0,0)$	$\psi(x_R,0)$	$\psi_x(x_R,0)$
8×8	8	0.14 (0.07)	0.955314	0.699181(-1)	0.996145	0.990301	-0.140611(-1)
16×16	6	2.04 (0.73)	0.955321	0.699102(-1)	0.996145	0.990328	-0.139337(-1)
32×32	4	73.18 (4.99)	0.955321	0.699102(-1)	0.996145	0.990328	-0.139337(-1)

Table 2. *Validation of the multidomain algorithm for the Poisson equation in the grooved channel.*

	8×8	16×16	32×32	64×64
$\psi(-1, 0.5)$	2.6(-15)	-1.8(-13)	-1.2(-11)	7.0(-12)
$\psi_x(-1, 0.5)$	0.817566	0.816394	0.816215	0.816187
$\psi_y(-1, 0.5)$	7.9(-14)	-3.4(-11)	7.6(-10)	-7.5(-9)
$\psi(-0.75, 0.5)$	0.153385	0.153105	0.153059	0.153052
$\psi_x(-0.75, 0.5)$	0.452766	0.451631	0.451444	0.451413
$\psi_y(-0.75, 0.5)$	-0.028354	-0.027761	-0.027659	-0.027643
$\psi(-0.5, 0.5)$	0.242893	0.242337	0.242249	0.242235
$\psi_x(-0.5, 0.5)$	0.282003	0.281842	0.281784	0.281769
$\psi_y(-0.5, 0.5)$	-0.116120	-0.101810	-0.097664	-0.096486
$\psi(0, 0.5)$	0.317491	0.316856	0.316751	0.316735
$\psi_x(0, 0.5)$	8.9(-6)	8.9(-7)	1.2(-7)	1.9(-8)
$\psi_y(0, 0.5)$	-0.239739	-0.238431	-0.238214	-0.238179
$\psi(0.5, 0.5)$	0.242896	0.242338	0.242249	0.242235
$\psi_x(0.5, 0.5)$	-0.282063	-0.281845	-0.281784	-0.281769
$\psi_y(0.5, 0.5)$	-0.076711	-0.090028	-0.094253	-0.095514
$\psi(0.75, 0.5)$	0.153388	0.153105	0.153059	0.153052
$\psi_x(0.75, 0.5)$	-0.452788	-0.451633	-0.451444	-0.451413
$\psi_y(0.75, 0.5)$	-0.028361	-0.027762	-0.027660	-0.027643
$\psi(1, 0.5)$	0	0	0	0
$\psi_x(1, 0.5)$	-0.817611	-0.816396	-0.816216	-0.816187
$\psi_y(1, 0.5)$	0	0	0	0

V. Theofilis

Table 3. *Validation of the multidomain algorithm for the Poisson equation in the backward-facing step geometry (Black 1997).*

	16×16	32×32	64×64
$\psi(0, 3\pi/4)$	-0.162463	-0.161707	-0.161585
$\psi_x(0, 3\pi/4)$	-0.279086	-0.278571	-0.278505
$\psi_y(0, 3\pi/4)$	-0.222365	-0.234559	-0.237928
$\psi(\pi, 0)$	0.645964	0.645964	0.645964
$\psi_x(\pi, 0)$	1.2(-12)	1.6(-11)	1.5(-10)
$\psi_y(\pi, 0)$	-1.719610	-1.719540	-1.719530

Table 4. *Boundary conditions for single-domain calculations in the PPF. Dirichlet and Neumann data are denoted by* (d) *and* (n) *respectively.*

Boundary	Type	ψ	ζ
N	(d)	Eq. (4.1)	Eq. (2.1)
	(n)	$\psi_y = 0$	
E	(n)	$\psi_{xx} = 0$	$\zeta_{xx} = 0$
S	(d)	Eq. (4.1)	Eq. (2.1)
	(n)	$\psi_y = 0$	
W	(d)	Eq. (4.1)	Eq. (2.1)
	(n)	$\psi_x = 0$	

V. Theofilis

Table 5. *Boundary conditions for multidomain calculations in the square lid-driven cavity. Dirichlet and Neumann data are denoted by* (d) *and* (n) *respectively.*

	Domain 1011			Domain 1110	
Boundary	ψ	ζ	Boundary	ψ	ζ
N	$\psi = 0$ $\psi_y = 1$	Eq. (2.1)	N	$\psi = 0$ $\psi_y = 1$	Eq. (2.1)
E	(d)	Eq. (2.1)	E	$\psi = 0$ $\psi_x = 0$	Eq. (2.1)
S	$\psi = 0$ $\psi_y = 0$	Eq. (2.1)	S	$\psi = 0$ $\psi_y = 0$	Eq. (2.1)
W	$\psi = 0$ $\psi_x = 0$	Eq. (2.1)	W	(n)	Eq. (2.1)

Table 6. *Convergence of open-cavity solutions at different Reynolds numbers*

| Resolution | Re | | | | |
	50	100	500	1000	5000
8×8	0.091626	0.090597	0.079286	0.072195	0.139555
12×12	0.087852	0.087006	0.077489	0.072145	0.146231
16×16	0.085891	0.085086	0.076138	0.071182	0.147909
20×20	0.084899	0.084103	0.075375	0.070629	0.146547

V. Theofilis

Table 7. *Parameters for the solution of the full-bay open cavity model; $(x_0, y_5) = (0.5, 0.121)$ and δ^* is the boundary layer thickness at inflow.*

$$(x_1 - x_0)/\delta^* = 20 \qquad y_4 = 0$$
$$(x_2 - x_1)/\delta^* = 17 \qquad (y_4 - y_3)/\delta^* = 3$$
$$(x_3 - x_2)/\delta^* = 6 \qquad (y_3 - y_2)/\delta^* = 2$$
$$(x_4 - x_3)/\delta^* = 4 \qquad (y_2 - y_1)/\delta^* = 2$$
$$(x_5 - x_4)/\delta^* = 5 \qquad (y_1 - y_0)/\delta^* = 3$$
$$(x_6 - x_5)/\delta^* = 10$$
$$(x_7 - x_6)/\delta^* = 13$$
$$(x_8 - x_7)/\delta^* = 30$$

Table 8. *Convergence of the transient solutions of the inviscid vortical flow at $(x,y) = (0,0)$ and $t = 0.5$; $u, v < 10^{-14}$.*

	$Re = 10^2, M = 1.0$		$Re = 10^5, M = 0.6$		$Re = 10^5, M = 2.6$	
	ρ	E	ρ	E	ρ	E
25×25	0.605211	3.16587	0.633437	5.26767	0.547016	2.40012
50×50	0.614062	3.19235	0.636089	5.28667	0.560949	2.34479
100×100	0.614119	3.19272	0.636078	5.28658	0.561028	2.34295
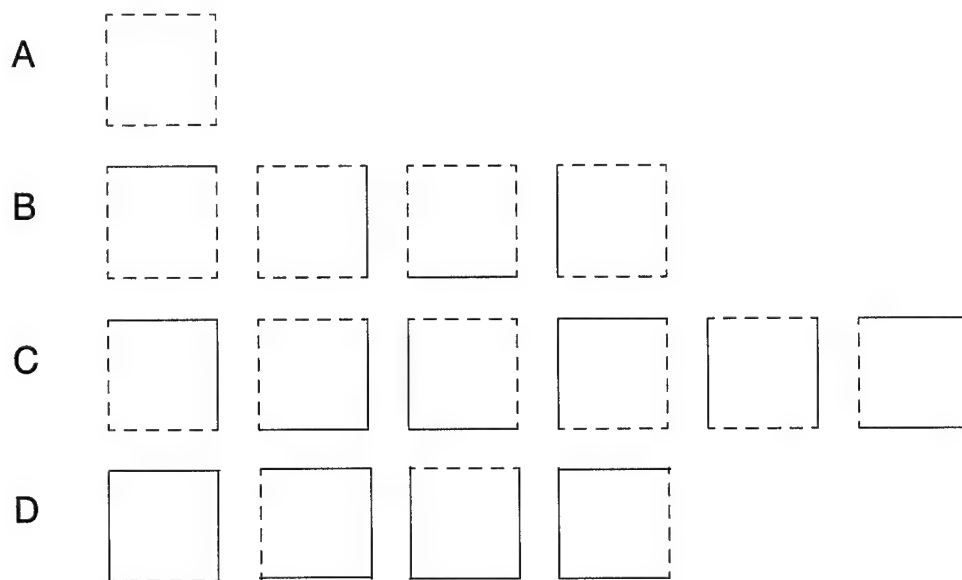
Figure 1. The building blocks of the two-dimensional domains considered
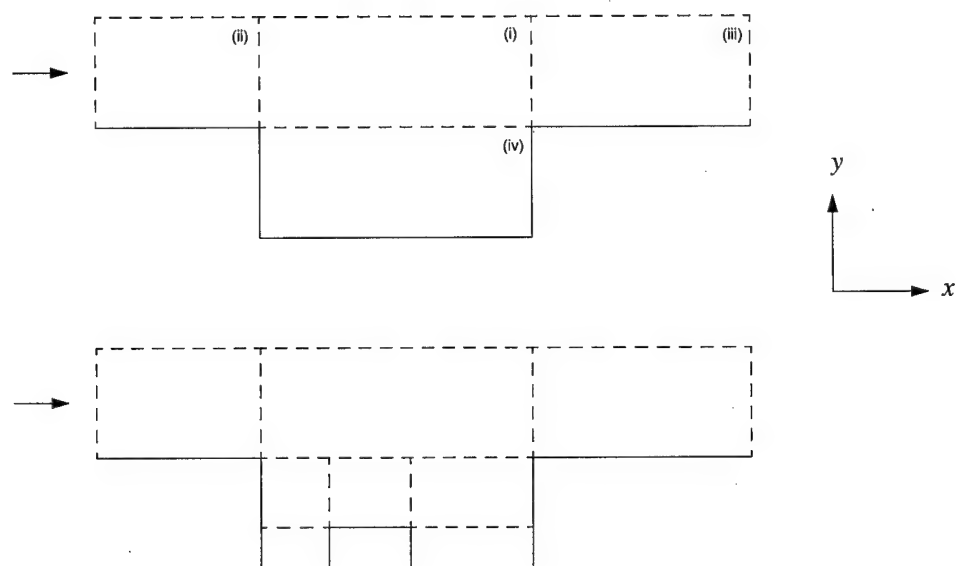
Figure 2. Spatial decomposition of an empty (upper) and an open cavity containing a protrusion (lower) using the building blocks of Figure 1.
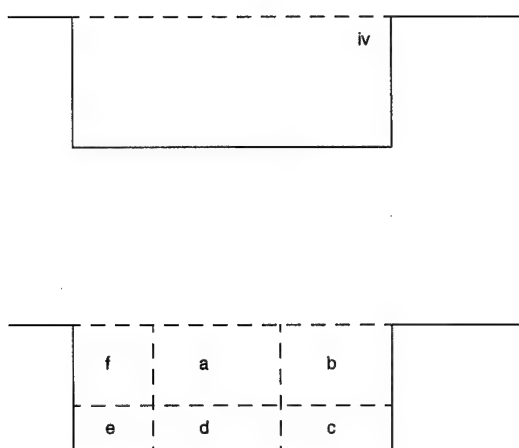
Figure 3. Example of spatial resolution refinement by decomposing an original (upper) into further subdomains (lower).
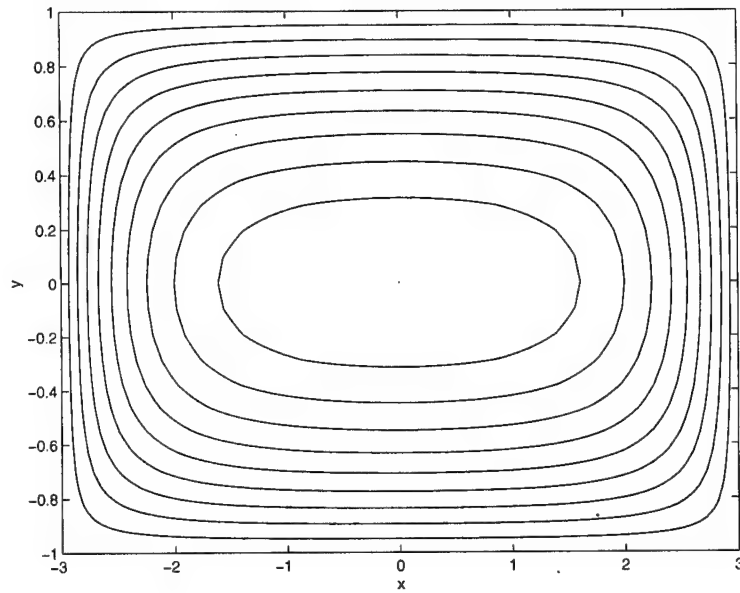
Figure 4. The streamfunction ψ in flow in an aspect-ratio $A = 3$ rectangular duct (Tatsumi & Yoshimura, 1990) recovered using three subdomains with interfaces at $x_L = -0.5A$ and $x_R = 0.25A$.
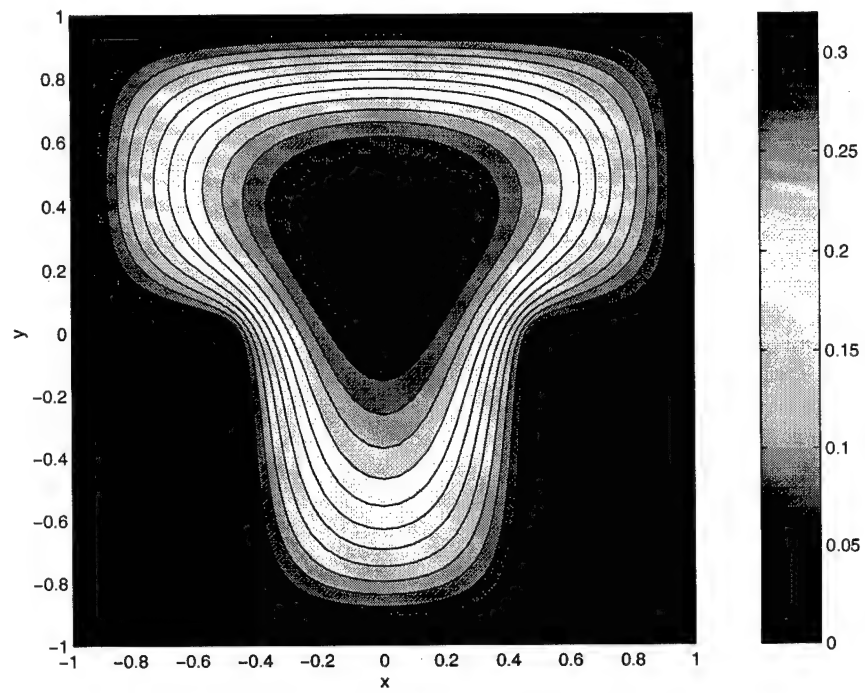
Figure 5. The streamfunction ψ in a grooved channel geometry recovered using five subdomains
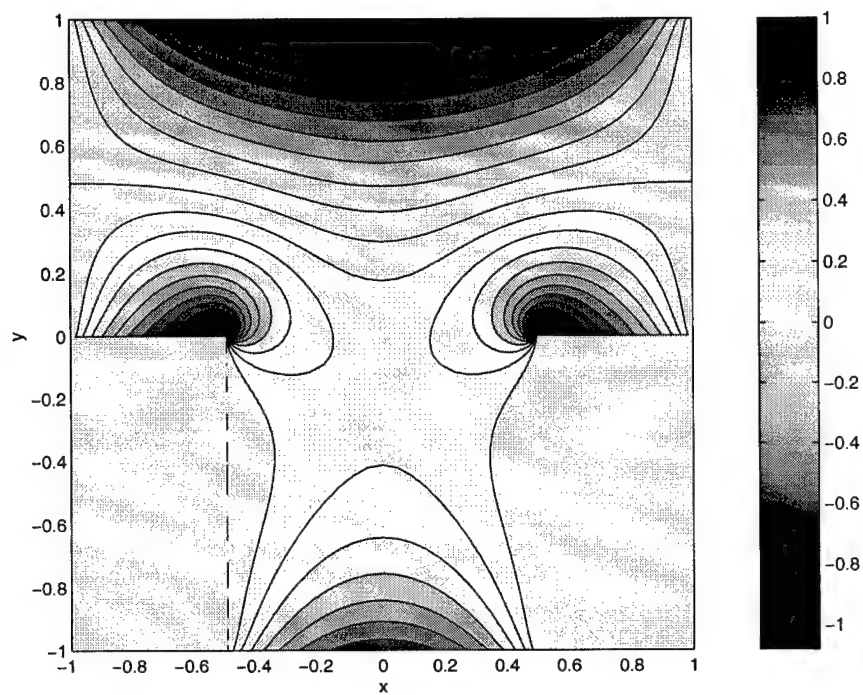
Figure 6. The velocity component $\bar{u}$ in a grooved channel geometry recovered using five subdomains
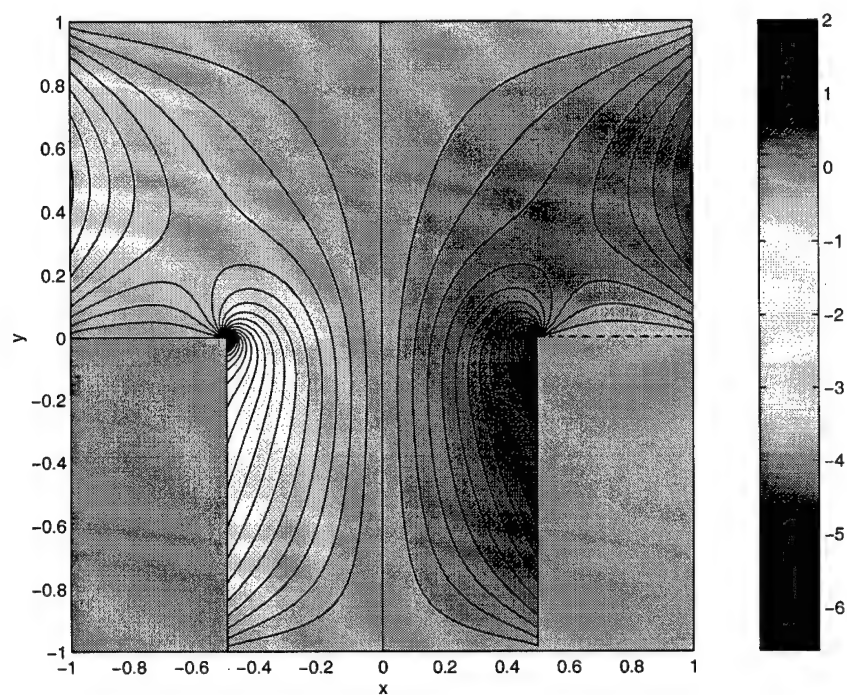
Figure 7. The velocity component $\bar{v}$ in a grooved channel geometry recovered using five subdomains
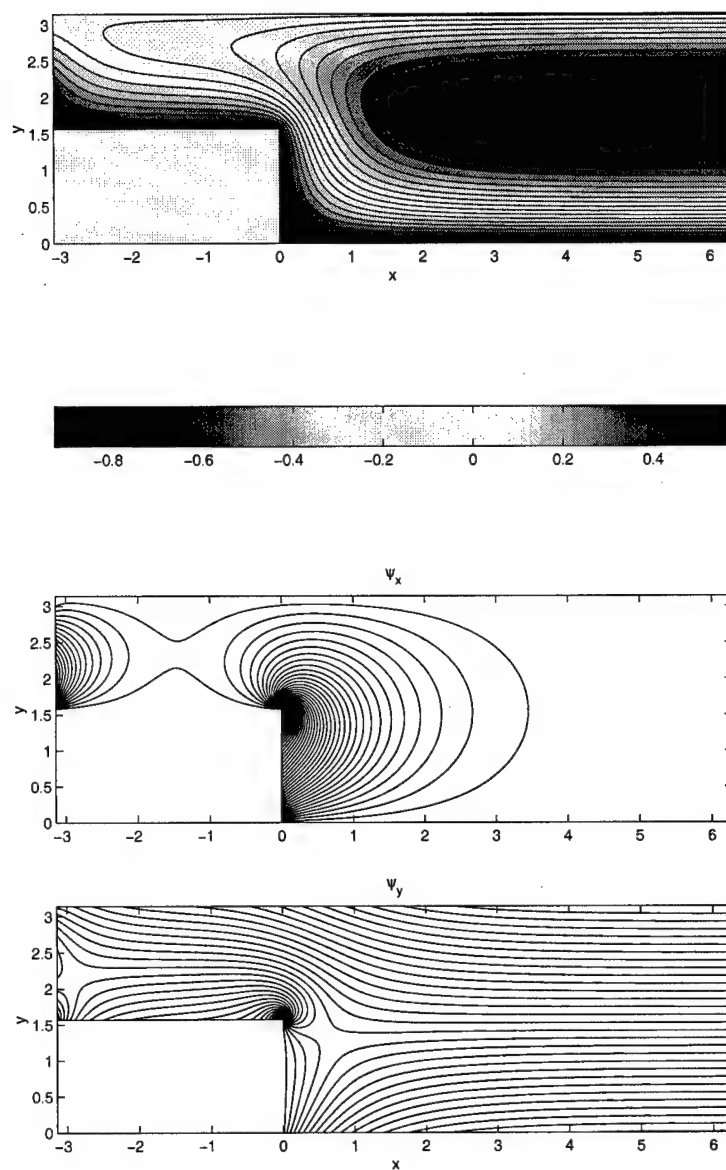
Figure 8. Solution of $\nabla^2 \psi = 1$ subject to the boundary conditions of Black (1997).
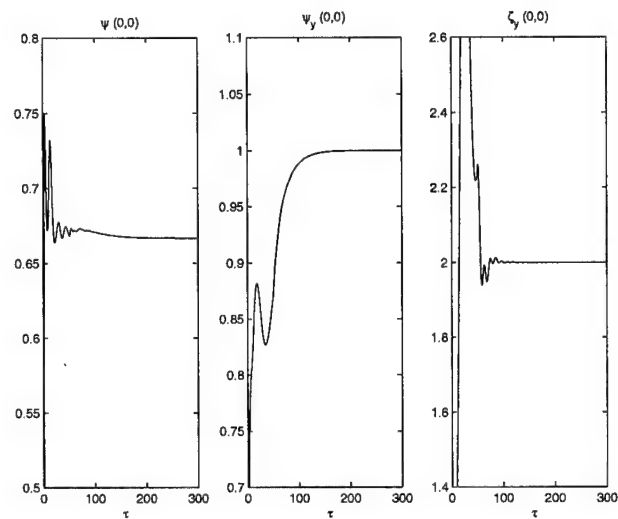
Figure 9. Spectral multidomain solution of the plane channel laminar basic flow. Shown are the flow streamfunction ψ (left), the streamwise velocity component $\bar{u}$ (centre) and the wall-normal derivative of the flow vorticity ζ (right) as functions of the number of iterations N and the relaxation parameter τ at $(x,y) = (0,0)$. $\tau = O(0.01)$ and $\tau = O(0.1)$ was used during the early and late iteration cycles, respectively.
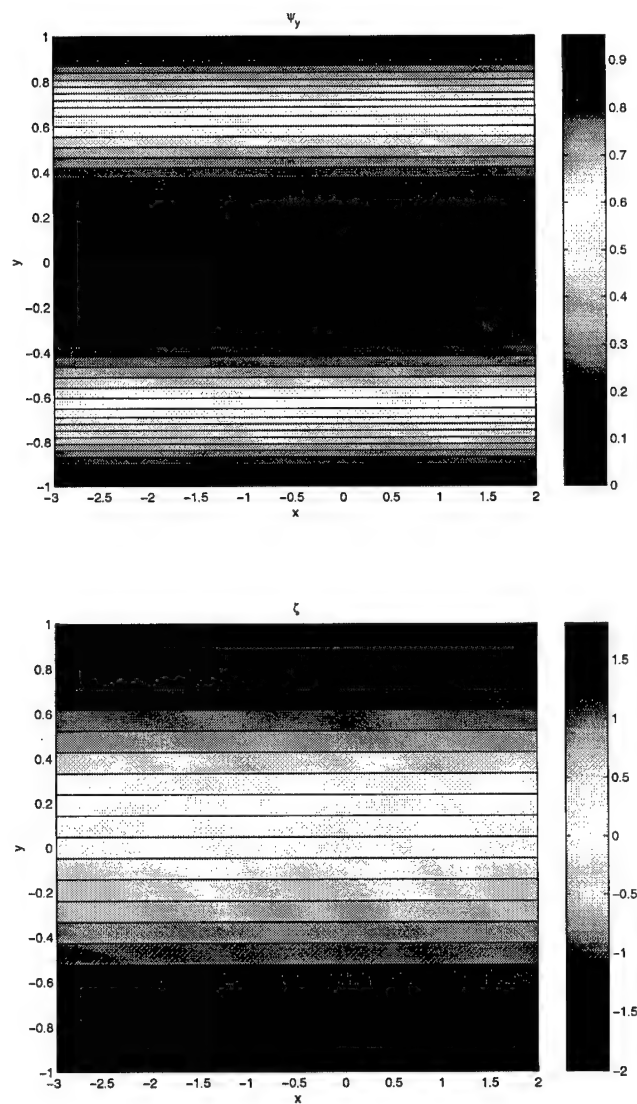
Figure 10. The streamwise velocity component and the vorticity in plane Poiseuille flow solved using two domains whose interface is at $x = 0$.
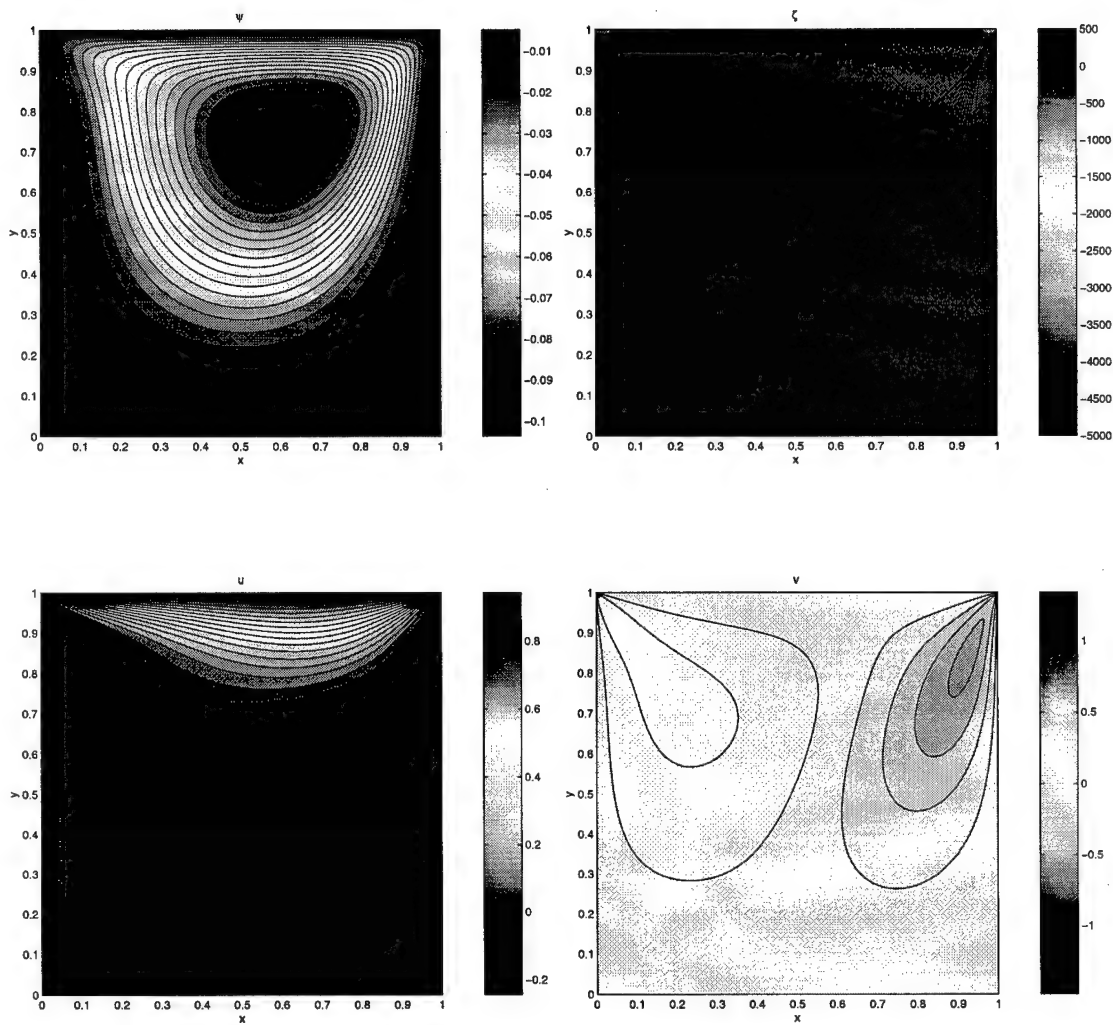
Figure 11. The streamfunction and vorticity (upper) and the velocity components (lower) in the square lid-driven cavity at $Re = 100$. Solution obtained using 48 collocation points per spatial direction in each of two domains whose interface is at $x = 0.5$.
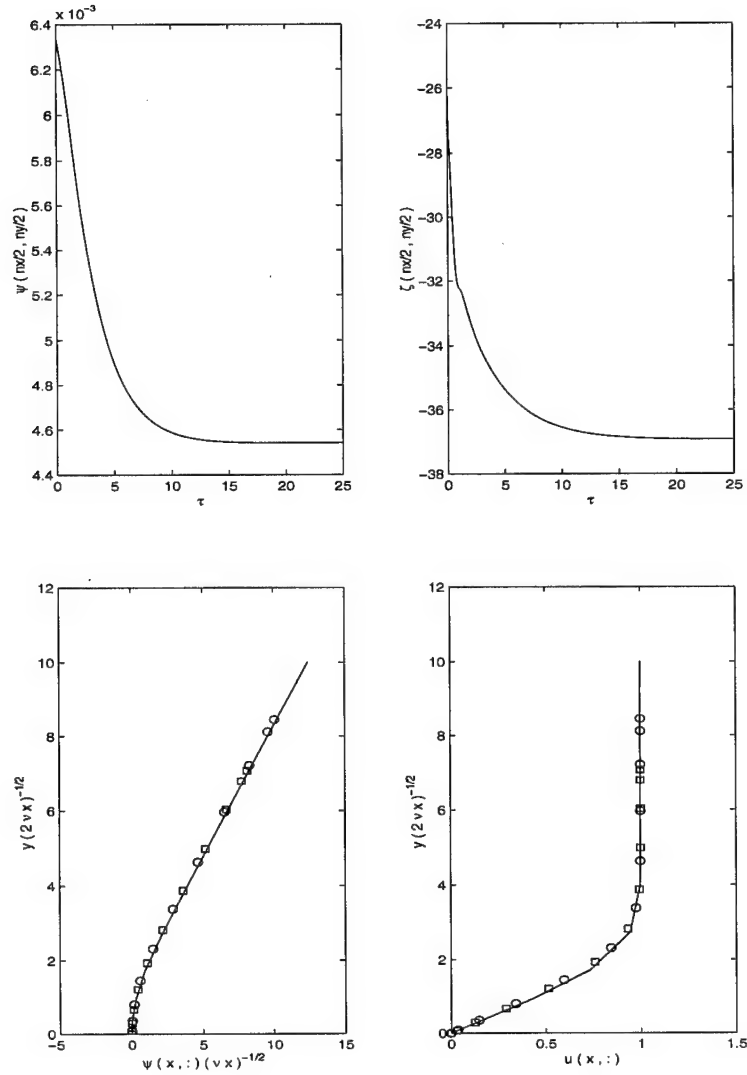
Figure 12. Upper: Convergence history of ψ (left) and ζ (right) as function of the time-like variable τ. Lower: Collapse of ψ (left) and ψ_y (right) on the respective Blasius profiles. The imposed at inflow Blasius solutions are indicated by the solid lines; results obtained at the interface of the domains are shown by ($\circ$) and those at the outflow boundary are denoted by ($\square$).
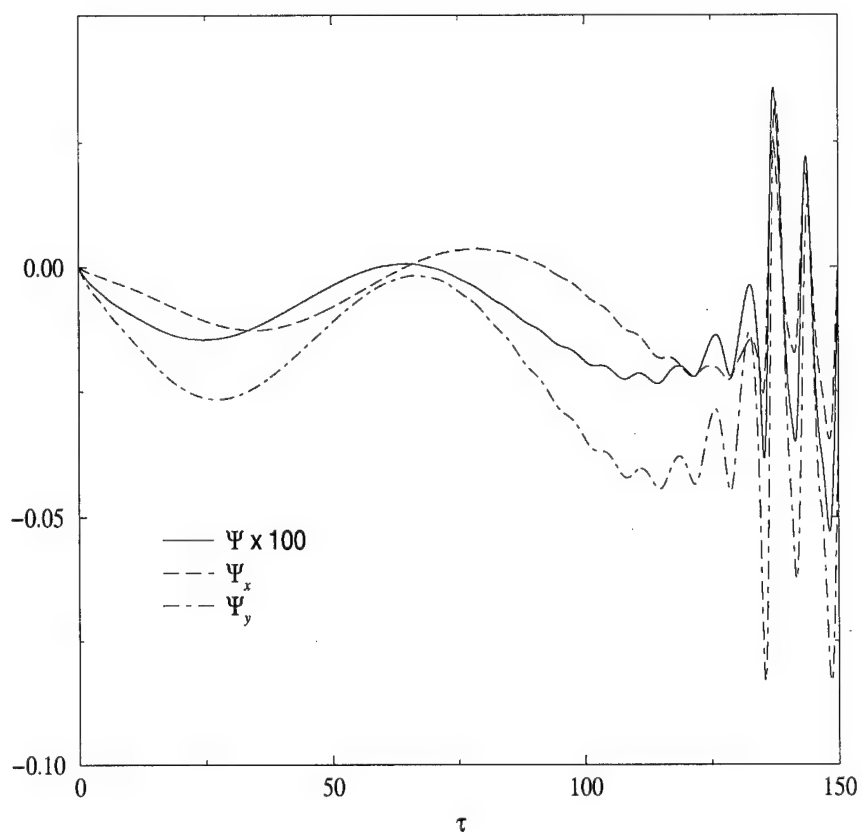
Figure 13. Instability of the numerical scheme in Blasius flow at low resolutions and high ω values.
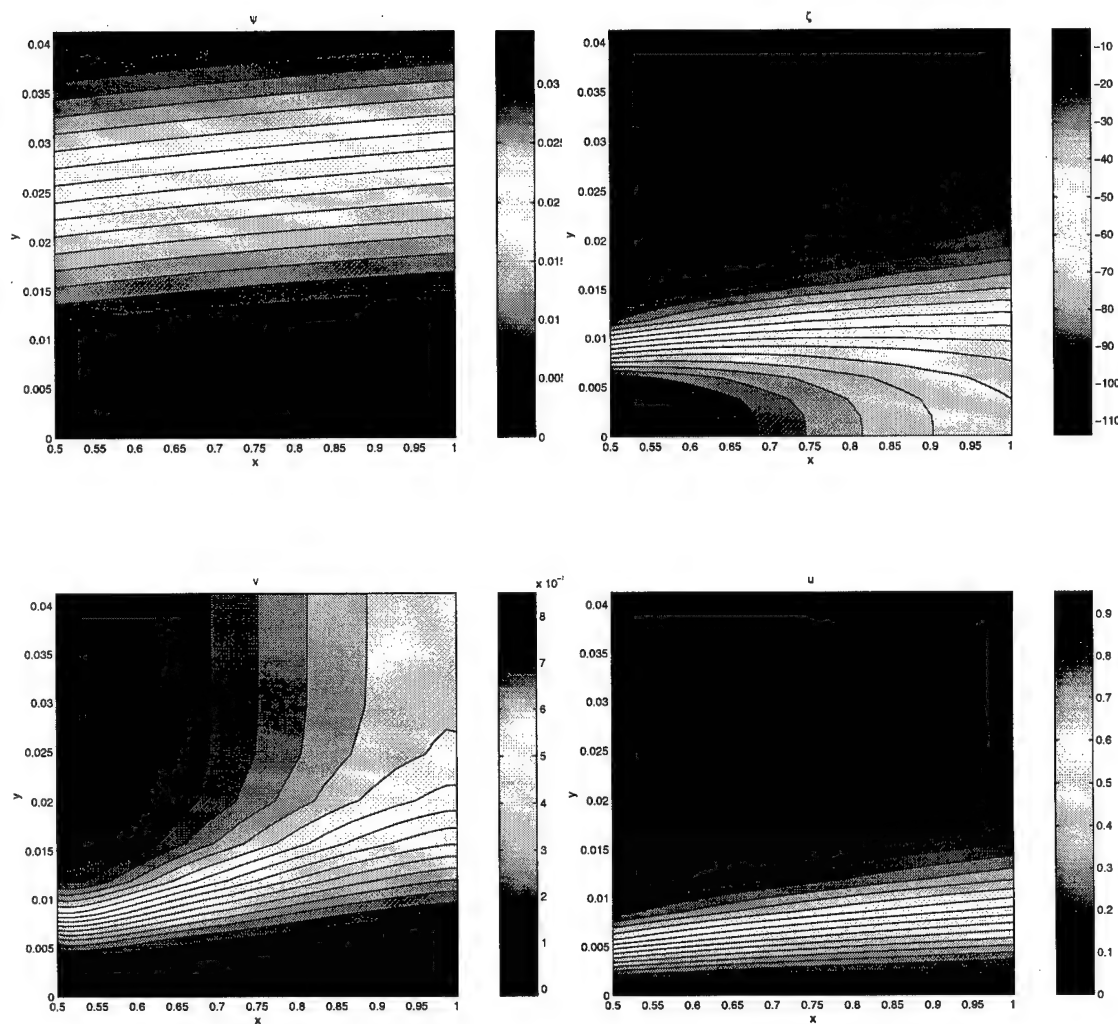
Figure 14. The streamfunction and vorticity (upper) and the velocity components (lower) in incompressible flow over a flat-plate. Solution obtained using 16 collocation points per spatial direction in each of the two subdomains connected at $x_c = 0.7$.
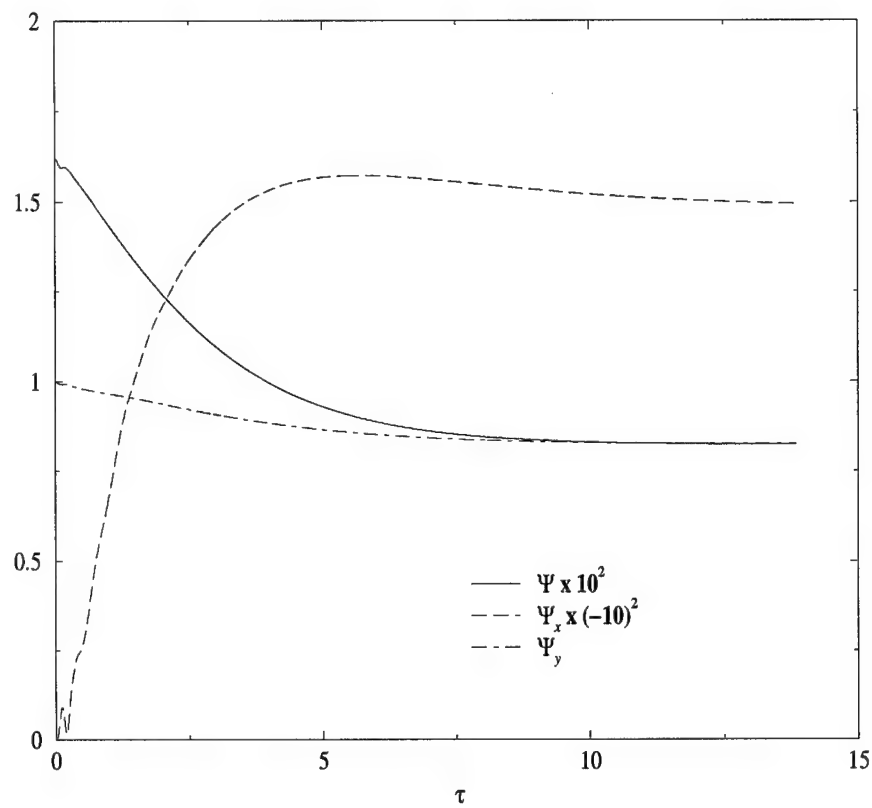
Figure 15. Iteration history of spectral multidomain Navier-Stokes solutions of a Blasius boundary layer, using 48^2 collocation points in each of two subdomains connected at $x_c = 0.21$.
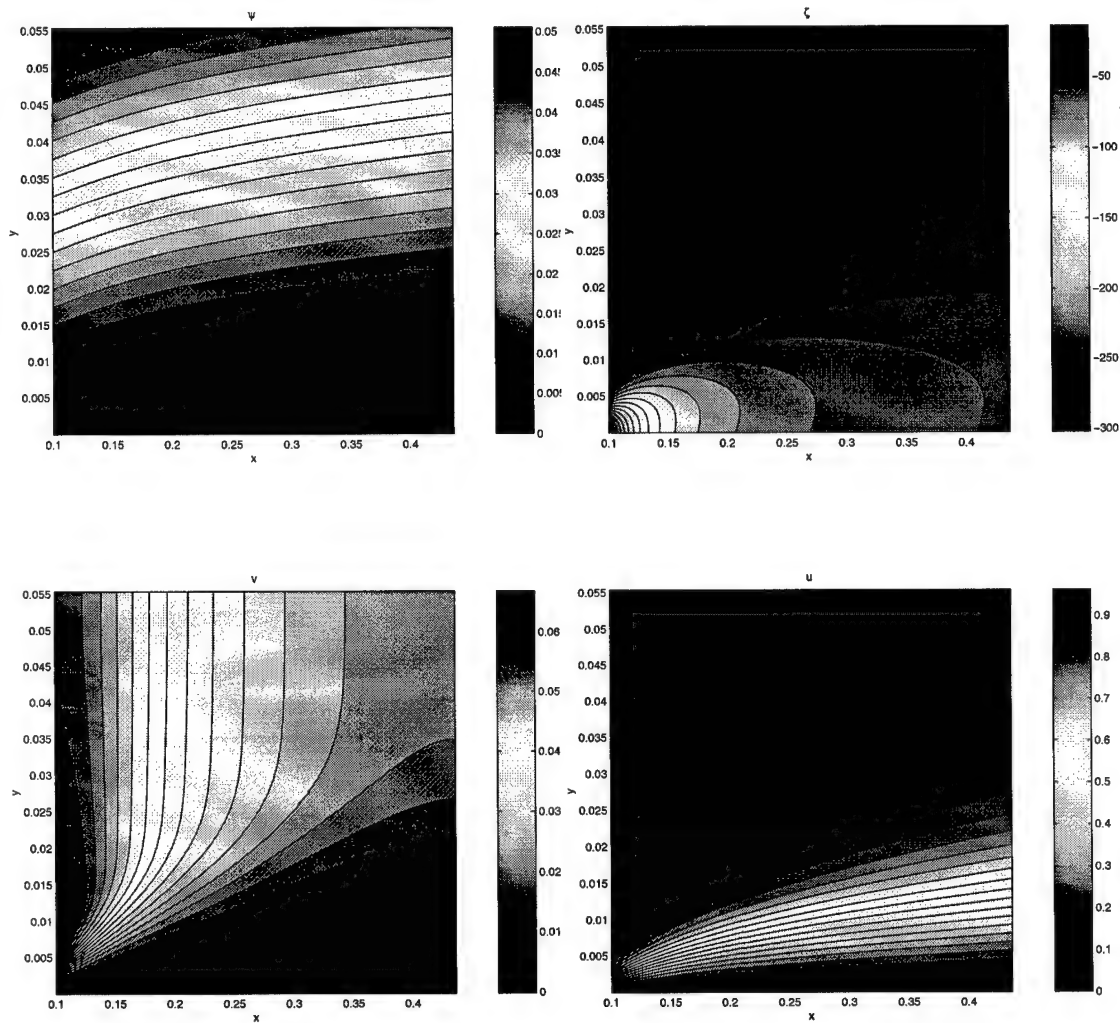
Figure 16. The streamfunction and vorticity (upper) and the velocity components (lower) in incompressible flow over a flat-plate. Solution obtained using 48 collocation points per spatial direction in each of the two subdomains connected at $x_c = 0.21$.
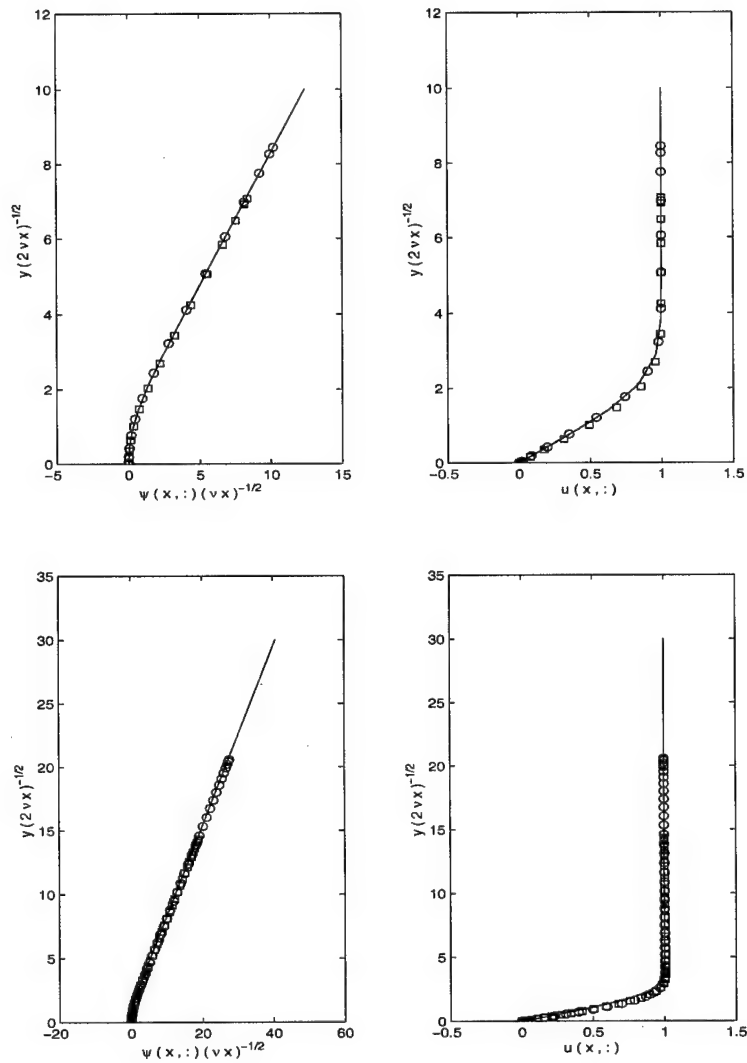
Figure 17. Collapse of ψ (left) and ψ_y (right) on the respective Blasius profiles. The imposed at inflow Blasius solutions are indicated by the solid lines; results obtained at the interface of the domains are shown by ($\circ$) and those at the outflow boundary are denoted by ($\square$). Upper: Calculation using 16×16 collocation points per subdomain. Lower: Calculation using 48×48 collocation points per subdoman.
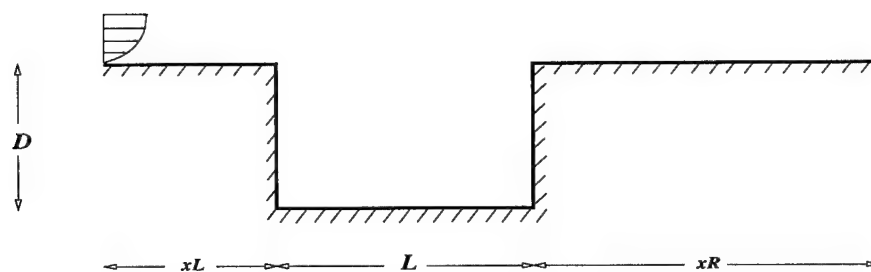
Figure 18. Schematic representation of the geometry and definition of parameters in the open-cavity flow.
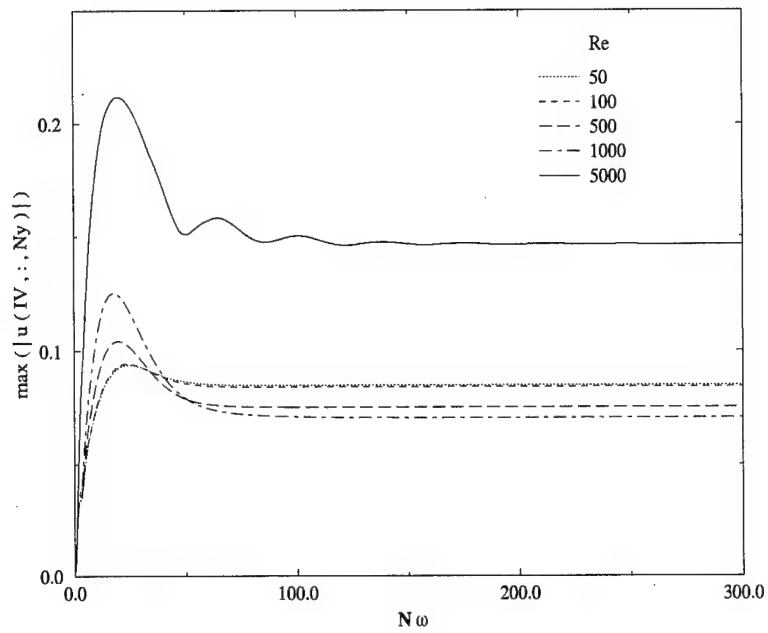
Figure 19. Iteration history of $\max(\bar{u})$ on the interface between subdomains II and IV at $\text{Re} = 50, 100, 500, 1000$ and 5000. Solutions obtained on 20^2 grids.
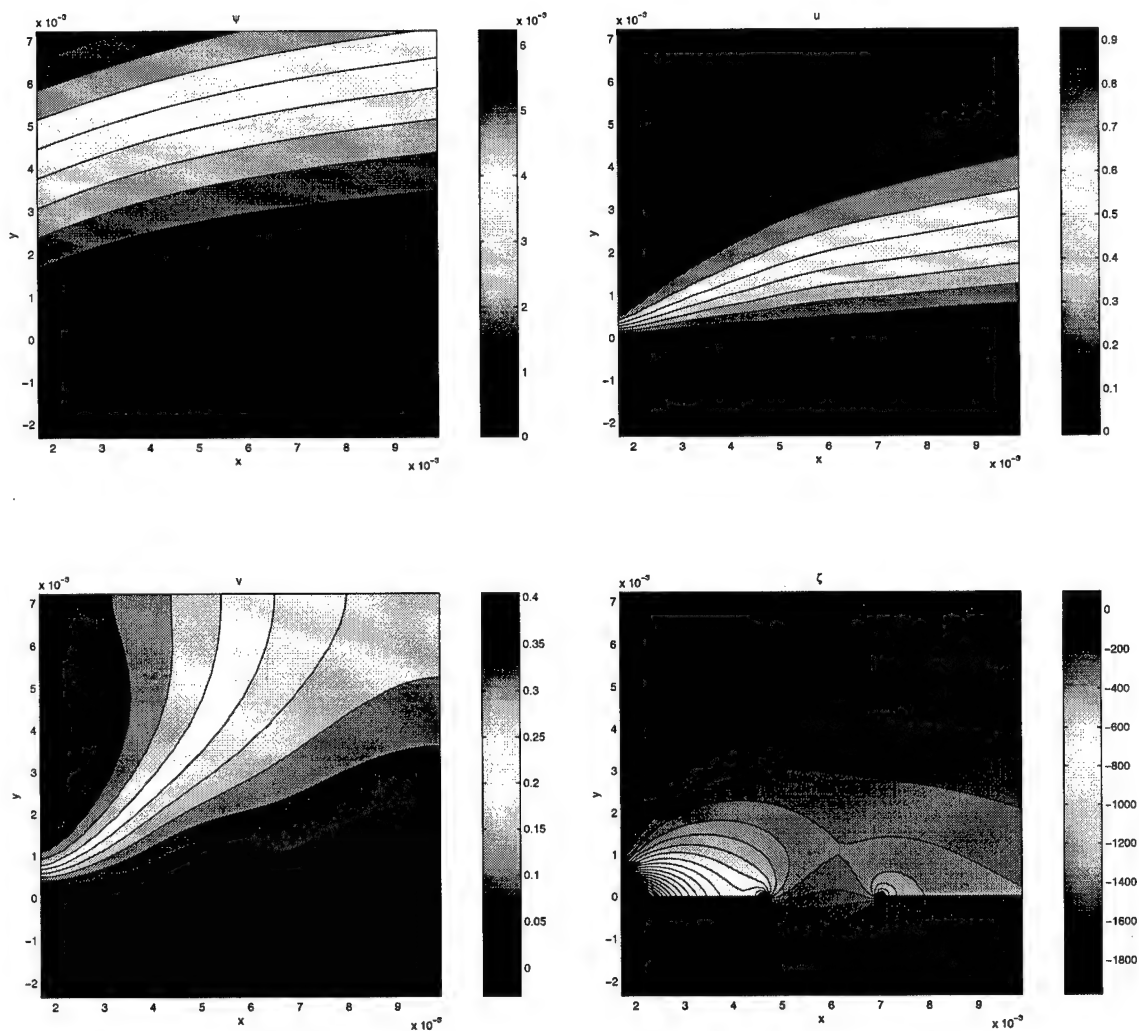
Figure 20. Steady-state solutions at Re = 100 obtained with 20^2 collocation points in each subdomain.
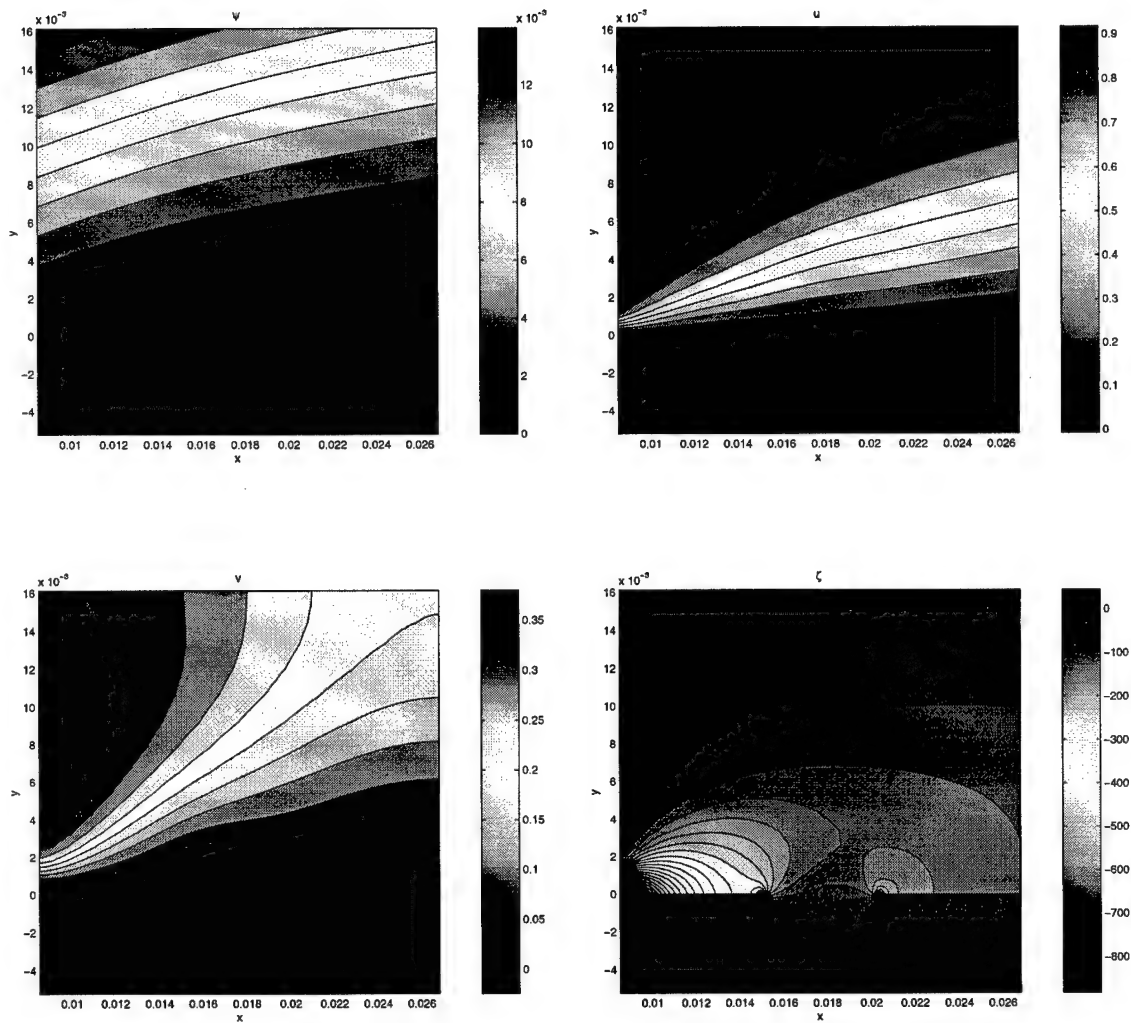
Figure 21. Steady-state solutions at $Re = 500$ obtained with 20^2 collocation points in each subdomain.
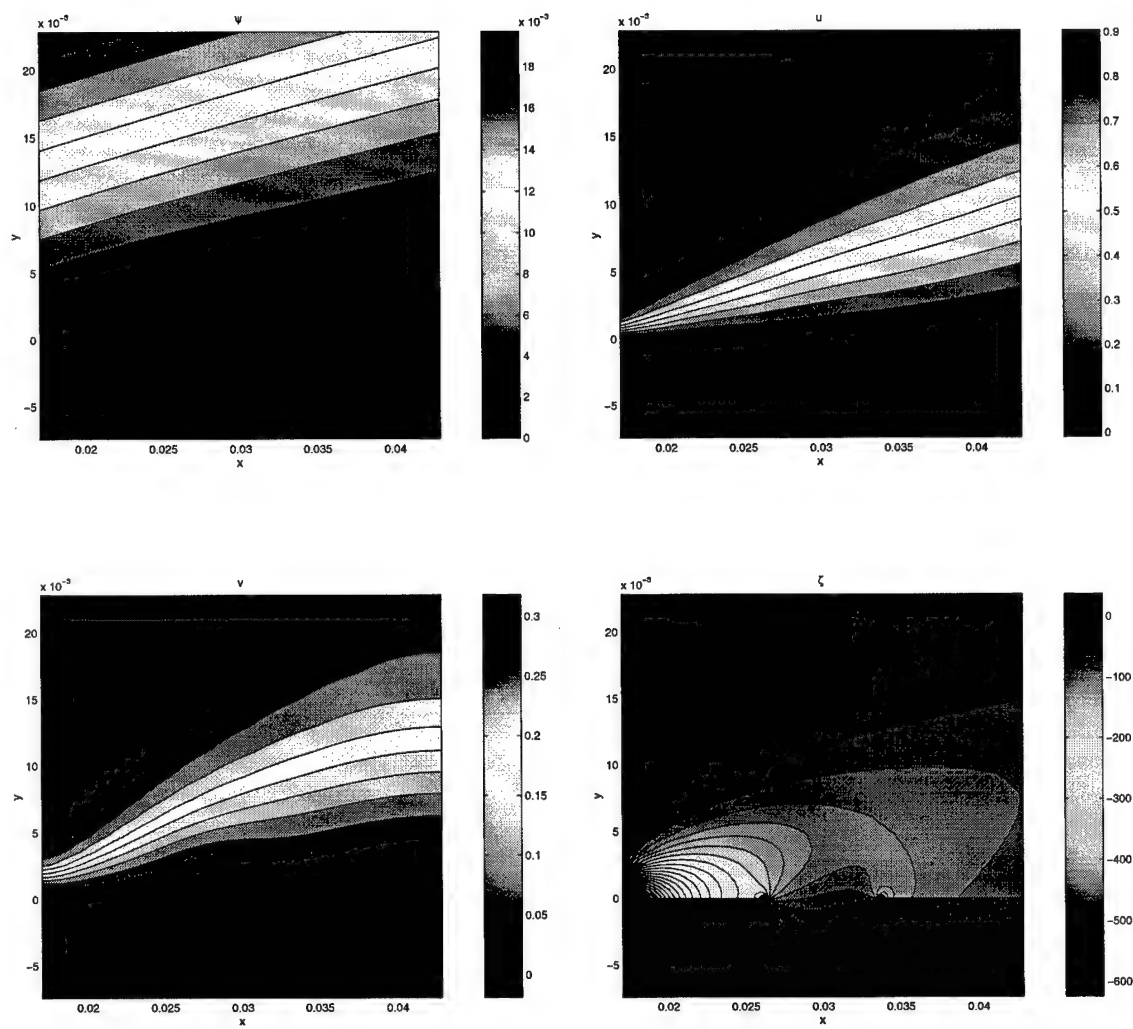
Figure 22. Steady-state solutions at Re = 1000 obtained with 20^2 collocation points in each subdomain.
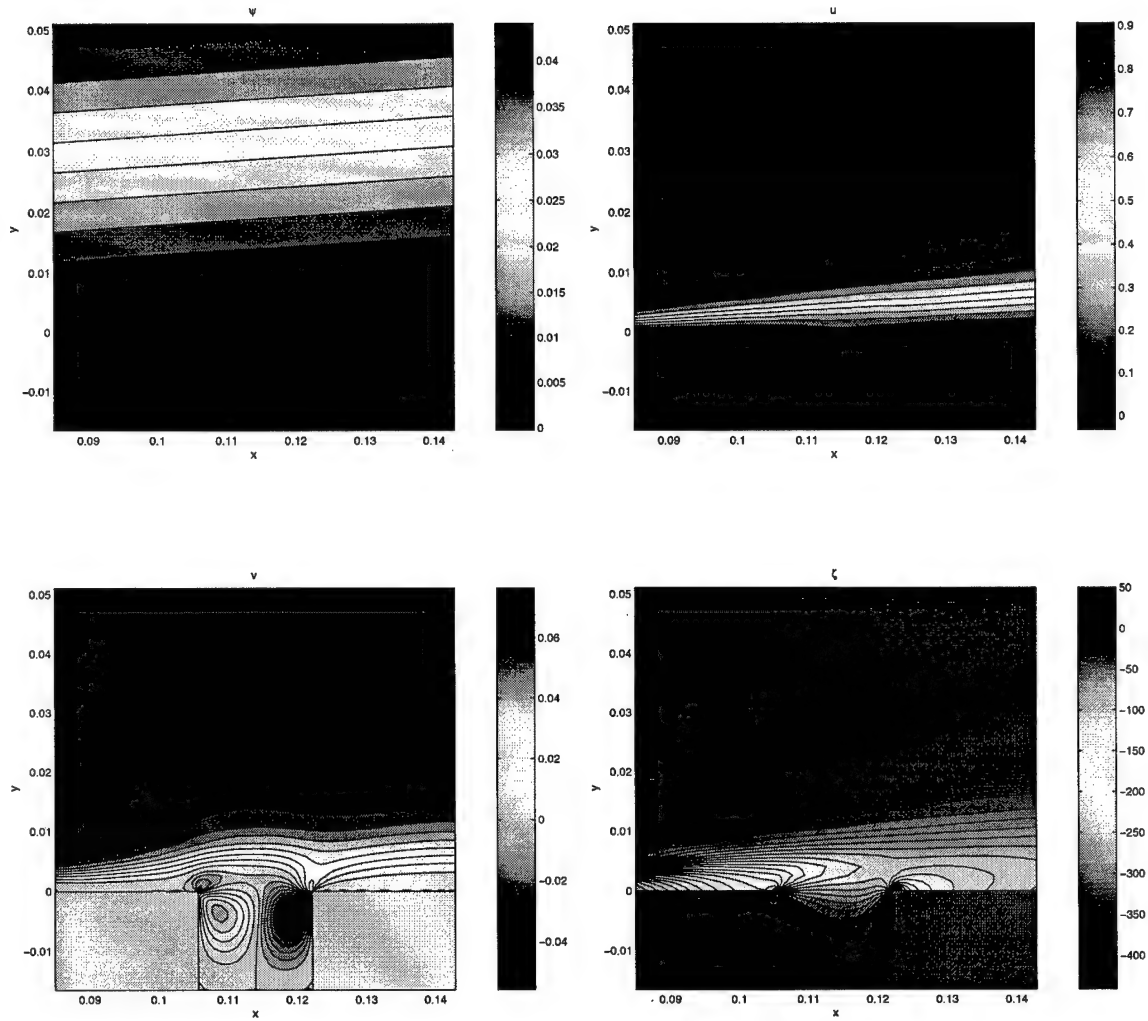
Figure 23. Steady-state solutions at $\mathrm{Re} = 5000$ obtained with 20^2 collocation points in each subdomain.
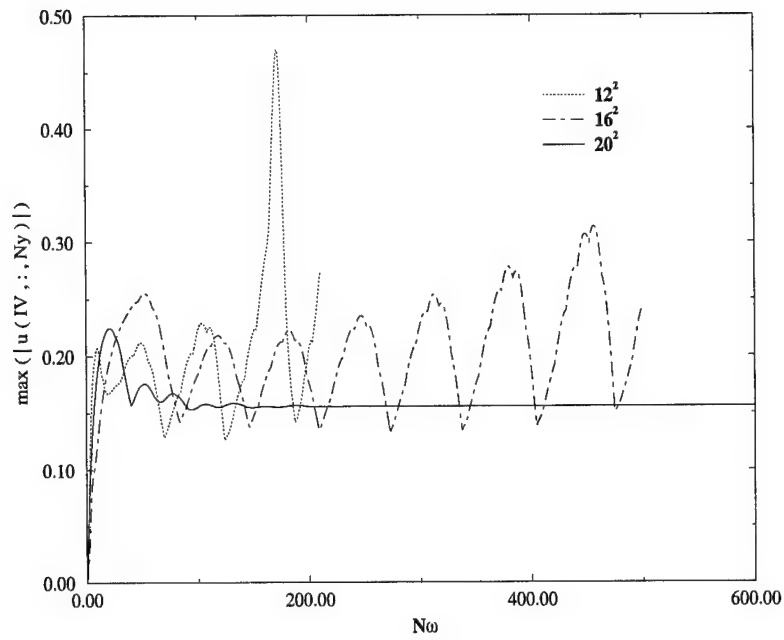
Figure 24. Iteration history of $\max(\bar{u})$ at the midpoint of the interface between subdomains II and IV at $\mathrm{Re} = 6000$ and spatial resolutions comprising $12^2, 16^2$ and 20^2 collocation points in each subdomain.

V. Theofilis
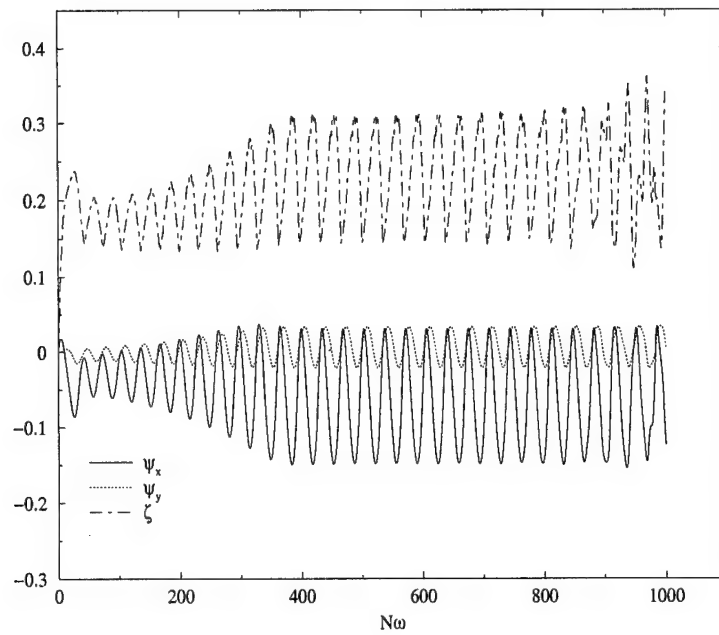
Figure 25. Oscillatory open cavity solutions obtained on account of poor spatial resolution using 16^2 collocation points in each subdomain. Shown are the values of ψ_x, ψ_y and ζ at the midpoint of the interface between subdomains II and IV.
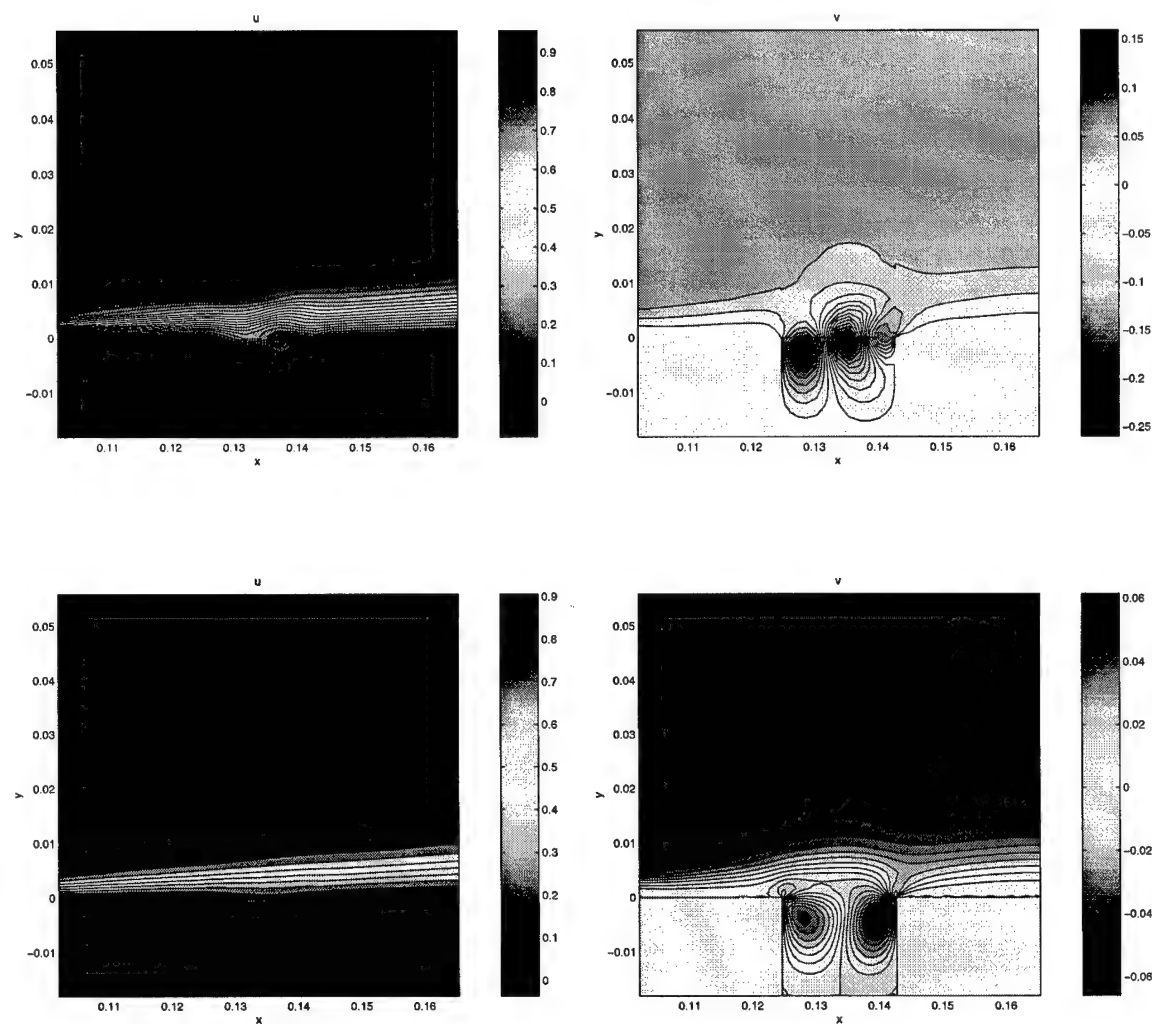
Figure 26. Upper: transient oscillatory solutions of the velocity components in the open cavity corresponding to the result of Figure 25. Lower: steady-state solutions of the same quantities obtained with 20^2 collocation points in each subdomain.
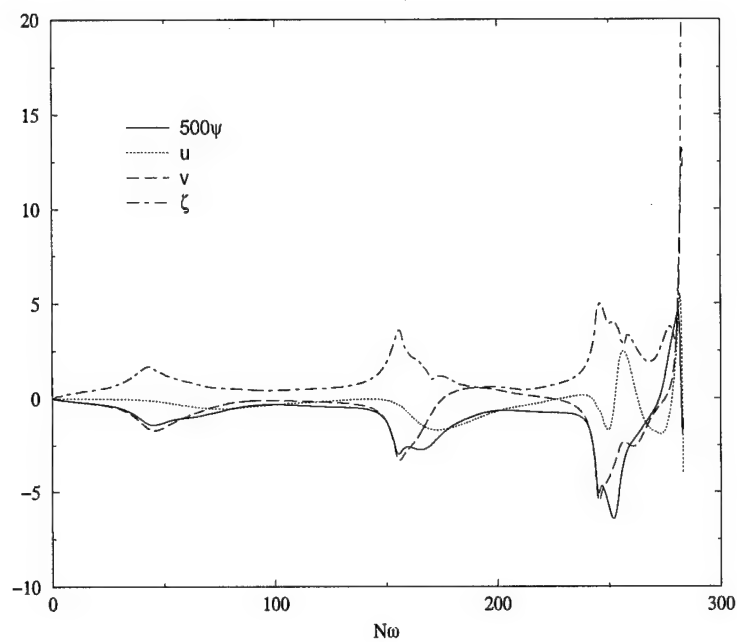
Figure 27. Iteration history of ψ, ψ_x, ψ_y and ζ at the midpoint of the interface between subdomains II and IV at $\mathrm{Re} = 7000$ and a spatial resolution comprising 32^2 collocation points in each subdomain.
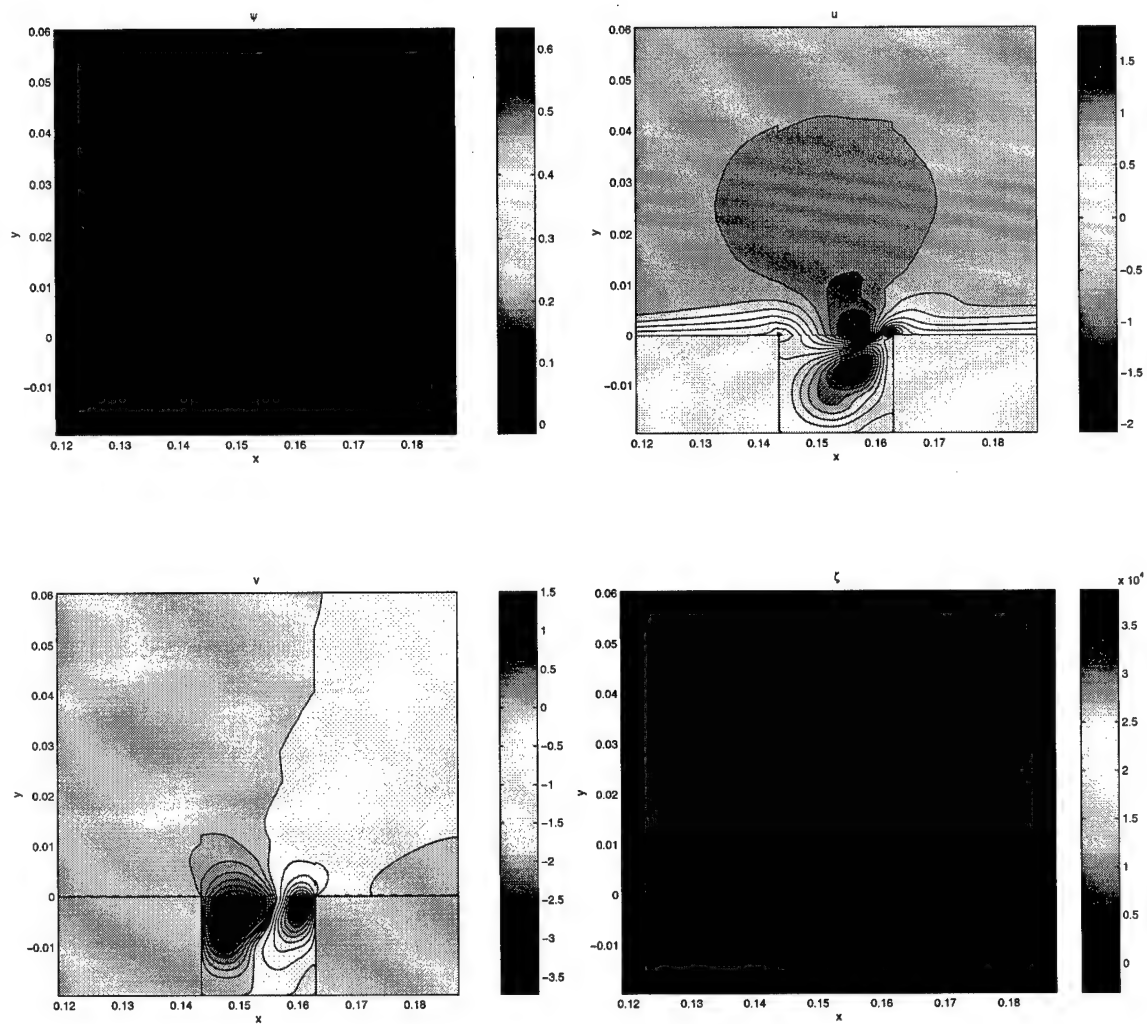
Figure 28. Transient solution shortly before numerical instability sets in at Re = 7000.
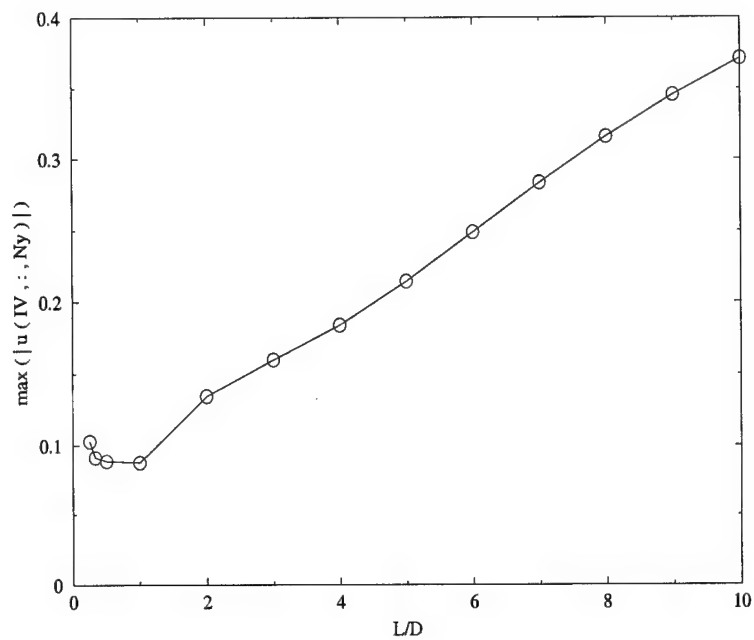
Figure 29. The dependence of the maximum value of ψ_y, taken at the midpoint of the interface between subdomains II and IV, in cavities of aspect ratio L/D.
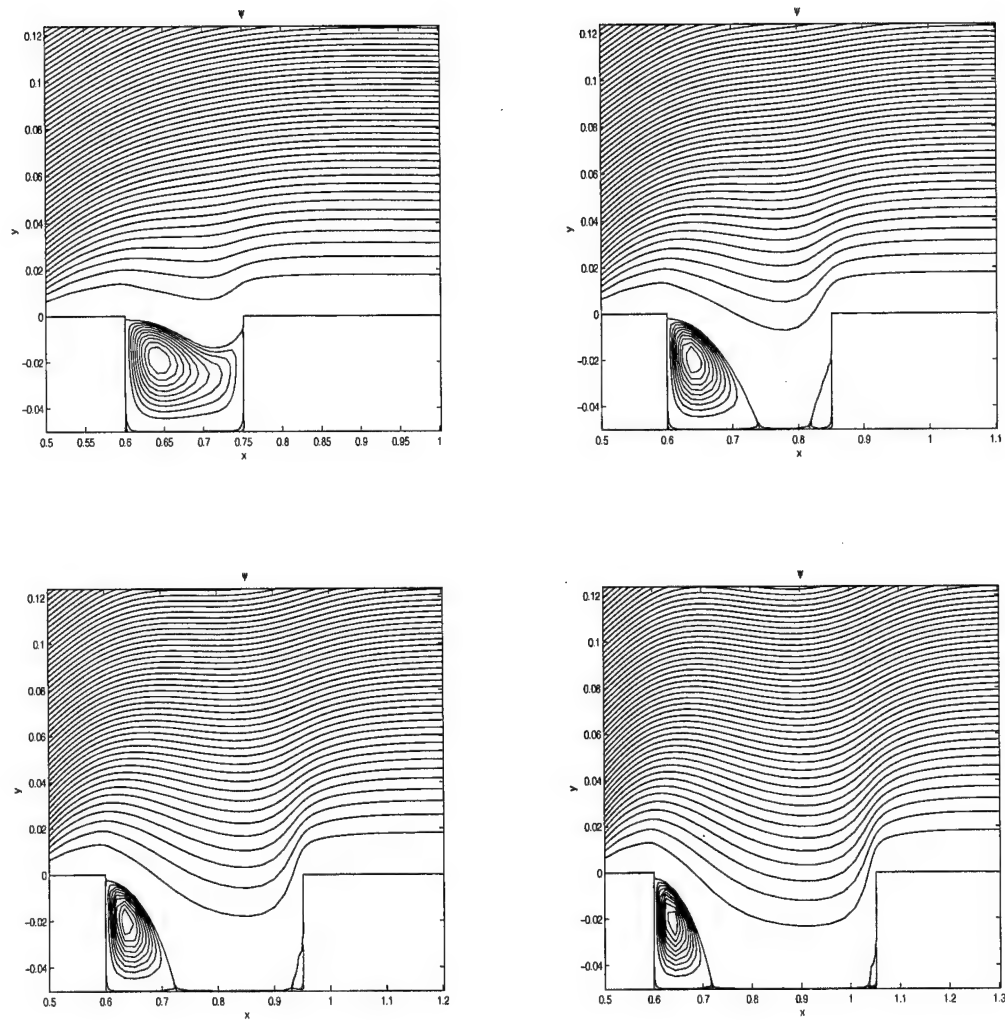
Figure 30. Wide Open Cavities: Isolines of ψ at $L/D = 3, 5, 7$ and 9.
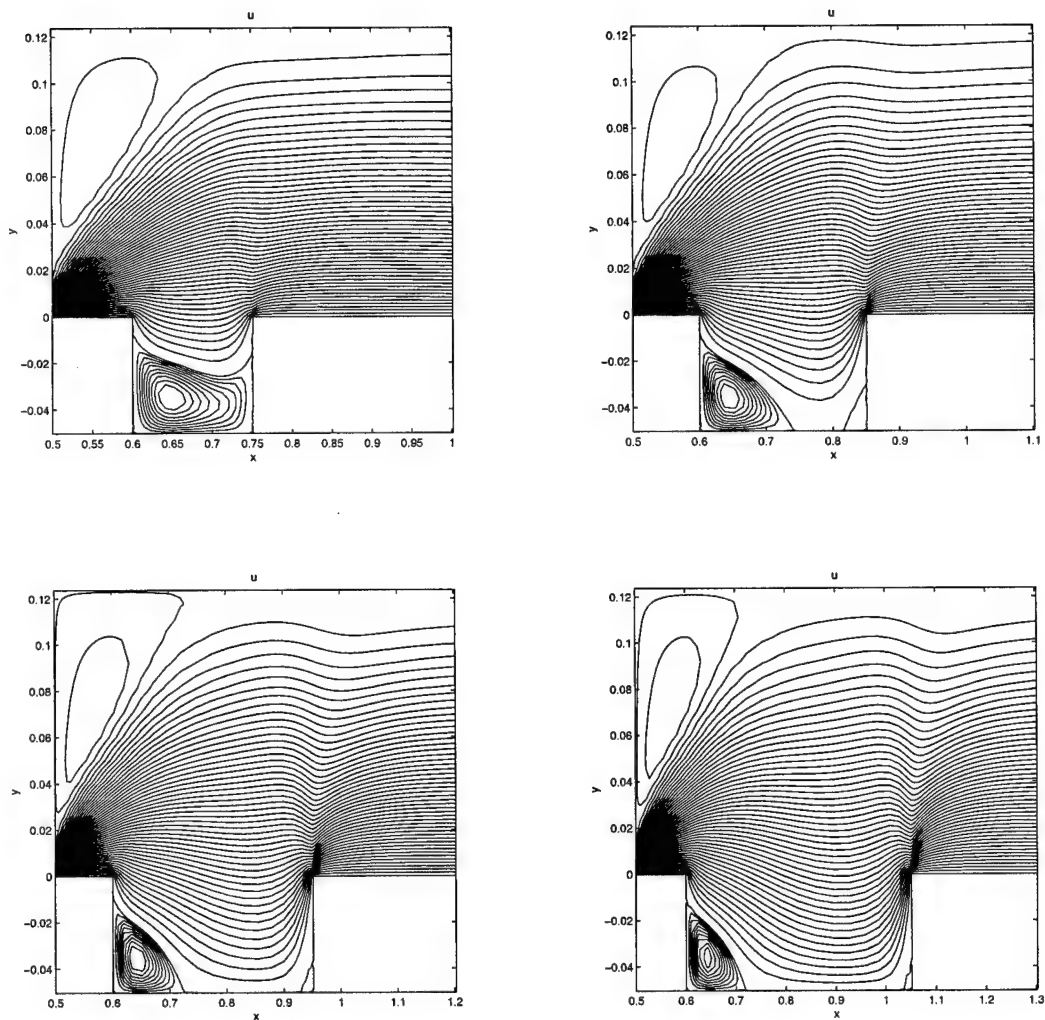
Figure 31. Wide Open Cavities: Isolines of u at $L/D = 3, 5, 7$ and 9.
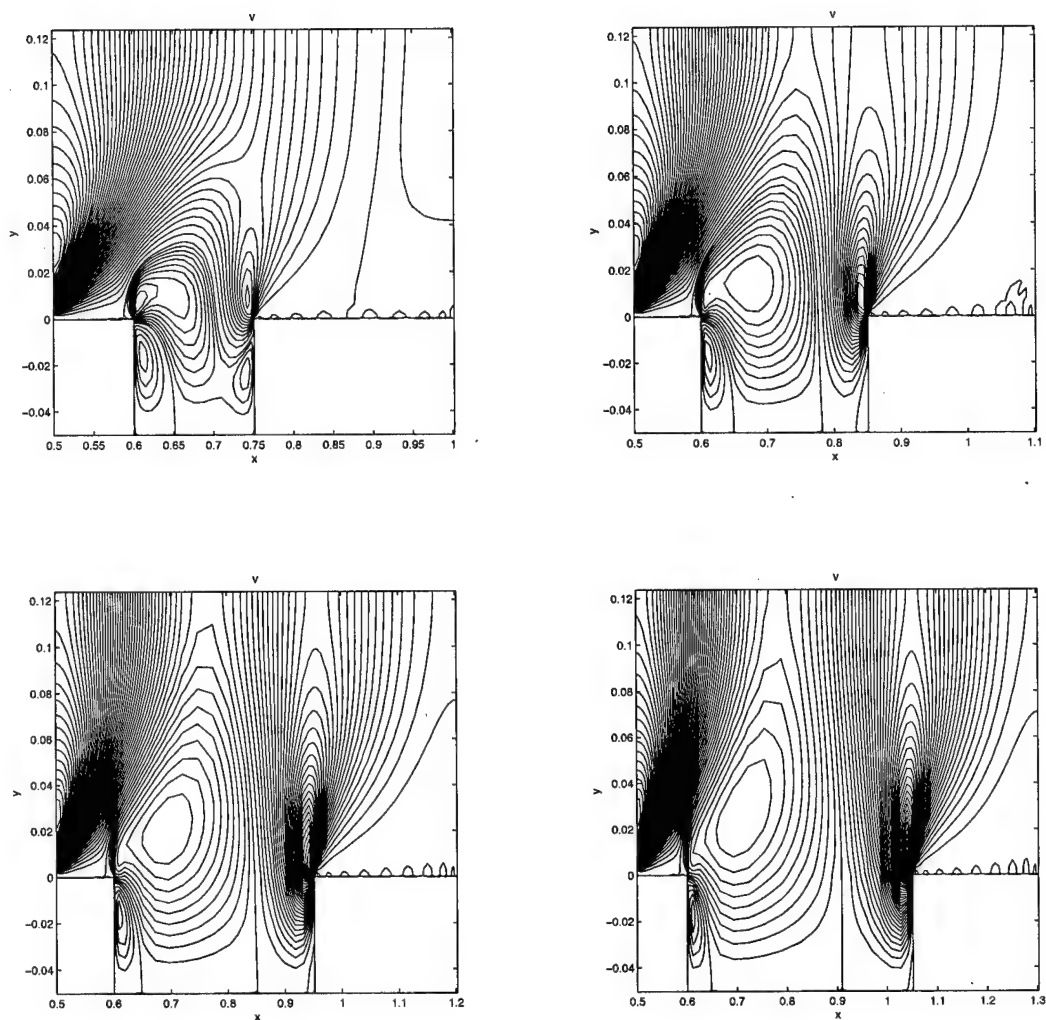
Figure 32. Wide Open Cavities: Isolines of v at $L/D = 3, 5, 7$ and 9.

V. Theofilis
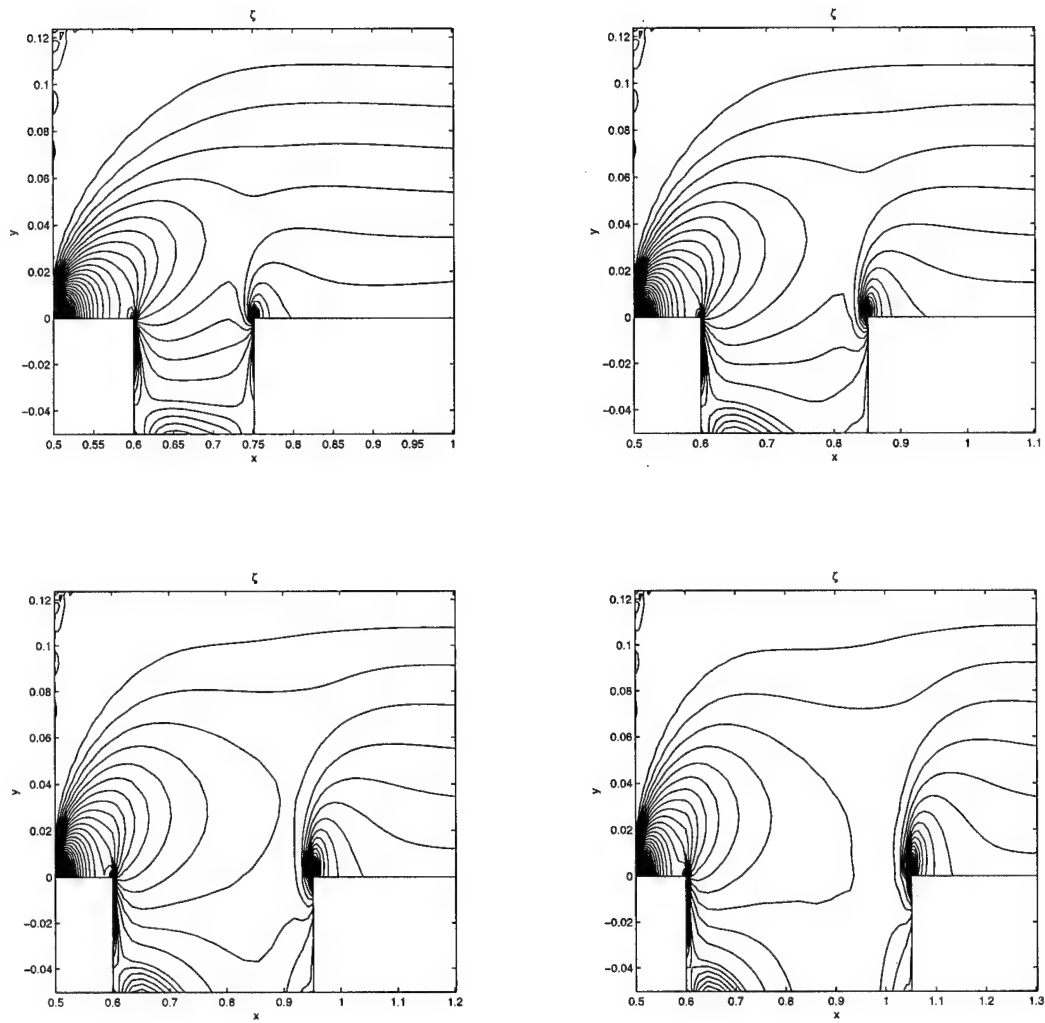
Figure 33. Wide Open Cavities: Isolines of ζ at $L/D = 3, 5, 7$ and 9.
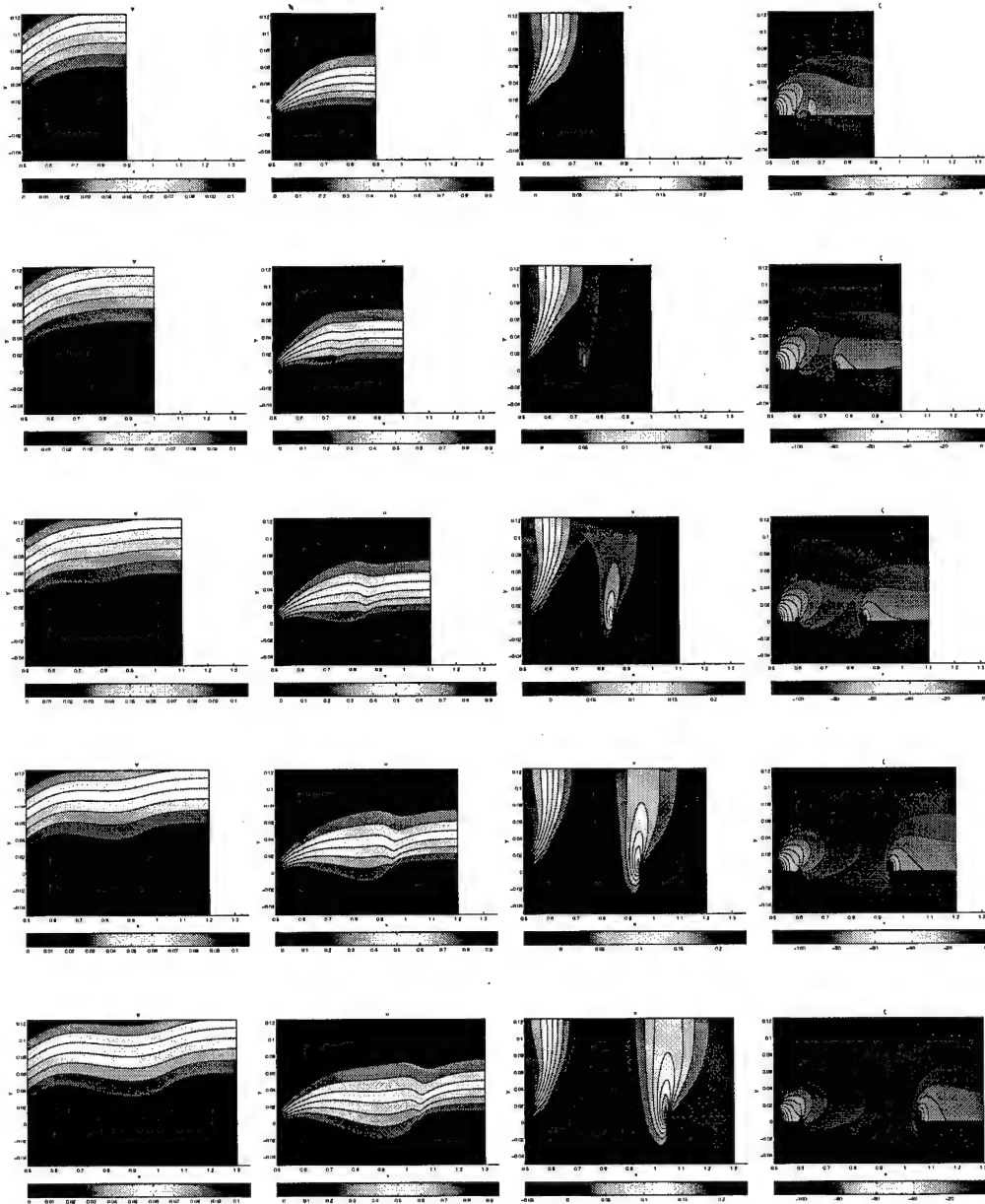
Figure 34. Steady-state rectangular open cavity solutions. Left to right column: $\psi, \psi_y, \psi_x, \zeta$. Upper to lower row: $L/D = 1, 3, 5, 7, 9$ with $D = 10\delta^*$ and δ^* the flat-plate boundary layer displacement thickness at the inflow boundary. A spatial discretisation comprising 20^2 collocation points in each subdomain was used.
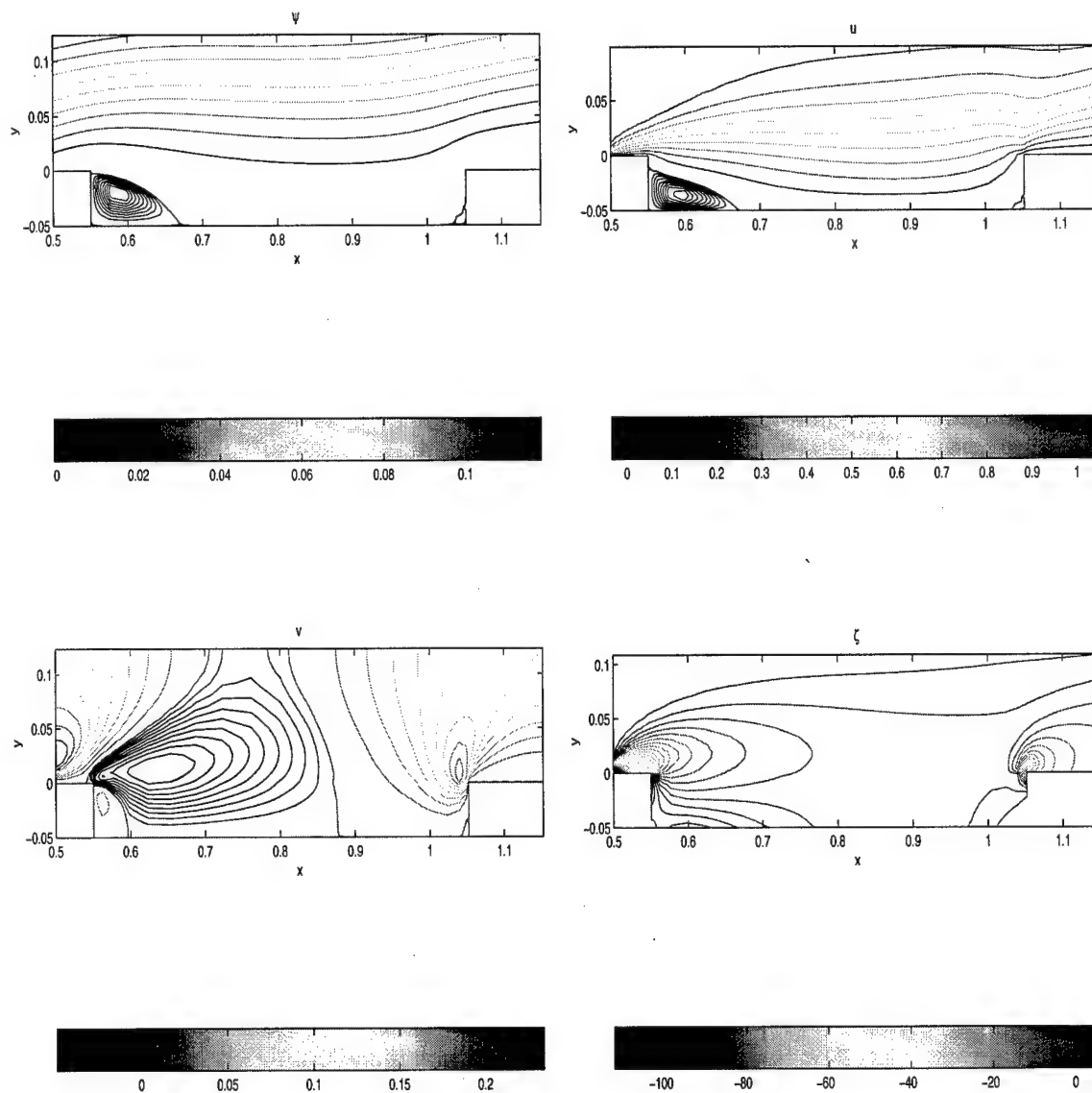
Figure 35. Steady-state open cavity solutions at $L/D = 10$. The backward- and forward-facing step flow patterns are visible at the upstream and downstream vertical walls of the open cavity, respectively.
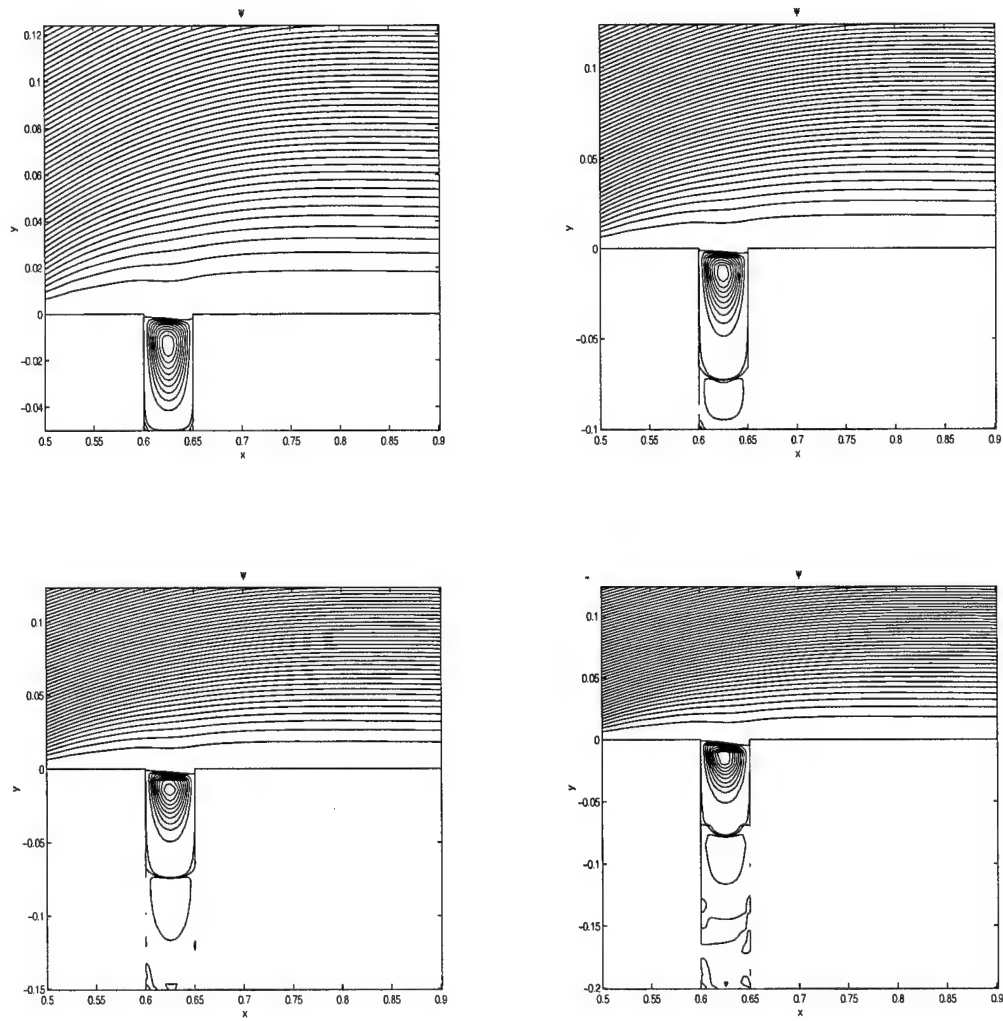
Figure 36. Deep Open Cavities: Isolines of ψ at $D/L = 1, 2, 3$ and 4.
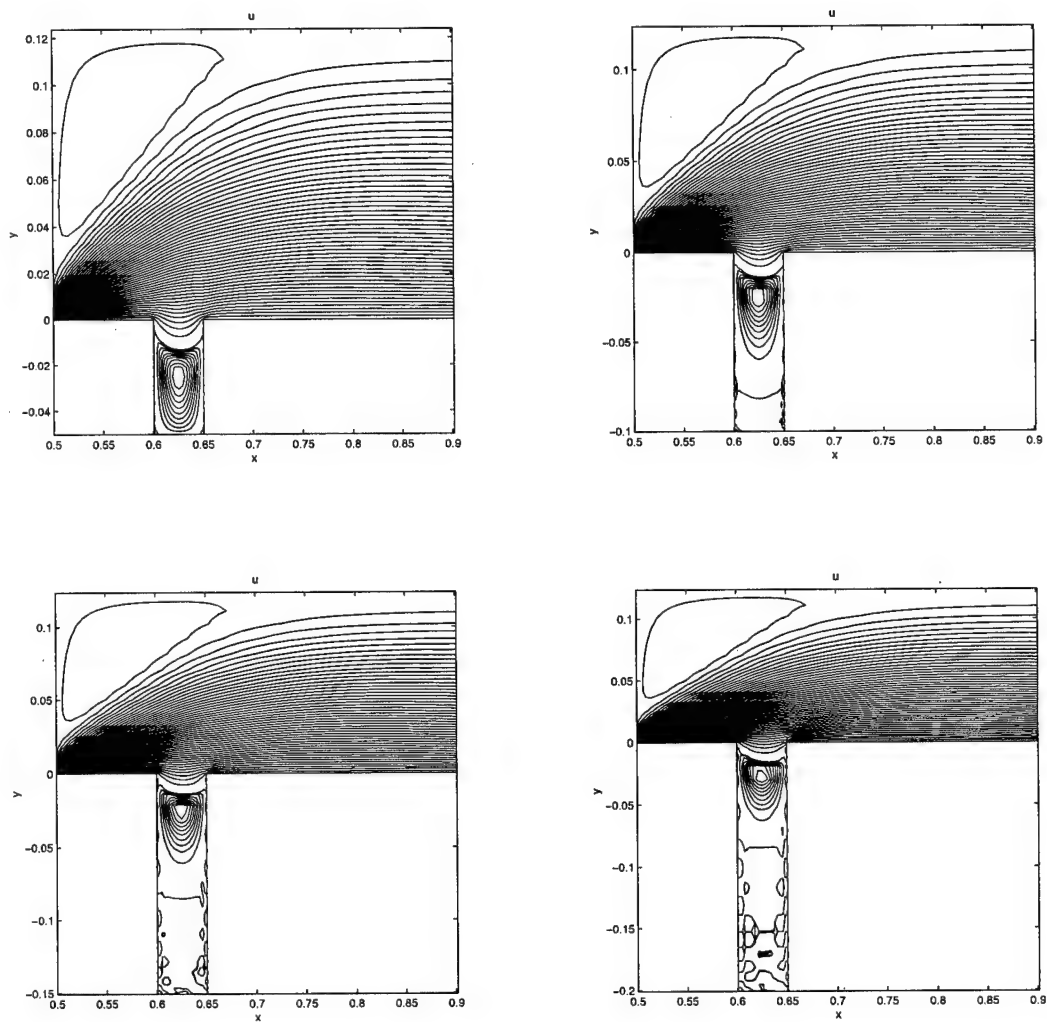
Figure 37. Deep Open Cavities: Isolines of u at $D/L = 1, 2, 3$ and 4.
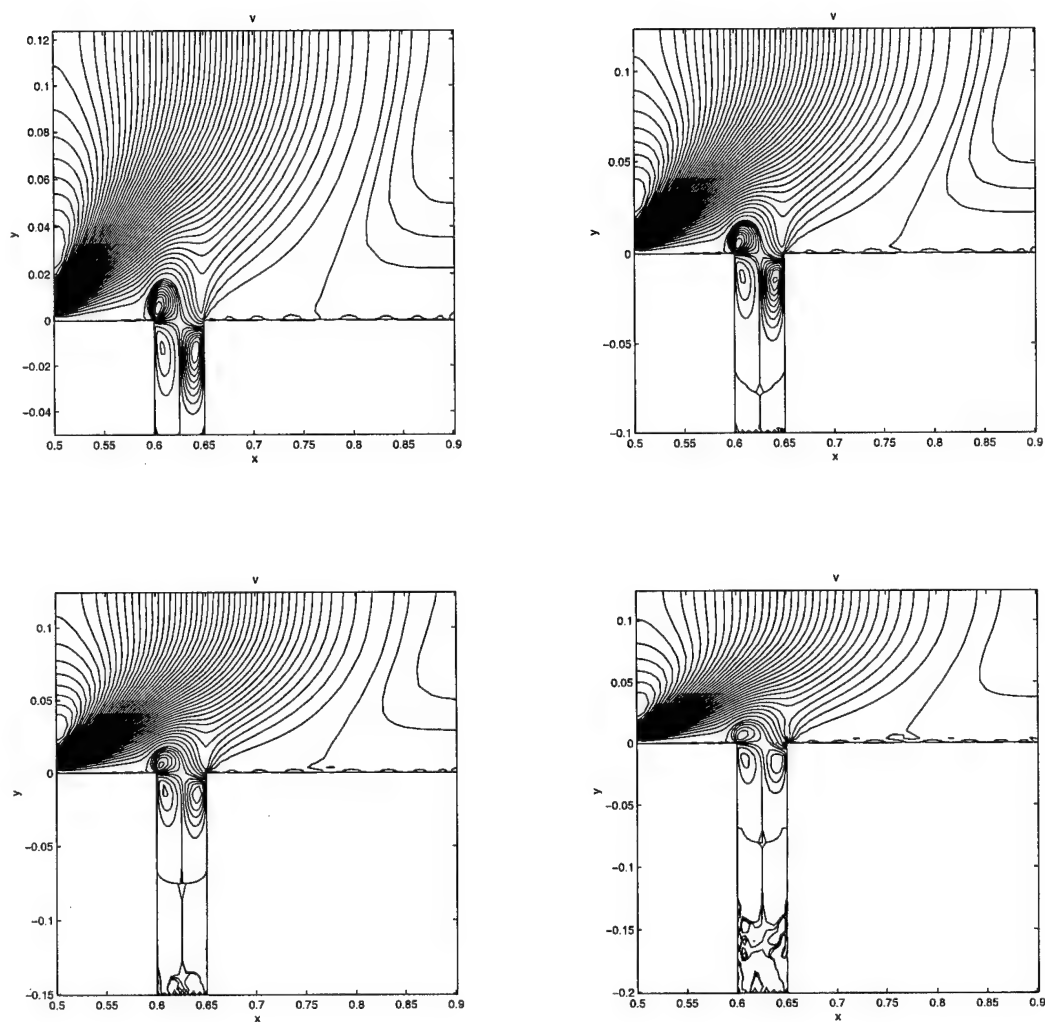
Figure 38. Deep Open Cavities: Isolines of v at $D/L = 1, 2, 3$ and 4.

V. Theofilis
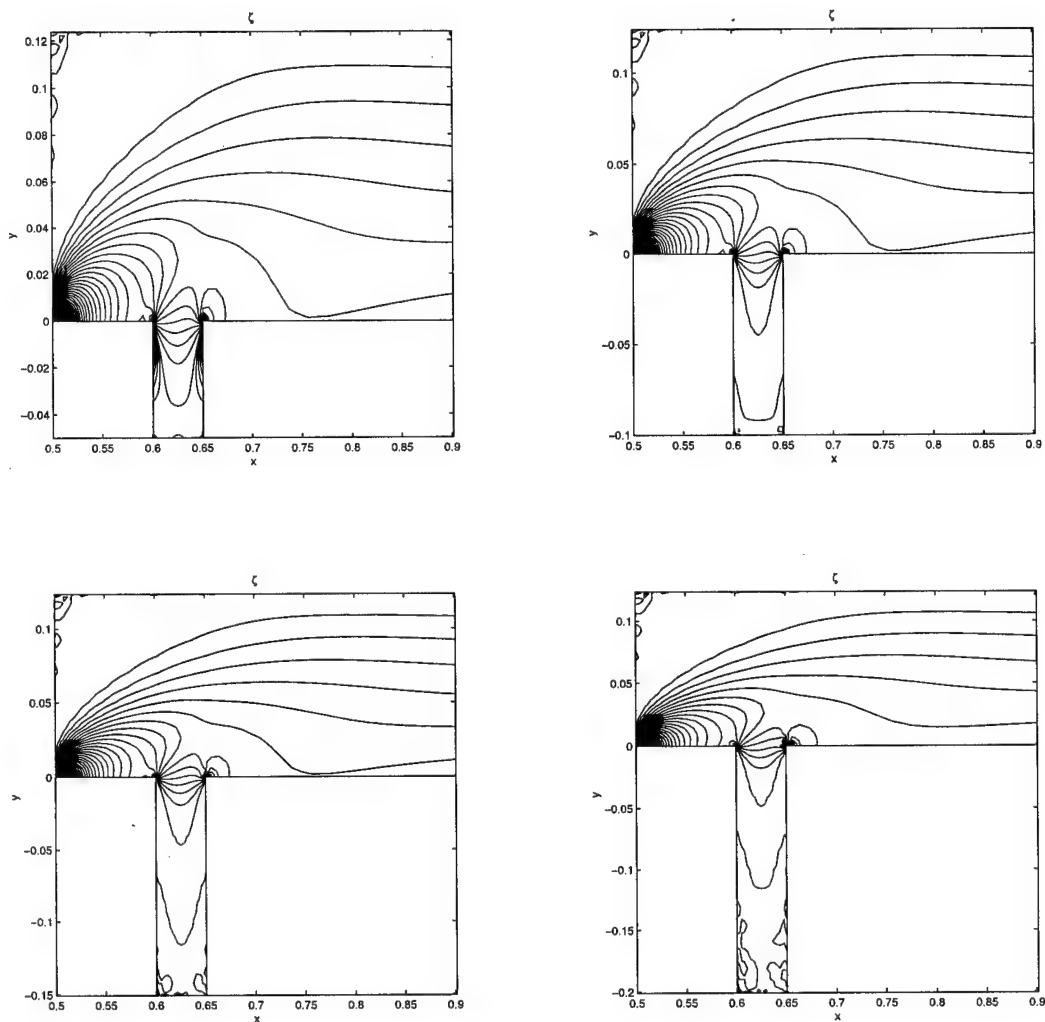
Figure 39. Deep Open Cavities: Isolines of ζ at $D/L = 1, 2, 3$ and 4.
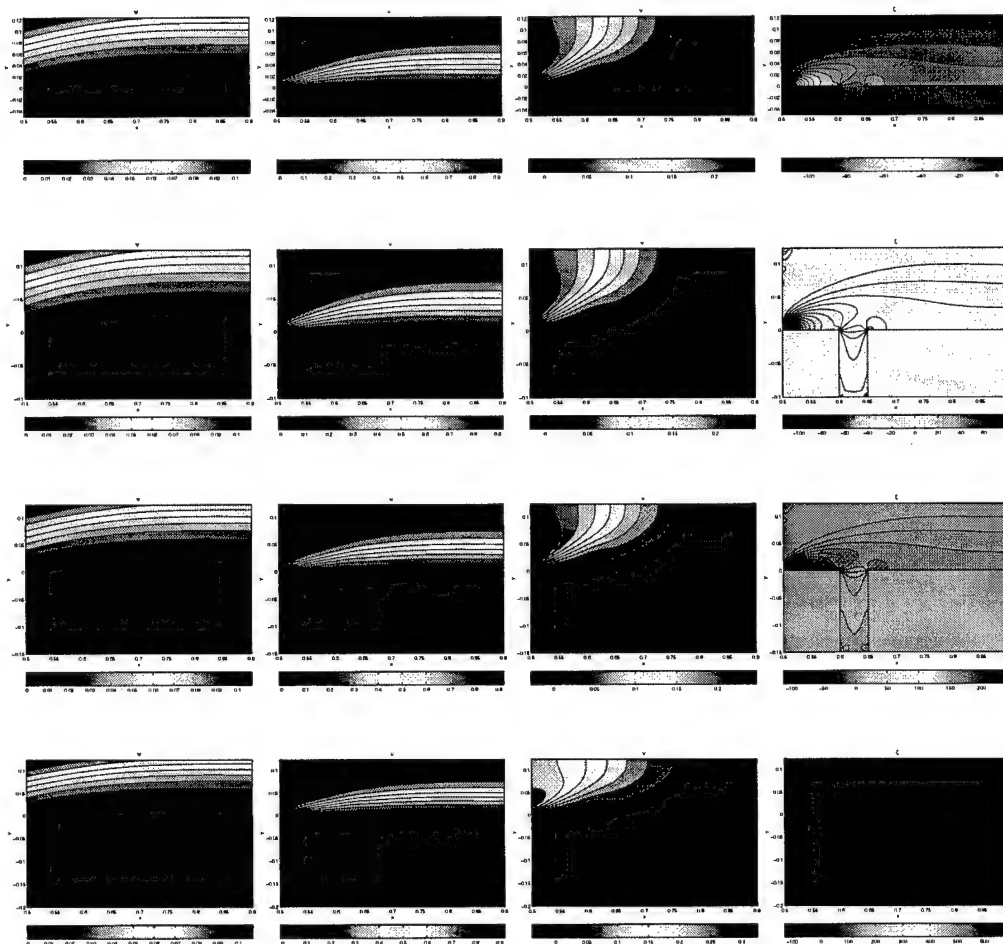
Figure 40. Steady-state rectangular open cavity solutions. Left to right column: $\psi, \psi_y, \psi_x, \zeta$. Upper to lower row: $D/L = 1, 2, 3, 4$ with $D = 10\delta^*$ and δ^* the flat-plate boundary layer displacement thickness at the inflow boundary. A spatial discretisation comprising 20^2 collocation points in each subdomain was used.
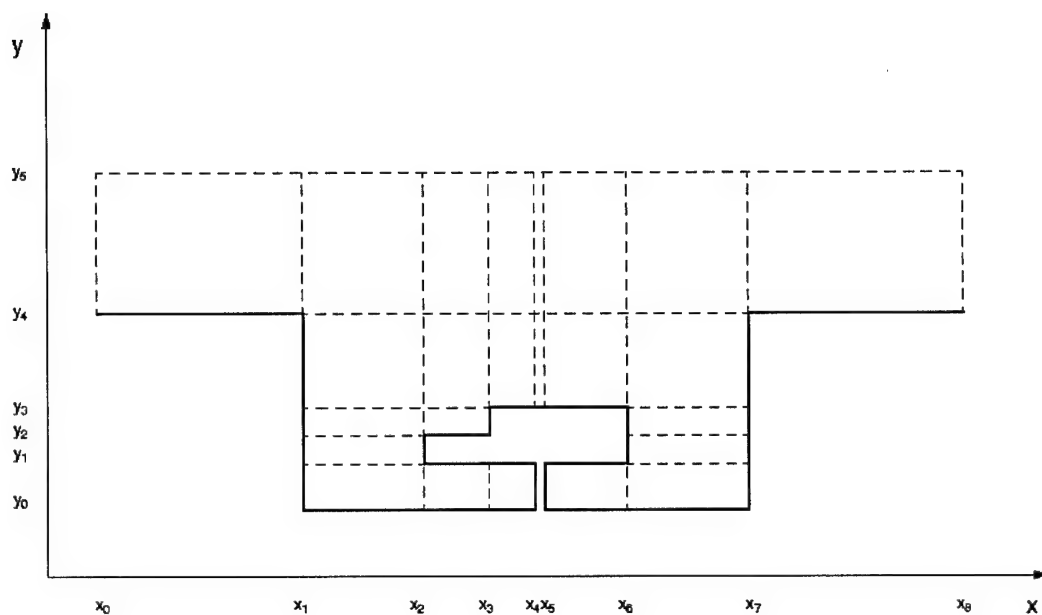
Figure 41. A model of an object contained in the open cavity and the resulting multidomain spatial discretisation
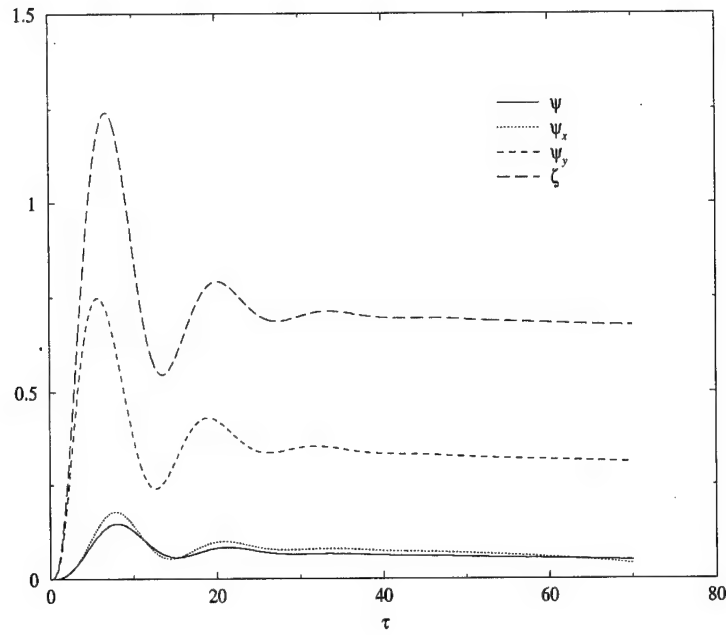
Figure 42. Local iteration history of the maxima of ψ, ζ and the velocity components for flow over the configuration depicted in Figure 41 using the parameters of Table 7. $Re = 295$ is imposed at inflow and 20^2 collocation points are used in each of the 24 subdomain shown in Figure 41.
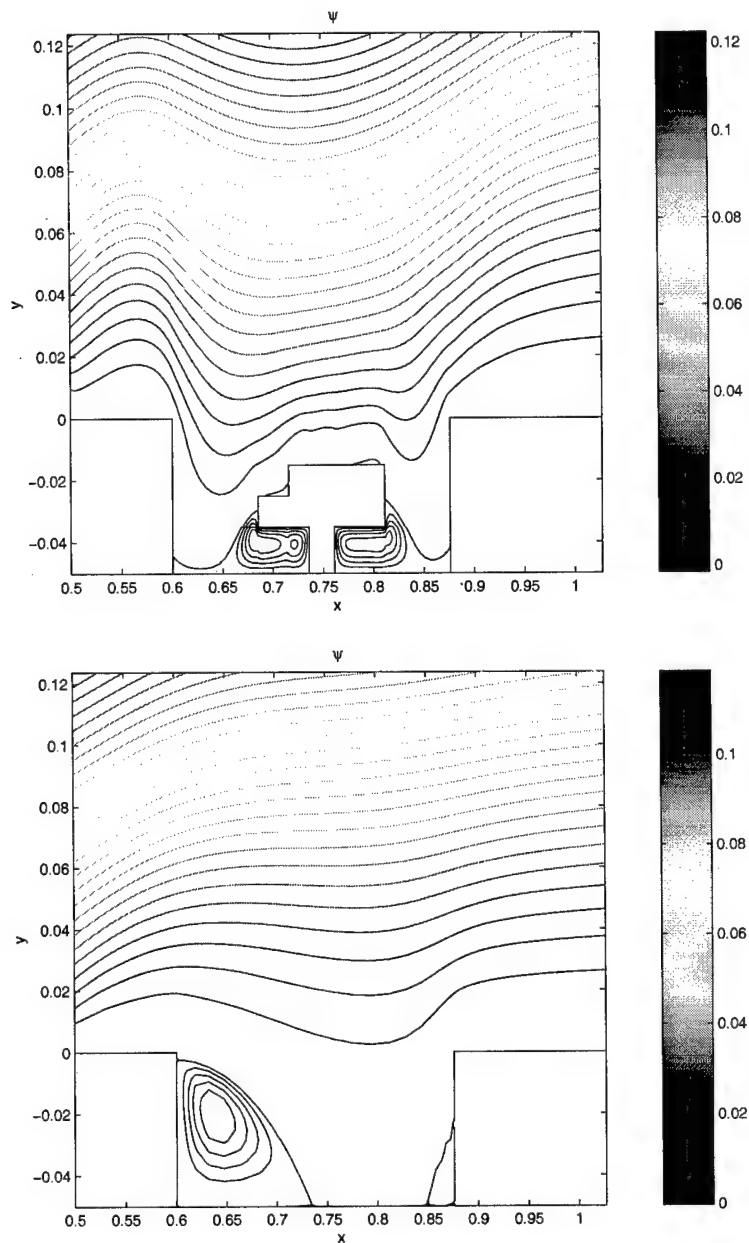
Figure 43. Streamfunction ψ contours in the full bay model flow (upper) compared against those of flow in the equivalent-sized empty cavity (lower).
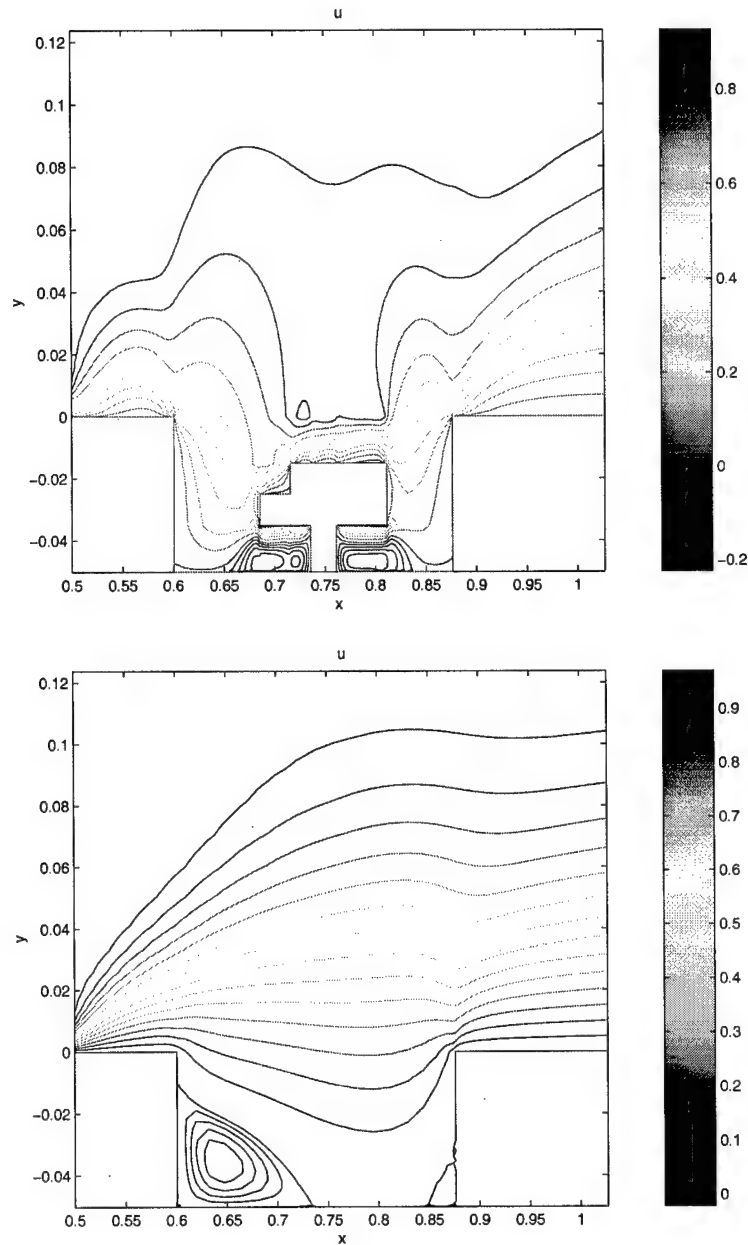
Figure 44. Velocity component $u = \psi_y$ contours in the full bay model flow (upper) compared against those of flow in the equivalent-sized empty cavity (lower).
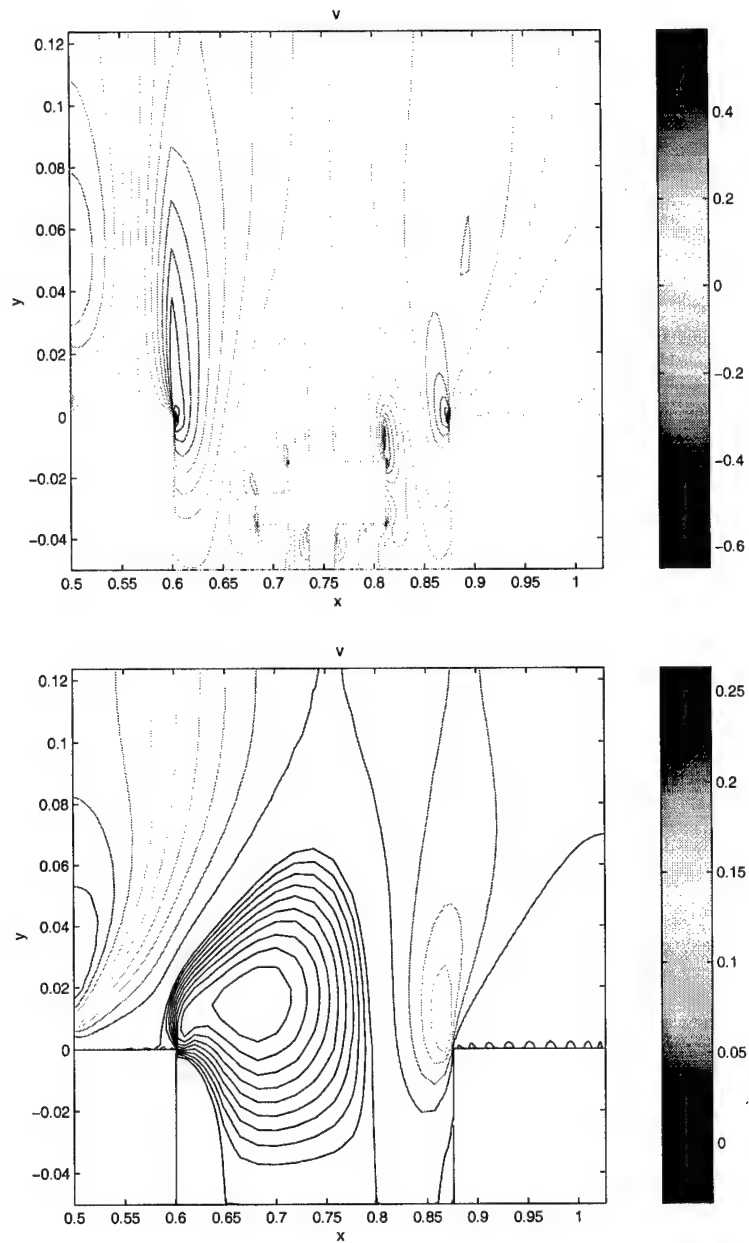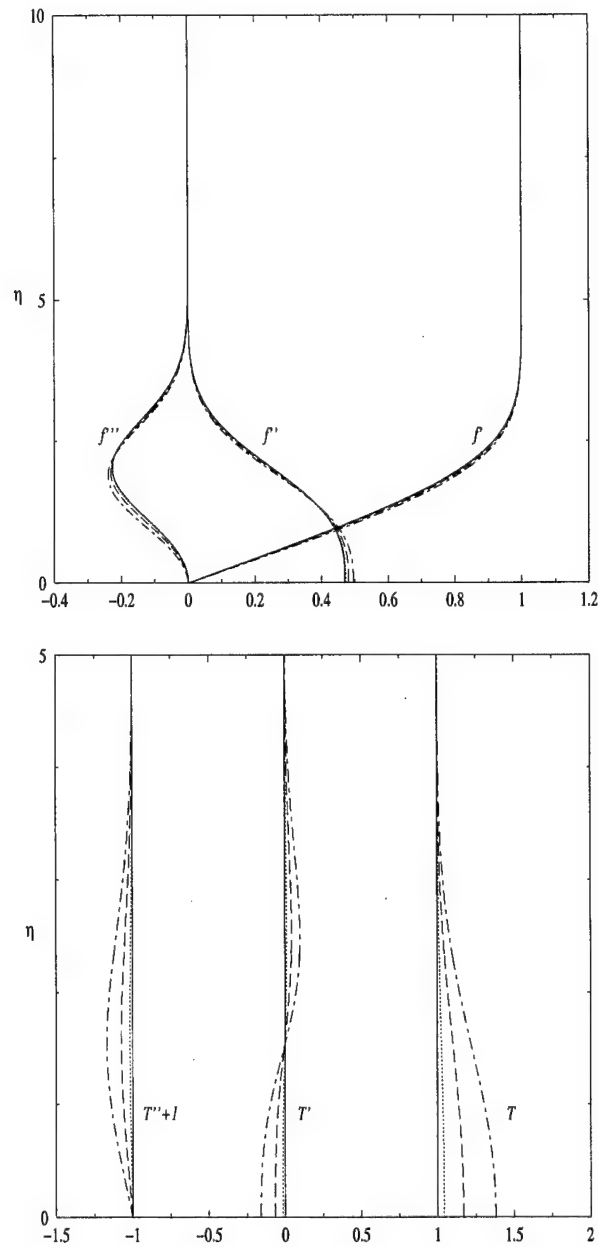
Figure 45. Velocity component $v = -\psi_x$ contours in the full bay model flow (upper) compared against those of flow in the equivalent-sized empty cavity (lower).

Figure 46. Compressible flat-plate boundary layer similarity solutions. Upper: Streamwise velocity component $u = f'$ and its first two derivatives; Lower: Temperature T distribution. Solid: $M_\infty = 0.01$, dotted: $M_\infty = 0.5$, dashed: $M_\infty = 1.0$, dash-dotted: $M_\infty = 1.5$.
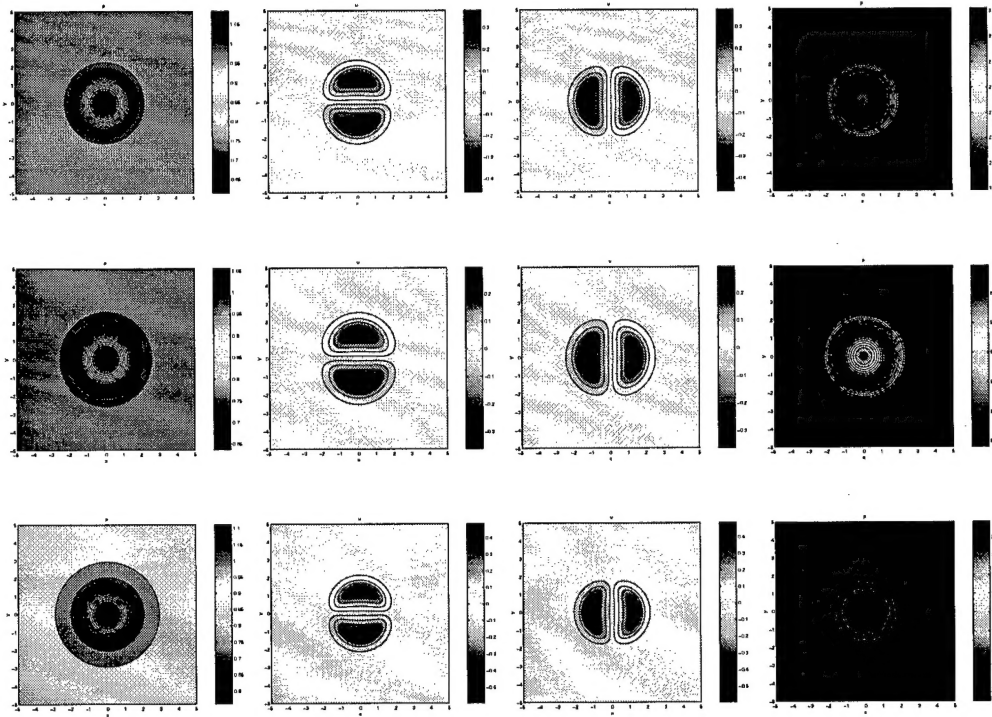
V. Theofilis

Figure 47. Transient vortical solutions in compressible flow at $t = 0.5$ (Visbal and Gaitonde 1998). Upper to lower row, $(Re, M) = (10^2, 1), (10^5, 0.6), (10^5, 2.6)$; left to right column, ρ, u, v, p.
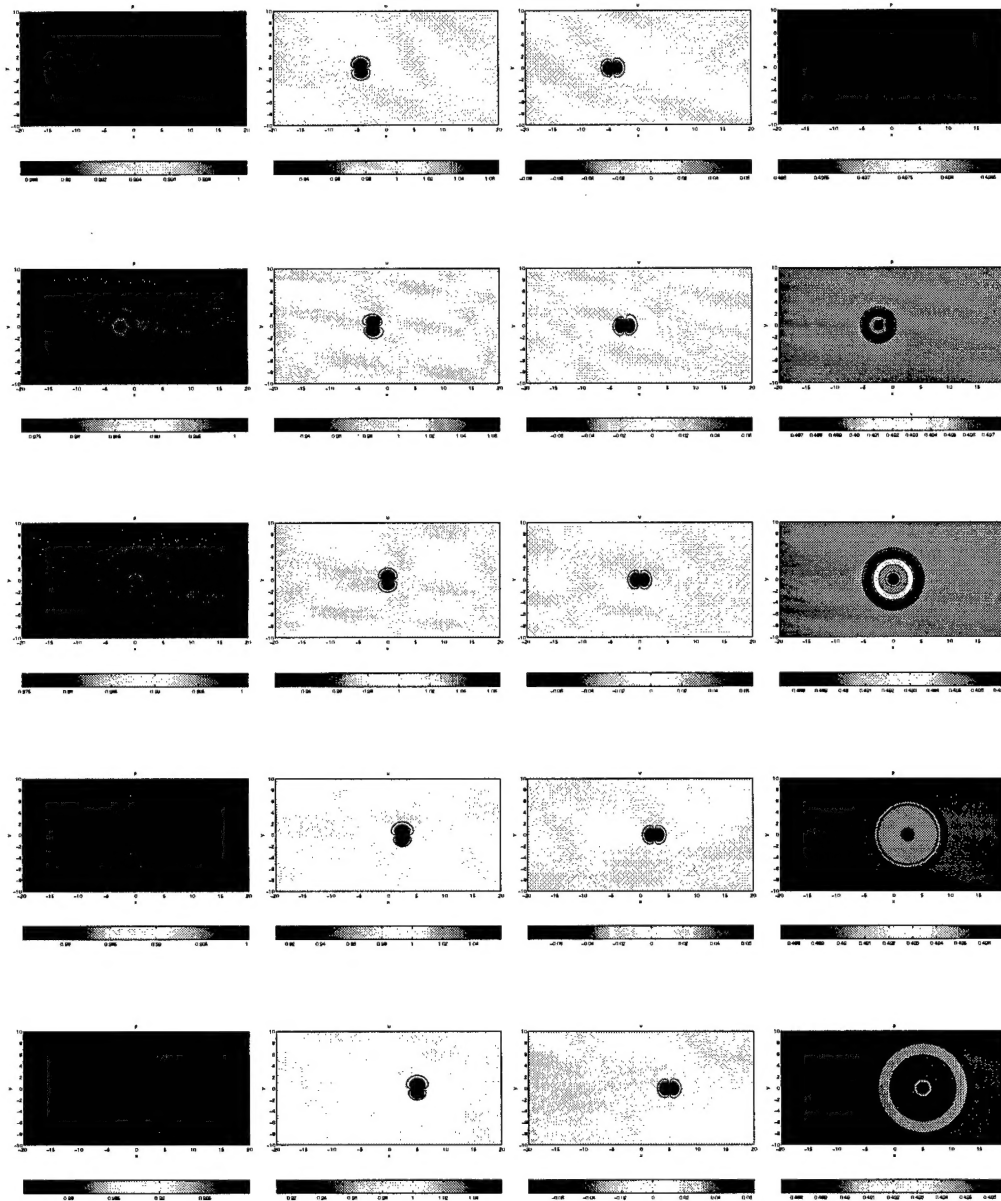
Figure 48. Advected vortex in $Re = 10^5, M = 1.2$ viscous compressible flow (Visbal and Gaitonde 1998). Left to right column ρ, u, v, p; upper to lower row, $t = 0, 2.5, 5.0, 7.5, 10.0$
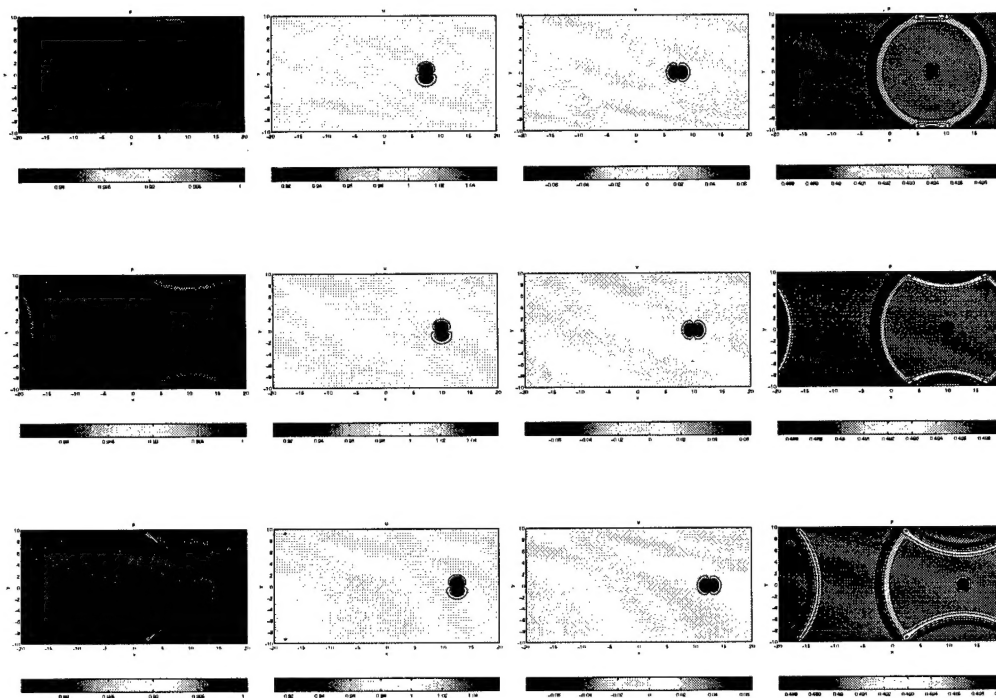
V. Theofilis

Figure 49. Advected vortex in $Re = 10^5$, $M = 1.2$ viscous compressible flow (Visbal and Gaitonde 1998). Left to right column ρ, u, v, p; upper to lower row, $t = 12.5, 15.0, 17.5$
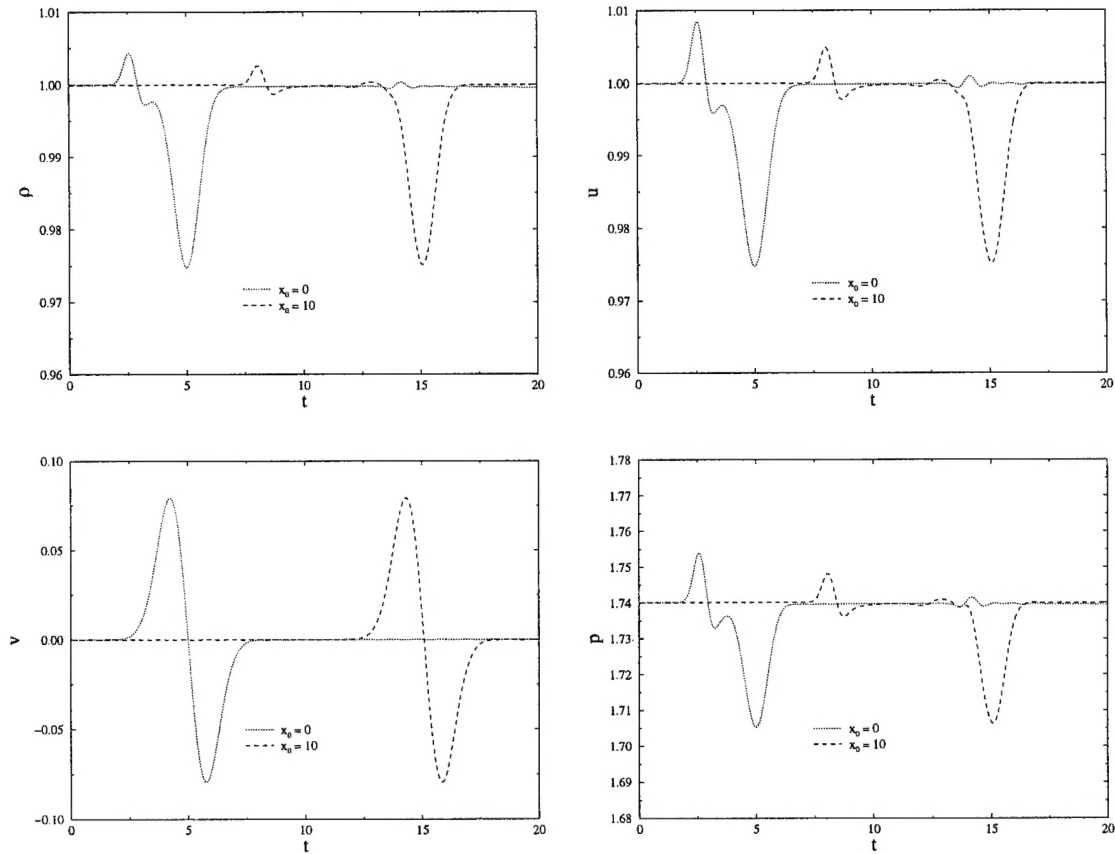
Figure 50. Vortical advection problem; $(\rho, u, v, p)^{\mathrm{T}}$ at $(x_0, 0)$ as function of time t. Dotted line $x_0 = 0$, dashed line $x_0 \approx 10$.